UNIVERSITY OF CALIFORNIA
RIVERSIDE

2D *Dirac* Materials: From Graphene to Topological Insulators

A Dissertation submitted in partial satisfaction
of the requirements for the degree of

Doctor of Philosophy

in

Electrical Engineering

by

Desalegne Bekuretsion Teweldebrhan

June 2011

Dissertation Committee:

Dr. Alexander A. Balandin, Chairperson
Dr. Roger Lake
Dr. Alexander Khitun

The Dissertation of Desalegne Bekuretsion Teweldebrhan is approved by:

_____

_____

_____

Committee Chairperson

University of California, Riverside

Acknowledgements

I would like to first acknowledge and express my sincere gratitude to my doctoral advisor Prof. Alexander Balandin, for his guidance and expertise during my graduate experience. I am appreciative for the support, kindness, patience, and professionalism he has always presented me with throughout my study. Prof. Balandin is one of the most respected and active researchers in our field. Throughout my studies I challenged myself to reach the high-quality research standards and work ethics he expected from his research group and staff. In the last few years, under his advisory, I was exposed to a world that very few people with my background could imagine existed. There is no doubt in my mind that the distinguished lessons and experiences he has equipped me with will always stay with me throughout my future endeavors. Thank you Prof. Balandin.

I would like to thank Prof. Roger Lake and Prof. Alexander Khitun for serving on my PhD dissertation committee. Their input and feedback of my research work lead to several fruitful discussions that I found beneficial for my studies.

I am grateful to the great lab members of Prof. Balandin's Nano-Device Laboratory (NDL). I would like to thank past students; Farough Parvizi, Dr. Suchismita Ghosh, Dr. Qinghui Shao, Dr. Muhammad Rahman and Dr. Irene Calizo, as well as current students Guanxiong Liu, Viveck Goyal, Craig Nolen, Md. Zahid Hossain, Farhan Shahil, and Javed Khan for their help and contributions towards my research work. I would also like to thank Dr. Dmitri Kotchetkov, Dr. Samia Sabrina, Dr. Denis Nika, Dr. Igor Bejenari, Jie Yu, and Zhong Yan for useful research discussions.

I am thankful to Prof. Roland Kawakami and his group in the Physics Department for their continuous support over the years. As an undergraduate, I worked with Prof. Kawakami and his students Kyle Pi, Richard Chiang, Yan Li, Ramesh Thamankar, and Wei-Hua Wang and was given the opportunity to take part in several fundamental science and experimental design projects. These projects exposed me to the world of nanoscale physics and materials growth methods, which became essential for my future graduate studies. Thank you to Wei Han, Jairo Velasco Jr., Kathy McCreary and Jared Wong for making my experiences there that much more fun and interesting.

Thank you to Maria Franco-Aguilar of UC Riverside's Graduate Division for being very supportive and helpful throughout my studies. These included her help in locating undergraduate research opportunities and my acquiring of a National Science Foundation Graduate Fellowship.

As always, I am thankful to my loving and supportive family. Thank you to my parents, Bekuretsion and Ainealem, whose unconditional love, prayers, and leadership have guided me and my siblings towards wanting to become productive members of society. They have always made sure I knew to keep my feet grounded, by reminding me of the all the responsibilities I have to carry on my shoulders. Thank you to my sister Letekidan and younger brothers Tesfay, Yonas and Mehari for all our joyful moments together. This dissertation is also dedicated to them.

Finally, all praises goes to God for blessing me with the ability to take on and complete my studies. His graces have allowed me to meet many great people during this journey of mine and I share this honor with them.

To My Parents,

Bekuretsion and Ainealem

ABSTRACT OF THE DISSERTATION

2D *Dirac* Materials: From Graphene to Topological Insulators

by

Desalegne Bekuretsion Teweldebrhan

Doctor of Philosophy, Graduate Program in Electrical Engineering
University of California, Riverside, June 2011
Professor Alexander A. Balandin, Chairperson

Silicon has been reaching physical limits as the semiconductor industry moves to smaller device feature sizes, increased integration densities and faster operation speeds. There is a strong need to engineer alternative materials, which can become foundation of new computational paradigms or lead to other applications such as efficient solid-state energy conversion. Recently discovered Dirac materials, which are characterized by the liner electron dispersion, are examples of such alternative materials. In this dissertation, I investigate two representatives of Dirac materials – graphene and topological insulators. Specifically, I focus on the (i) effects of electron beam irradiation on graphene properties and (ii) electronic and thermal characteristics of exfoliated films of Bi_2Te_3-family of

topological insulators. I carried out Raman investigation of changes in graphene crystal lattice induced by the low and medium energy electron-beam irradiation (5–20 keV). It was found that radiation exposures result in appearance of the disorder D band around 1345 cm^{-1}. The dependence of the ratio of the intensities of D and G peaks, I(D)/I(G), on the irradiation dose is non-monotonic suggesting graphene's transformation to polycrystalline and then to disordered state. By controlling the irradiation dose one can change the carrier mobility and increase the resistance at the minimum conduction point. The obtained results may lead to new methods of *defect engineering* of graphene properties. They also have important implications for fabrication of graphene nano-devices, which involve electron beams. Bismuth telluride and related compounds are the best thermoelectric materials known today. Recently, it was determined that they reveal the topological insulator properties. We succeeded in the first "graphene-like" exfoliation of large-area crystalline films and ribbons of Bi_2Te_3 with the thickness going down to a single quintuple. The presence of van der Waals gaps allowed us to disassemble Bi_2Te_3 crystal into the five mono-atomic sheets consisting of $Te^{(1)}$-Bi-$Te^{(2)}$-Bi-$Te^{(1)}$. The exfoliated films had extremely low thermal conductivity and electrical resistance in the range required for thermoelectric applications. The obtained results may pave the way for producing Bi_2Te_3 films and stacked superlattices with strong quantum confinement of charge carriers and predominantly surface transport, and allow one to obtain theoretically predicted order-of-magnitude higher thermoelectric figure-of-merit.

Contents

List of Figures

List of Tables

Chapter 1

Introduction

1.1 Motivations

Considered to be one of the greatest invention of the 20th century, the transistor is the most active component of all of modern technology. Experimentally first observed and demonstrated by John Barseen, Walter Bratain, and William Shockley in 1947 at Bell Labs, the transistor is a solid piece of semiconductor material with several contact terminals that connect it to an external circuit. Although transistors can be packaged individually, it wasn't till they were embedded into integrated circuits, vastly increasing their functionality, that they helped revolutionize the electronics field to unprecedented levels both technically and economically. In initial setups, several semiconductor materials were used to produce transistors which included germanium, gallium arsenide, silicon and even silicon carbide. Although it required higher melting temperatures and was naturally reactive, silicon offered the best prospects for better performance,

especially in logic based applications. Silicon transistors had shown to have far less leakage issues as compared to germanium, and in 1954 were the first commercially available transistors developed by Texas Instruments. Today, our technology is dependent on highly automated semiconductor processing methods based around silicon to mass produce low cost per-volume transistors.

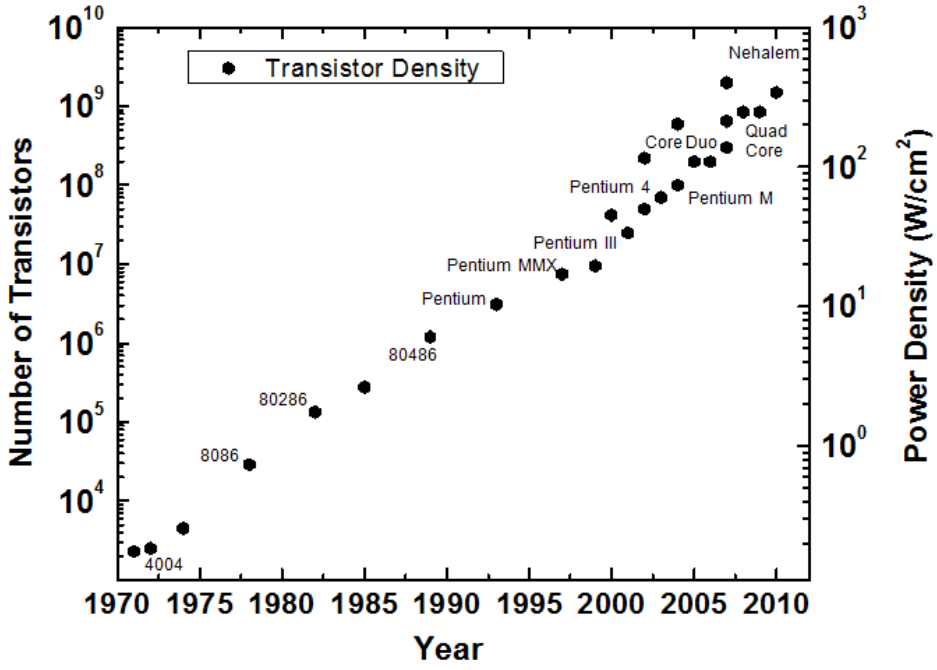

Figure 1.1: Plot of number of transistors and power density on a chip between the years 1970 and 2010. Plot from data provided by Intel Corporation.

As the basis roadmap of the semiconductor industry, Moore's Law has continuously projected performance gain that have resulted in shrinking transistor gate length, increase in number of transistors per wafer, wafer size growth, and reduction in defect density reduction. Along with the ability to help predict technological

expectations, Moore's Law has also been associated with the growing number of challenges from each new generation that the industry will continually need to address.

With high performance capacity, silicon-based contemporary metal oxide semiconductor (Si-CMOS) based transistor architectures are the most common used in today's electronics industry. Every two years, the industry makes changes to these fundamental structures of the transistor on the basis of using a miniaturization process. Also plotted, alongside the Moore's Law trend, in Figure 1.1 is the average power densities of processors with advancements which have shown to increase within the chips over the past 30 years. With miniaturization comes increased heat generation per unit area and increase thermal resistance so better cooling systems are necessary for further advancements in many technological application. Currently levels of heat generated in processors exceed 100 watts/cm^2, which can be categorized to be on the order, if not greater, than the heat produced from a nuclear reactor. As shown in Figure 1.2, the past shows that similar thermal issues were observed, prior to switching to CMOS architecture, in bipolar type transistors.

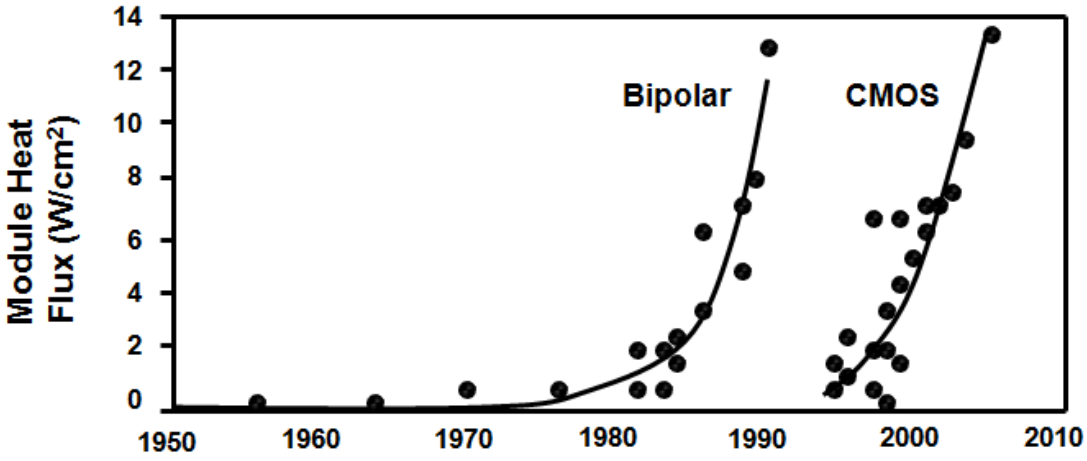

Figure 1.2: Plot indicates the increasing trends of heat produced from different generation of bipolar and CMOS architecture generations.

Currently, commercial products are available in the 45 nm and 32 nm technology node regimes, while advancements towards 22 nm and lower features sizes have already began production. As silicon based transistors reach physical and technological limitations, continuous research towards novel material with extraordinary properties have growingly been important to help meet the demands of the next generation of devices [1]. In the field of material science and disciplines alike, extensive research studies has been devoted into looking at alternative materials for devices integration with current technology.

The transistor is made up of several materials with a variety of physical properties that together allow for fast switching capabilities in the presence of an external field. Traditionally, thin layers of several semiconducting material and high thermal conductivity metal such copper have been used to construct such devices. The aggressive downscaling of the feature sizes and compact integration for new and complex structures

continuously requires expensive replacement of tools and instrumentations. With that the technology is being pushed to its limits, standard materials and new materials must both be capable of being processed using state of the art lithography methods for device fabrication. New and innovative ideas are also critical to meet the demands of device miniaturization and patterning techniques. A promising approach has recently been to look at incorporating materials with low dimensionalities that exhibit extraordinary properties into the chip design to help improve the device ability to perform effectively.

1.2 Dirac Materials

Dirac materials are defined as a class of material who possess a unique Dirac-like cone type of low-energy band structure within the first Brillioun zone. This allows for the production of extraordinary electrons that are distinctive from standard electron produced in metals. Typical electrons, like those found in standard metals, tend to behave like massive particles and have a quadratic energy dependence on momentum. Such massive electrons are said to obey Schrodinger's equation. Dirac electrons, on the other hand, have energies that contain a linear dependence on momentum and follow Dirac equations, see Figure 1.3. The linear dispersion will result in a $d^2\varepsilon/dk^2 = 0$ according to Eq. [1.1], which is used to determine the effective masse of electron in a material.

$$\frac{1}{m^*} = \frac{1}{\hbar^2}\frac{d^2\varepsilon}{dk^2} \qquad [1.1]$$

As a result, Dirac electrons behave like massless fermions which allow for ballistic transport along the surface of the Dirac material. Unlike other massless particles though, such as neutrinos, Dirac electrons have a charge. As a result, electrons in Dirac materials are charged massless particles that can easily be influenced by an external magnetic field.

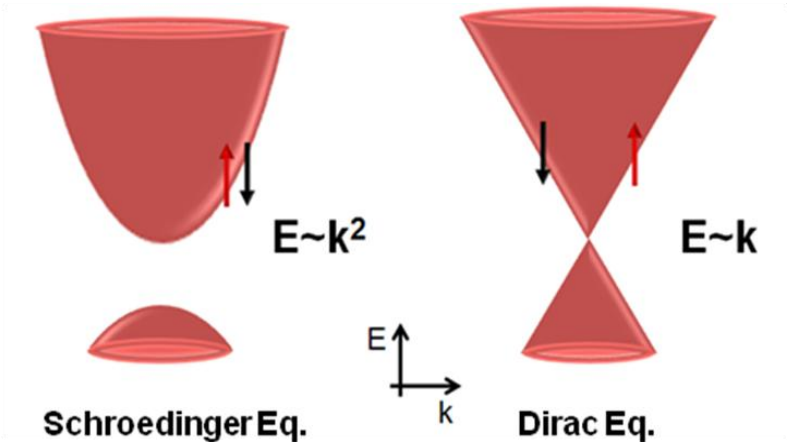

Figure 1.3: On the left is an illustration of the energy dispersion dependence for electrons in a typical metal that tends to follow Schrödinger's Equation and have a quadratic dependence to momentum. On the right is the dispersion relation for Dirac electrons which posses a linear Dirac-like dependence.

This opens the door to some exotic physics and physical properties in Dirac materials that are not found in typical materials, which may be utilized for a plethora of future applications. The pseudospins in the momentum direction are called chirality, which is used to refer to the additional built-in symmetry between electron and hole parts in the spectrum. We will discuss two types of Dirac materials here as possible candidates for future electronic application. These are single layer graphene and newly found Dirac

materials of bismuth telluride based topological insulator materials (i.e. Bi_2Te_3, Bi_2Se_3, etc).

1.2.1 Graphene

Graphene, a single atomic layer of graphite, is a flat sheet of carbon atoms tightly packed into a two-dimensional honeycomb lattice, and is a basic building block for graphitic materials of all other dimensionalities i.e. 0D buckyballs, 1D nanotubes, or 3D graphite. Theoretically, graphene has been studied for over sixty years, and is widely used for describing properties of various carbon-based materials. The material had not been considered to exist in the free standing state until it was reported by Andre Geim and K.S. Novoselov from University of Manchester, UK in 2004 [2]. Both Geim and Novoselov, would become recipients of the 2010 Noble Prize in Physics for their work with the new material. Graphene is a source of remarkable electronic properties, one of the reasons being its unique energy band structure. The electronic structure results from a simple nearest neighbor, tight-binding approximation. As seen in Figure 1.4, Graphene posses a two atoms per unit cell in its lattice structure which accounts for two conical points per Brillouin zone, called the Dirac points located at the two inequivalent Brillion zone corners (k and k'). At these corners of the Brillouin zone, the valence and the conduction band meet, with the Fermi energy level passing through these points. Energy dispersion curve in the vicinity of these points can be approximated to introduce a linear

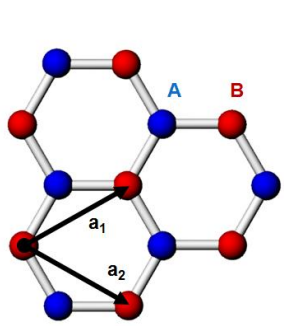

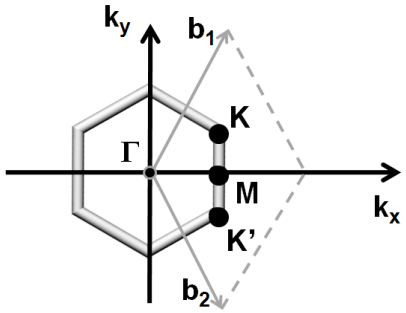

$$a_1 = \frac{a_o}{2}(3,\sqrt{3},0) \qquad b_1 = \frac{2\pi}{3a_o}(1,\sqrt{3},0) \qquad K = \frac{2\pi}{3a_o}(1,\frac{1}{\sqrt{3}},0)$$

$$a_2 = \frac{a_o}{2}(3,-\sqrt{3},0) \qquad b_2 = \frac{2\pi}{3a_o}(1,-\sqrt{3},0) \qquad K' = \frac{2\pi}{3a_o}(1,-\frac{1}{\sqrt{3}},0)$$

Figure 1.4: Crystal structures of Graphene which has two atoms per unit cell, which accounts for two Dirac points per Brillouin zone. Both are located at the two inequivalent Brillion zone corners (k and k') of its reciprocal lattice structure shown on the right.

relationship with momentum and is given by the Eq. [1.2],

$$H = \hbar v_f \begin{pmatrix} 0 & k_x - ik_y \\ k_x + ik_y & 0 \end{pmatrix} = \hbar v_f \sigma \bullet k \qquad [1.2]$$

where v_f is the Fermi velocity. Now, only graphene and its bilayer have such simple electronic spectra, they are both zero-gap semiconductors. For three and more layers, the spectra become increasingly complicated, where several charge carriers appear and the conduction and valence bands start notably overlapping.

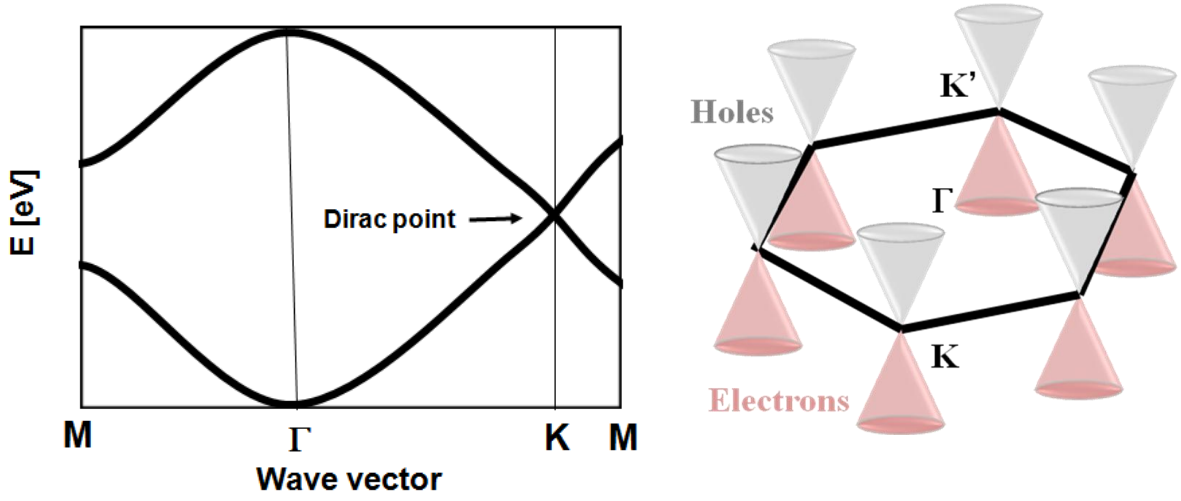

Figure 1.5: Energy band structure of graphene. The energy bands become cone shaped at the corner Dirac points at K and K'. Here the conductance band touches valence band.

The interaction between electrons and the honeycomb lattice causes the electrons to behave as if they have absolutely no mass. As a result, they are referred to as massless relativistic Dirac fermions. The electron dynamics in graphene obey the 2D Dirac equation, where the quantum mechanical description of electrons moving relativistically. The speed of light is associated with the material by its Fermi velocity of $v_f = c/300$. Thus graphene could even be utilized effectively to study quantum field theory without the use of a huge charge accelerator.

One of the most important merits of graphene is an ambipolar electric field effect. Here, charge carriers can continuously be tuned between the electrons and holes which may have mobilities that exceed 15000 $cm^2V^{-1}s^{-1}$ at room temperature. This feature makes graphene based devices achievable on silicon integrated circuits. In Figure 1.6, it's shown the effect an electric field has on a graphene device. The hall resistivity

changes polarity at Vg ~ 0V. This behavior shows that substantial concentrations of electrons (or holes) can be induced by positive (or negative) gate voltages. As a result, the resistance decreases with increasing carrier concentration with typical 1/ne dependence. Moreover, the resistivity follows a similar trend.

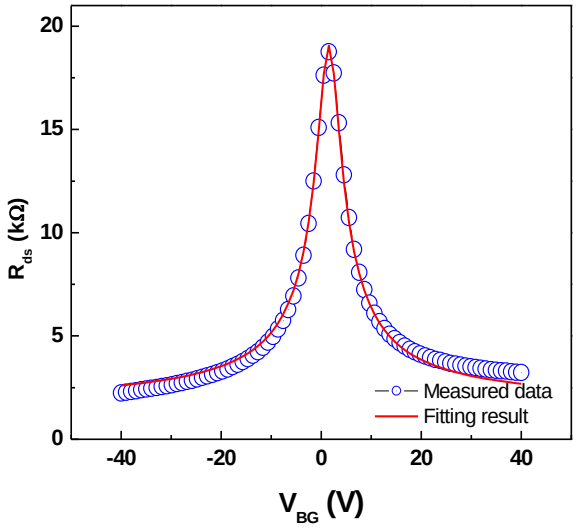

Figure 1.6: Graphene's ambipolar behavior change carriers with voltage bias.

1.2.2 Bi_2Te_3 Based Materials

The bismuth telluride (Bi_2Te_3) families of materials (i.e. Bi_2Se_3, Sb_2Te_3) have unique properties with a potential for diverse range of applications. Since the discovery of its extraordinary thermoelectric properties, Bi_2Te_3 has become a vital component for thermoelectric industry [3-5]. Bulk Bi_2Te_3-based materials are known to have the highest thermoelectric figure of merit, ZT ~ 1.14 at room temperature (RT). The thermoelectric figure of merit is defined as $ZT=S^2\sigma T/K$, where $S=-\Delta V/\Delta T$ is the Seebeck coefficient (ΔV is the voltage difference corresponding to a given temperature difference ΔT), σ is the

electrical conductivity and K is the thermal conductivity, which has contributions from electrons and phonons. It is clear from ZT definition that in order to improve thermoelectric figure of merit one should increase the thermopower $S^2\sigma$ and decrease the thermal conductivity. Different approaches have been attempted in order to enhance the thermoelectric properties of Bi_2Te_3 or its alloys. These approaches included change in stoichiometry, the use of polycrystalline materials with different grain sizes, intentional introduction of structural defects and incorporation of different dopants, e.g. Sb or Se, into Bi_2Te_3 lattice. The optimization of bulk Bi_2Te_3 led to incremental improvements but no breakthrough enhancement in ZT was achieved.

Bi_2Te_3 has the rhombohedral crystal structure of the space group D_{3d}^5 – R(-3)m with five atoms in one unit cell. The lattice parameters of the hexagonal cells of Bi_2Te_3 are a_H= 0.4384 nm and c_H = 3.045 nm [6]. Its atomic arrangement can be visualized in terms of the layered sandwich structure (see Figure 1.7 below). Each sandwich is built up by five mono-atomic sheets, referred to as *quintuple* layers, along the c_H axis with the sequence – [$Te^{(1)}$-Bi-$Te^{(2)}$-Bi-$Te^{(1)}$] – [$Te^{(1)}$-Bi-$Te^{(2)}$-Bi-$Te^{(1)}$] –. Here superscripts (1) and (2) denote two different chemical states for the anions.

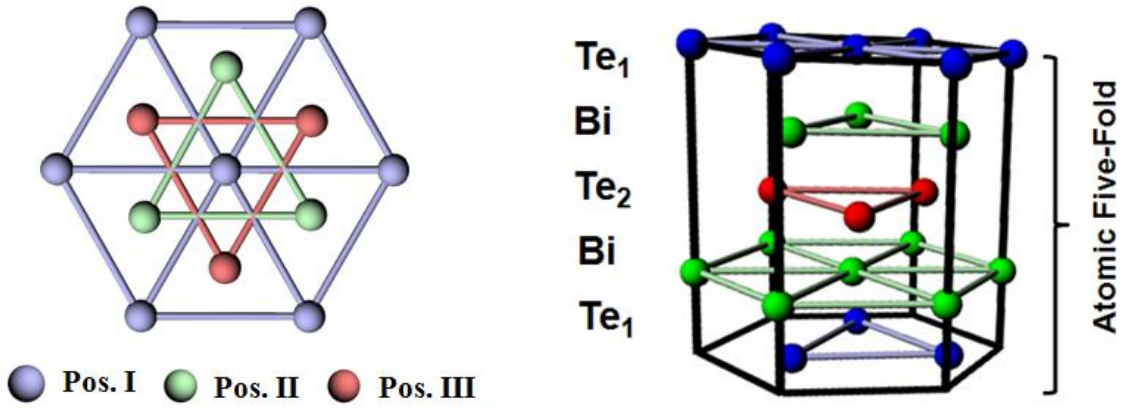

Figure 1.7: Schematic of Bi_2Te_3 crystal structure of D_{3d}^5 – R(-3)m space group showing a positions of Bi and Te atoms in a single five-fold quintuple layer.

Topological insulators is a relatively new and exciting area that looks at materials which have a bulk insulating gap and conducting surface states that are topologically protected against scattering by the time-reversal symmetry. This newly discovered class of materials was predicted to reveal many unique properties, e.g. quantum-Hall-like behavior in the absence of magnetic field. Some of these properties have already been demonstrated, stimulating interest into topological insulators as possible materials for quantum computing and magnetic memory with pure electrical read-write operations. As topological insulators, surface states of certain crystals are predicted to consist of a single Dirac cone. Moreover, it has been shown that the layered structures of Bi_2Te_3 and related materials such as Bi_2Se_3 and Sb_2Te_3 are also topological insulators [7-9].

The particles in topological insulators coated with thin ferromagnetic layers have manifested exotic physics and were proposed for possible applications in the magnetic memory where write and read operations are achieved by purely electric means.

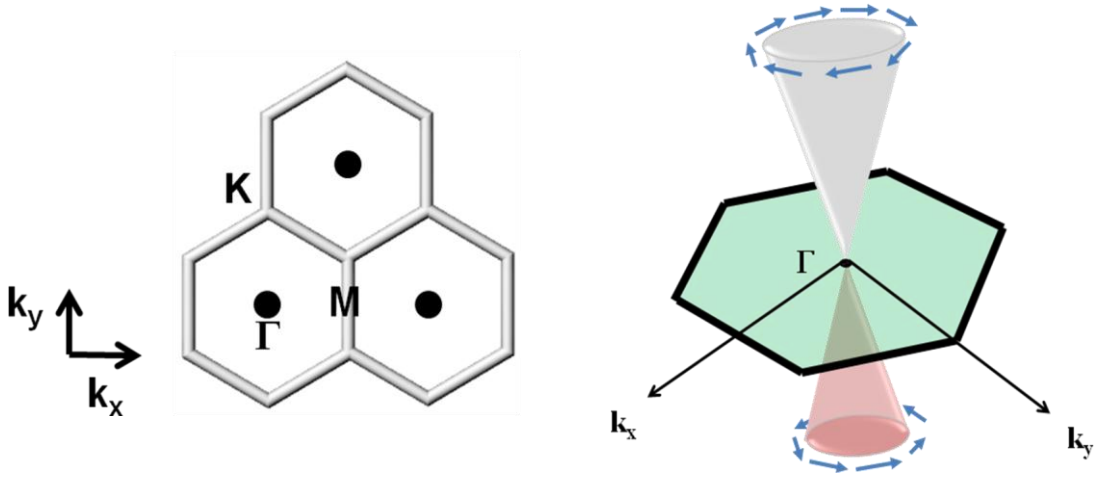

Figure 1.8: An idealized band structure for a topological insulator. The Dirac cone falls within the gamma point of the first Brillioun zone for the topologically-protected surface states.

Behind its theoretical physics, topological insulators are fundamentally described as material that behave as complete insulator within its interior while allowing ballistic transport of charges on its boundary. In the interior of a bulk three dimensional topological materials the electric band structure would be like that of any other insulator with the Fermi level being within its band gap. Now theoretically it has been determined that at the surface and edges, special states lie with the bulk band gap which allow for conduction of carriers. These carriers are allowed protected ballistic transport when their spin states are aligned and opposite with their momentums, which restricts scattering from occurring at particular energies as shown in Figure 1.9 [8, 10].

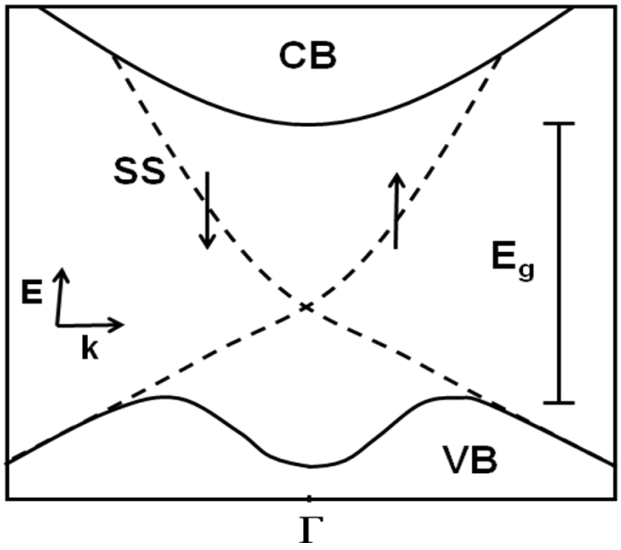

Figure 1.9: Illustration of the band structure for topological insulators. With the Fermi level falling within the bulk band gap which allow for dissipationless transport from protected surface states.

For observation of such effects, it is important that the material be free of defects, as the Fermi level must be within the band gap of the material [13, 14]. As such tuning effects can be done by doping or gating to challenge the effects bulk carriers and defects impurities [15, 16]. Konig *et al.* predicted and observed that in grown films of layered mercury telluride sandwiched between cadmium telluride topological effects occurred for a short period of time. Afterwards several experimental works were conducted, primarily with use of angle resolved photoemission spectroscopy, and wide variety of bulk materials were observed to be 3D topological insulators. The best observed results coming from Sb, Bi_2Se_3, Bi_2Te_3, and Sb_2Te_3 based materials [11, 12]. Beyond ARPES measurements, methods to observe such topological effects experimentally initially eluded researchers. This stimulated the search for methods to produce confined

nanostructure forms of quasi-2D crystalline forms of topological insulator based materials for even further enhance methods of characterizing such effects.

1.3 Confined Nanostructures

As a result of spatial confinement, it is been shown that classical physics breaks down and new effects can modify a material's properties. For example, in confined structures it has been theoretically shown that modification to a material's density of state occurs which directly affect how the material interacts with electrons, point defects, phonons, etc. As a benefit, in some cased low-dimensional confinement may also be utilized to enhance some material properties and allow for increased functionality e.g. electronic band gap tuning. Typically, one would need to produce nanostructures with thickness shorter than de Broglie wavelength of the material, typically less than 100nm in feature size.

$$\lambda = \frac{h}{p} \qquad\qquad p = \frac{E}{c} \qquad [1.3]$$

1.3.1 Quantum Wells

It has been theoretically predicted that atomically thin films metals and semimetals are thermodynamically unstable, and none could be shown to exhibit any notable field effect. Theoretical predictions have also projected that significant change in

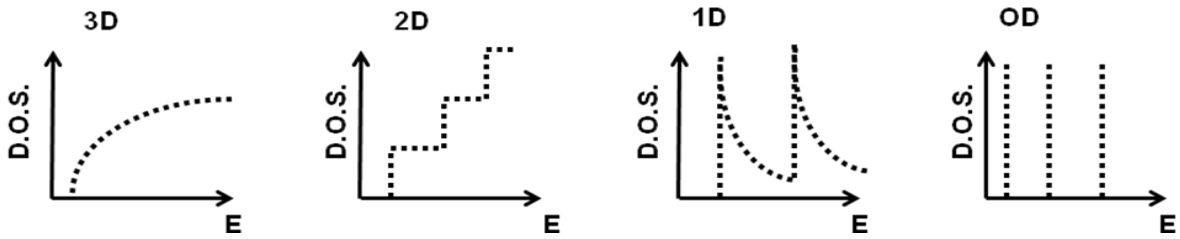

Figure 1.10: Electronic density of states modifications for a) bulk 3D crystalline semiconductors, b) 2D quantum wells, c) 1D nanowires or nanotubes, and d) 0D quantum dots. Low dimensionality of materials also exhibits other physical phenomena, other than a density of electronic states (DOS), which may be useful for enhancing thermoelectric performance.

the thermal properties of quantum well structures is possibly due to the confinement of charge carriers, which results in change to the carrier density of states [19]. These reports however ignored the effects of spatial confinement of phonons and bulk values of thermal conductivity were used. The spatial confinement of phonons in nanostructures and thin films can affect the phonon dispersion strongly and modify phonon properties such as phonon group velocity, polarization, and the interaction of phonons with other particles [20]. Such altered affects in quantum wells is only possible if materials are crystalline and essentially free of defects. The thickness of the thin film required to achieve the quantum confinement conditions has to be on the order of few atomic layers. Superlattices, which are commonly used for confined wells, are only partially confined with small potential barrier height and of relatively low material quality.

References

[1] G.E. Moore, "*Cramming More Components onto Integrated Circuits*", *Proc. IEEE*, **86**, 1, 82-85 (1998).

[2] K.S. Novoselov, A. K. Geim, S. V. Morozov, D. Jiang, Y. Zhang, S.V. Dubonos, I.V. Grigorieva, and A. A. Firsov, *Science*, **306**, 666 (2004).

[3] A.F. Ioffe, *Semiconductor Thermoelements* (Nauka, Moscow) (in Russian) (1956).

[4] A.F. Ioffe, *Semiconductor Thermoelectric and Thermoelectric Cooling* (Infosearch, London) (1957)**.**

[5] H.J. Goldsmid,R.W. Douglas, *Br. J. Appl. Phy*, **5**, 458 (1954).

[6] Feutelais, Y.; Legendre, B.; Rodier, N.; Agafonov, V. *Mater. Res. Bull*., **28**, 591 (1993).

[7] X. L. Qi and S.-C. Zhang, *Physics Today*, **63**, 33 (2010)**.**

[8] B.A. Bernevig, L.H.Taylor, and S-C Zhang, *Science*, **314**, 1757, 2006.

[9] M. Konig, S. Wiedmann, C. Brune, A. Roth, H. Buhmann, L. W. Molenkamp, X-L Qi, and S.C Zhang, *Science,* **318**, 766, (2007).

[10] C.L. Kane and E.J. Mele, *Phys Rev B*, **95,** 146802 (2005).

[11] L. Fu and C. L. Kane, *Physical Review B,* **76**, 045302 (2007).; S. Murakami, *New Journal of Physics*, **9**, 356 (2007).

[12] D. Hsieh, D. Qian, L. Wray, Y. Xia, Y. S. Hor, R. J. Cava and M. Z. Hasan, *Nature*, **452**, 970 (2007).

[14] M.Z. Hasan, and C. L Kane, Rev. Mod. Phys. **82**, 3045 (2010).

[15] H. Lin, L.A. Wray, Y. Xia, S. Xu, S. Jia, R. J. Cava, A. Bansil, and M. Z. Hasan, *Nature Materials*, **9**, 546 (2010).

[16] D. Hsieh, Y. Xia, D. Qian, L. Wray, F. Meier, J. H. Dil, J. Osterwalder, L. Patthey, A.V. Fedorov, H. Lin, A. Bansil, D. Grauer, Y. S. Hor, R. J. Cava, and M. Z. Hasan, *Phys. Rev. Lett.*, **103**, 146401 (2009).

[17] H.-J Noh, H. Koh, S.-J. Oh, J.-H. Park, H.-D. Kim, J. D. Rameau, T. Valla, T. E. Kidd, P. D. Johnson, Y. Hu and Q. Li, *EPL Europhysics Lett.*, **81**, 57006 (2008).

[18] D. Hsieh, Y. Xia, D. Qian, L.Wray, J. Dil, F. Meier, J. Osterwalder, L. Patthey, J. G. Checkelsky, N. P. Ong, A. V. Fedorov, H. Lin, A. Bansil, D. Grauer, Y. S. Hor, R. J. Cava, and M. Z. Hasan, *Nature*, **460**, pp. 1101–1105 (2009).

[19] L.D. Hicks and M.S. Dresselhaus, *Phys. Rev. B.*, **47**, 12727 (1993).

[20] A. Balandin, K.L. Wang, *Physical Review B*, **58**, 1544 (1998).; A. Balandin and K.L. Wang, *J. Applied Physics*, **84**, 6149 (1998).

Chapter 2

Experimental Setup

This chapter focuses on the initial processes that were developed for synthesis and fabrication methods for experimental analysis of 2D graphene as well as some new properties observed along the way. We start with a simple overview of some of these preparation methods, present experimental results that demonstrate unique methods of making such films, and characterize some of its intrinsic properties using Raman Spectroscopy. Introduction to the basics of the Raman Effect and electrical transport methods are also presented.

2.1 Thin Film Synthesis and Fabrication Methods

Before the first successful exfoliation method used to produce pristine graphene by Novoselov *et al.* [1, 12] in 2004, chemists used intercalated methods as a means to derive thin films of graphite for study. These methods required extensive processing, where the

graphite used for the intercalation was thoroughly dried by heating in vacuum at 150^{o} C for at least 24 hours and preserved in dry boxes filled with dry nitrogen, or mixed with different salts and heated at 110^{o} C for a few days. Later graphite films with few single layers were synthesized by simpler chemical exfoliation methods based on direct graphene intercalation methods [2]. The polymerization of unsaturated hydrocarbons as a result of these processes can be observed by using potassium as a catalyst that show the ability to exfoliated thin graphite films into graphene sheets. However, none of these methods allowed for detection and isolation of single graphene layer in chemical solutions of many different multi-layers graphite films.

From thermal decomposition method of 6H-SiC [3], a graphene monolayer can be synthesized due to the disjointing of carbon atoms from the SiC substrate. The formations of thin film carbon layers were observed to be formed in semi-orderly fashion due to the strong carbon-carbon interactions within a graphene layers and the good epitaxial fit to the substrate lattice structure. Such epitaxial growth method of graphene films offered one of the better viable routes towards electronic application. The limitation is that the process can only produce graphene films on particular substrates. Ultrathin epitaxial graphite films were produced on the Si-terminated (0001) face of single-crystal 6H-SiC by thermal desorption of Si. After surface preparation by oxidation or H_2 etching, samples are heated in ultrahigh vacuum (base pressure 1x10^{-10} Torr) to ~1000 ^{o}C in order to remove the oxide (some samples were oxidized/deoxidized several times to improve the surface quality) [4]. Scanning force microscopy images showed that the best initial surface quality was obtained with H_2 etching. After verifying by Auger electron

spectroscopy that the oxide has been removed, samples are heated to temperatures ranging from 1250 ^{o}C to 1450 ^{o}C for 1-20 min. Under these conditions, thin graphite layers are formed where the number of layers is determined predominantly by the temperature and the amount of time exposed to such annealing conditions.

Chemical vapour deposition (CVD) methods on certain crystal plane of metals (Cu [5], Pt [6], Pd [7], Co [7] and Ni [8-9]) of semiconductor (SiC [10], TiC [11]) can be also be used to synthesize graphene. Considered the most promising method for industrial production [10], CVD graphene is attractive as it provides the capability to produce large area coverage of transferable single layer graphene. Here the metal substrates are heated in a furnace which is attached to a gas delivery system. The gaseous carbon source (i.e. methane) is streamed across the metallic surface. The heated wafer attracts absorbents to the metal surface and as the temperature is cooled graphene is formed on the surface. Current challenges that CVD grown method include long range single crystal graphene formation (i.e. graphene grains produced), effective transfer from metallic surface to substrate of choice, and complete removal of functional groups from graphene surface.

In the absence of a high quality graphene production method, most experimental groups currently use graphene samples produced by micromechanical exfoliation of bulk graphite. This is the same technique that allowed the isolation of pristine graphene by Geims and Noveselov [1, 12]. Here an adhesive source, similar to scotch tape was used to repeatedly peel small flakes of graphite off a graphite source or mesas to form ultrathin

graphene regions. The combination of optical microscopy, Raman spectroscopy, and atomic force microscopy can be used to selectively locate thin film regions that are only a few graphene layers thick. For graphitic films thinner than 50 nm, there exist transparency levels to visible light when placed on thin SiO_2 on Silicon substrates. Here, the optical path shifts when interacting with thin graphitic films as compared to the substrate. The color for a 300 nm thick SiO_2, the standard oxide thickness used, on Si wafer gives off a violet-blue contrast and the extra thickness due to graphitic films shifts it to different blue shading based on its thickness [13].

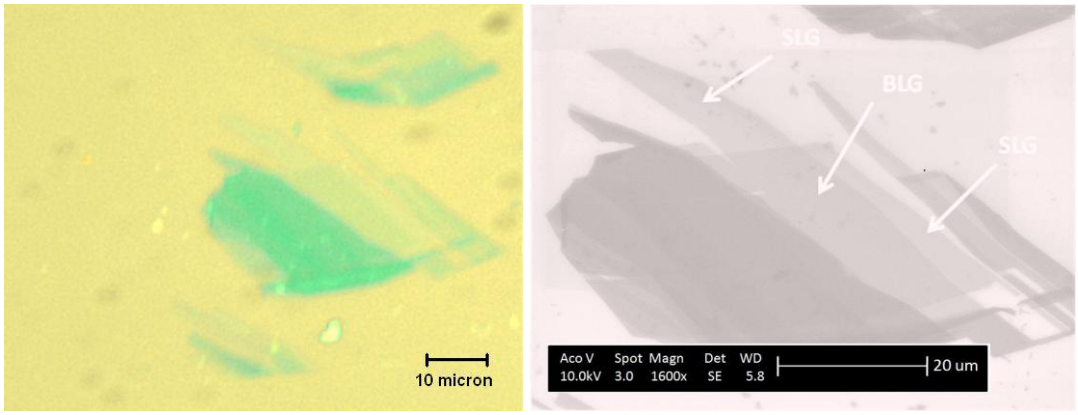

Figure 2.1: Images of a mechanically exfoliated thin graphitic flake in optical (left) and scanning electron (right) microscopes. Few-layer graphene is clearly visible in SEM but not easily optically.

Although invisible in optics, few-layer graphene (FLG) can still be seen clearly in a high-resolution SEM. Comparison between optical and scanning-electron micrographs of large areas on the wafer can be used to identify FLG films. Figure 3.5 shows a flake, which is easily identifiable on both SEM and optical images because of a thick region

nearby. The FLG film gives a clear contrast in SEM but would be impossible to see by optical methods if an isolated FLG film were shown. High-quality graphene crystallites up to 100um in size have been synthesized using micromechanical cleavage method.

For Bi_2Te_3 based materials, to observe useful low-dimensional confinement effects for the enhancement of the materials thermoelectric properties would require the production of quasi-two-dimensional structures with thickness of a few-atomic layer and high quality interfaces. Conventional chemical vapor deposition, electrochemical or other means are not capable of producing such quality structures. Molecular beam epitaxial (MBE) growth of low-dimensional thermoelectric materials was also much less successful than that of optoelectronic or electronic materials due to the lattice mismatch and other factors. These considerations create very strong motivations for the search of alternative approaches to fabrication.

The lattice spacing between layers has a direct relationship with the atomic bond strength between the neighboring layers. For this reason the weakest $Te^{(1)}$-$Te^{(1)}$ bond correspond to the largest spacing d~0.37 nm. What is also important for our purposes is that the strength and length of Bi-$Te^{(2)}$ bond is not much different from the van der Waals gaps of $Te^{(1)}$-$Te^{(1)}$. Experimental measurements of atomic layer spacing between layers are tabulated from several sources in Table 1. The latter suggests that the mechanical exfoliation may lead not only to [$Te^{(1)}$-Bi-$Te^{(2)}$-Bi-$Te^{(1)}$] quintuples but also to separate atomic planes of Bi-Te and Te-Bi-Te. One should note here that for thermoelectric applications, the quintuple layers or bound atomic planes of Bi-Te and Te-Bi-Te are of

greater interest than single atomic planes of Bi or Te atoms. For this reason, in this study we are mostly interested in producing individual quintuples or few-quintuple layers. The quasi-2D quintuple layers are also of principle importance for the investigation of topological insulators.

$Bi–Te_1$	$Bi–Te_2$	$Te_1–Te_1$	References
3.04 Å	3.24 Å	3.72 Å	Ref. 23
3.12 Å	3.22 Å	3.57 Å	Ref. 24
3.065 Å	3.246 Å	3.627 Å	Ref. 25
3.10 Å	3.235 Å	3.64 Å	Ref. 26

Table 1: The bond lengths between the atomic layers in Bi_2Te_3 quintuple layers. There is a correlation between the bond lengths and bond strength.

2.2 Raman Spectroscopy

The Raman Effect, which was discovered in 1928 by C.V. Raman, received a Nobel Prize in 1930. Today, the Raman scattering process is a well known characterization technique [14]. The basis of the effects is based on the inelastic scattering of photons with atomic lattice of a material resulting in the absorption or creation of a phonon. In crystalline material, phonons are simply the quantization of the vibrational waves as an atom in the

lattice is displaced from its equilibrium position. Raman spectroscopy is a robust non-destructive technique that uses resulting molecular vibrations to effectively characterize and analyze nanoscale physical changes.

When a photon hits a sample its lattice loses or gains energy $h\omega_{vib}$ where h is Planck's constant and ω_{vib} is the characteristic phonon frequency. As such, there will be an increase or decrease in the frequency of scattered photon, hence $\omega_\sigma = \omega_0 + \omega_{vib}$ or $\omega_\sigma = \omega_0 - \omega_{vib}$ respectively. So with an increase in frequency, a scattered photon has annihilated a phonon from the sample in a Raman process called anti-stokes process. If the frequency of the scattered photon is decreased then a phonon is absorbed by the sample in a Raman process called Stokes process. During Raleigh scattering, a photon interacts with the sample where the frequency of the initial photon and the scattered one are the same and there is no transfer of energy. In Figure 2.2, all scattering processes are illustrated showing change in energy and relative Raman intensity associated with each process.

A Raman spectrum consists of a plot of intensity (count of photons) versus Raman shift (cm^{-1}). The Raman shift represents the frequency (or energy) difference between the incident photon and the scattered photon. Peaks in the Raman spectra arise due to inelastic scattering of photons, giving us information on the vibrational modes of the atoms in the unit cell i.e. BZ center optical phonon modes.

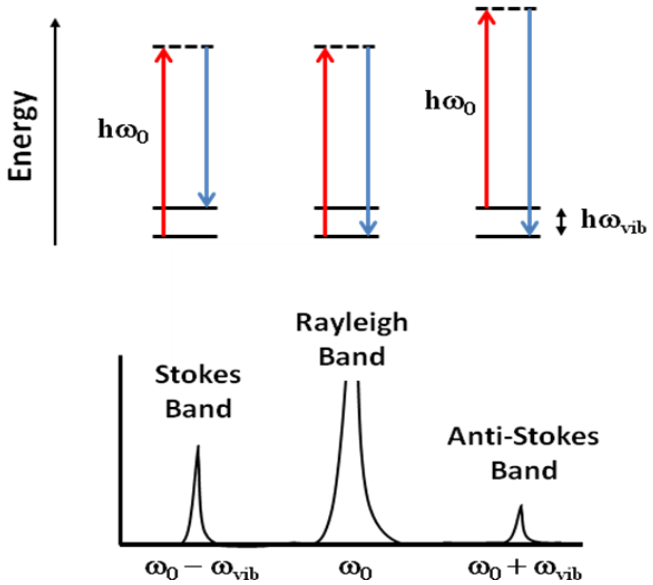

Figure 2.2: Rayleigh, Stokes, and Anti-Stokes scattering processes at the same laser frequency (below). Here the energy relationship of the photon during Rayleigh, Stokes, and anti-Stokes scattering is illustrated (top).

The Stokes process is the scattering of photons which shift to longer wavelengths and the anti-Stokes process which shift to shorter wavelengths. This is results in the photon shifting to lower and higher energy, respectively. The intensity of the anti-Stokes peak is heavily temperature sensitive. This arises due to the fact that the anti-stokes process allows for an energy transfer to the incident photon lowering the electron energy in the material to a ground state. Slight variances in thermal energy provided to the sample from that of the equilibrium state will create excitation of a few electrons to the higher excited states. This will allow for anti-stokes Raman spectroscopy to sense and monitor the temperature change in the material from that of an equilibrium state. In addition to temperature monitoring, Raman spectroscopy can be used to evaluate crystal

quality, alloy composition, carrier concentration, scattering time, ion-damage, annealing effects, and strain in semiconductors. In nanostructures, the phonons mean free path can be larger than the characteristic length giving rise to boundary scattering.

For our measurements, we use a micro-Raman spectroscopy which is carried out using the confocal Renishaw instrument [15]. The spatial resolution in our experiments has been limited only by the laser spot size (~1μm), which allowed us to selectively examine different regions of the few-micrometer sized thin film samples. The spectra were excited by the 488 nm visible laser. An optical microscope with 50x objective was used to collect the backscattered light. The spectra were recorded with the 1800 lines/mm grating. A special precaution was taken to avoid the local excitation laser heating of the samples by keeping the power on top of the samples below 4 mW.

2.2.1 Raman Spectrum of Carbon Materials

Raman spectroscopy has been widely used to characterize the structure of graphitic materials in the past forty years. The Raman spectra of graphite can be affected by basic structural properties such as in-plane crystallite size and out-of-plane stacking order. However, due to the poor sample quality, quantitative analysis was lacking. Amorphization takes place in mico- and nanometer sized graphitic materials, which increases the sp^3 carbon sample content and thus leads to significant changes in the Raman profiles. Recent systematic studies greatly improve the research using Raman scattering as a method to analyze nano-graphite. An empirical formula for the in-and out-

of-plane crystalline size dependence of the Raman scattering intensity has been established [16-18].

It was recently demonstrated that Raman spectroscopy can serve as a convenient technique for identifying number of graphene layers [15, 16, 19]. Ferrari *et al.* [16] studied the evolution of a 2D-band, which is a second order Raman active signature band found in carbon materials, and determined using a double-resonance model the shifting effects that the addition of single layer graphene create to the peak. The work goes on to demonstrate that micro-Raman spectroscopy can be used for unambiguous and high-throughput identification of the exact number of graphene layers with both the G peak and 2D bands. The details for this process will be discussed in section 3.2.1.

Beyond its uses as a nanometrology tool, Raman spectroscopy can be expanded to graphene-based devices to investigate the changes in the Raman signature peaks with temperature. This is essential for the graphene-based devices since applied electric bias and gate voltages may result in the device self-heating e.g. joule heating. Although the thermal conductivity of graphene is expected to be high, there are always some thermal resistances associated with the contacts and interfaces between different materials [20, 21], which may lead to local temperature increase which can be detected in the Raman spectrum [22]. These considerations provided an additional motivation for the temperature study of the graphene Raman signatures.

2.3 Electrical Transport

Materials may be characterized by the manner in which sub-atomic particles such as electrons or phonons travel through the material. When applying a voltage onto a material, information can be collected to identify how well the material may be able to transport electromagnetic information. The voltage difference between two points on the material is described by ohm law:

$$V = IR \qquad [1.1]$$

where V is the voltage difference across the conductor, I is the current, and R is the resistance. This is proportional and better understood terms of a resistivity ρ defined as:

$$R = \rho \frac{L}{A} \qquad [1.2]$$

where L is the length of the material and A is the cross sectional area. Usually it is more appropriate to use resistivity rather than resistance measurements to characterize the intrinsic property of materials.

Scattering of and random moving of charged particles, i.e. electrons and holes, in conductive material occurs in all directions. Such scattering may occur due to phonons, defects in the lattice structure of the material, or interfaces between different materials.

The net velocity at which the particle travels due to an applied field is known as the drift velocity, v_d. This is related to density of current J by:

$$J = nev_d \qquad [1.3]$$

where n is the charge carrier density and e is the electron charge. The mean free path between scattering points shortens with lose of drift velocity and has a direct relation to the mobility of charged particle in that material:

$$\mu = v_d / E \qquad [1.4]$$

where, μ is the mobility. One can quantify the intrinsic transport properties of conductor by also using:

$$\rho = \frac{1}{ne\mu} \qquad [1.5]$$

References

[1] K.S. Novoselov, A. K. Geim, S. V. Morozov, D. Jiang, Y. Zhang, S.V. Dubonos, I.V. Grigorieva, and A. A. Firsov, *Science*, **306**, 666 (2004).

[2] H. Shioyama, *J. Mater. Sci. Lett*., **20**, 499 (2001).

[3] A. Charrier, A. Coati, T. Argunova, F. Thibaudau, Y. Garreau, R. Pinchaux, I. Forbeaux, J.-M. Debever, M. Sauvage-Simkin, and J. –M. Themlin, *J. Appl. Phy*., **92**, 2479 (2002).

[4] C. Berger, Z. Song, T. Li, X. Li, A. Y. Ogbazghi, R. Feng, Z. Dai, A. N. Marchenkov, E. H. Conrad, P. N. First, and W. A. de Heer, *J. Phys. Chem. B*, **108**, 19912 (2004).

[5] X. Li, W. Cai, J. An, S. Kim, J. Nah, D. Yang, R. Piner, A. Velamakanni, I. Jung, and I. Tutuc, *Nature*, **324**, 1312 (2009).

[6] T.A. Land, T. Michely, R.J. Behm, J. C. Hemminger, and G. Comsa, *Surf. Sci.*, **264**, 261 (1992).

[7] J.C. Hamilton and J.M. Blakely, *Surf. Sci.*, **91**, 199 (1980).

[8] M. Elzenberg and J.M. Blakely, *Surf. Sci.*, **82**, 228 (1979).

[9] L.C. Isett, and J.M. Blakely, *Surf. Sci.*, **58**, 397 (1976).

[10] S. Bae, H. Kim, Y. Lee, X. Xu, J. Park, Y. Zheng, J. Balakrishnan, T. Lei, H.R. Kim, Y.I. Song, Y.-J. Kim, K.S. Kim, B. Ozyilmaz, J.-H. Ahn, B.H. Hong and S. Lijima, *Nature Nanotech.*, **5**, 574 (2010).

[11] H. Itoh, T. Ichinose, C. Oshima, T. Ichinokawa, and T. Aizawa, *Surf. Sci. Lett.*, **254**, 437, (1991).

[12] K.S. Novoselov, D. Jiang, F. Schedin, T. J. Booth, V. V. Khotkevich, S. V. Morozov, and A.K. Geim, *Proc. Natl. Acad. Sci.*, **102**, 10451 (2005).

[13] P. Blake, E.W. Hill, A.H. Castro Neto, K.S. Novoselov, D. Jiang, R. Yang, T.J. Booth, and A.K. Geim, *Appl. Phys. Lett.*, **91**, 063124 (2007).

[14] C.V. Raman, and K.S. Krishnan, *Nature*, **121**, 501 (1928).

[15] I. Calizo, D. Teweldebrhan, W. Bao, F. Miao, C. N. Lau, and A. A. Balandin, *J. Phys. C*., **109**, 012008 (2008).; I. Calizo, A.A. Balandin, W. Bao, F. Miao and C.N. Lau, *Nano Letters*, **91**, 071913 (2007); I. Calizo, F. Miao, W. Bao, C.N. Lau and A.A. Balandin, *Appl. Phys. Lett*., **91**, 071913 (2007).

[16] A.C. Ferrari, J.C. Meyer, V. Scardaci, C. Casiraghi, M. Lazzeri, F. Mauri, S. Piscanec, D. Jiang, K. S. Novoselov, S. Roth, and A. K. Geim *Phys. Rev. Lett.*, **97**, 187401 (2006).

[17] A. C. Ferrari, and J. Robertson, *Phys. Rev. B*, **61**, 14095 (2000).

[18] F. Tuinstra and J.L. Koening, *J. Chem. Phys.*, **53**, 1126 (1970).

[19] A. Gupta, G. Chen, P. Joshi, S. Tadigadapa, and P. C. Eklund, *Nano Letters* **6**, 2667 (2006).

[20] K. Filippov and A.A. Balandin, *J. Nitride Semicon. Research*, **8**, 4 (2003).

[21] P. L. Kapitza, *J. of Phys. (Moscow)*, **4**, 181 (1941).

[22] K. A. Alim, V. A. Fonoberov, and A. A. Balandin, *Appl. Phys. Lett.*, **86**, 053103 (2005).

[23] R. W. G. Wyckoff, Crystal Structures 2, *J. Wiley and Sons*, New York, (1964).

[24] C. A. Kagarakis, C. A., *J. of Material Science*, **13**, 7 (1978).

[25] H. Scherrer, B. Hammou, J.P. Fleurial, and S. Scherrer, *Phys. Lett. A*, **130**, 161 (1988).

[26] B. L. Huang, M. Kaviany, *Phys. Rev. B*, **77**, 125209 (2008).

Chapter 3

Graphene Preparation and Characterization

3.1 Preparation Methods of Atomically-Thin 2D Graphene

There are many methods reported to obtain atomically thin film samples i.e. mechanical exfoliation, chemical exfoliation, chemical vapor depositions or molecular beam epitaxial growth. For our work we use the common method of mechanical exfoliation which involves the cleavage breaking of van der Waals gaps from bulk layered materials. The identification and selection of thin layer regions is conducted by using a combination of optical microscopy, scanning electron microscopy, atomic force microscopy and Raman spectroscopy to characterize our single layer graphene (SLG), bilayer graphene (BLG), and few layer graphene.

3.2 Raman Spectroscopy of Graphene

The unique properties of graphene have recently attracted major attention of the physics and device research communities [1-2]. Raman spectroscopy has been successfully utilized as a convenient technique for identifying and counting graphene layers on the Si/SiO_2 substrates [3-4]. The most notable features of the spectrum are *G* peak at ~1580 cm^{-1}, which corresponds to the E_{2g} mode, and a relatively wide *2D* band around 2703 cm^{-1} [3-4]. The *2D* band is an overtone of the disorder-induced *D* band, which is frequently observed in carbon materials at ~ 1350 – 1360 cm^{-1}. The *D* band corresponds to the in-plane A_{1g} *(LA)* zone-edge mode, which is silent for the infinite layer dimensions but becomes Raman active for the small layers or layers with substantial number of defects through the relaxation of the phonon wave-vector selection rules [5]. The band at ~2445 cm^{-1} was attributed to the $T+D_2$ combination similar to the one observed in the carbon-implanted HOPG [6] and graphite crystal edge planes [7]. While the presence of *D* band in the spectra taken from a graphitic sample away from its edges indicates the structural disorder or other defects, it is not the case for *2D* band. The second-order phonon *2D* band is always present in graphene and other carbon materials owing to the double-resonance processes [8] involving two phonons. The expected spectral position of the *D* band is ~1350 cm^{-1}.

It was shown that the evolution of the 2D-band Raman signatures with the addition of each extra layer of graphene can be used to accurately count the number of layers [3] together with the position of G peak, which up-shifts with the increasing 1/*n*,

where *n* is the number of graphene layers [4]. Most of the Raman spectroscopy studies of graphene were limited to graphene layers on Si/SiO_2 substrates with a carefully selected thickness *W* of the SiO_2 layer ($W \approx 300$ nm). The latter is explained by the fact that graphene becomes visible in an optical microscope when placed on top of Si wafer with the 300-nm thick oxide layer due to the light interference. At the same time, it is not obvious that the features of the 2D band and G-peak position will be preserved when graphene is transferred to another substrate due to possible changes in the nature and density of the defects, surface charges and different strength of graphene – substrate bonding.

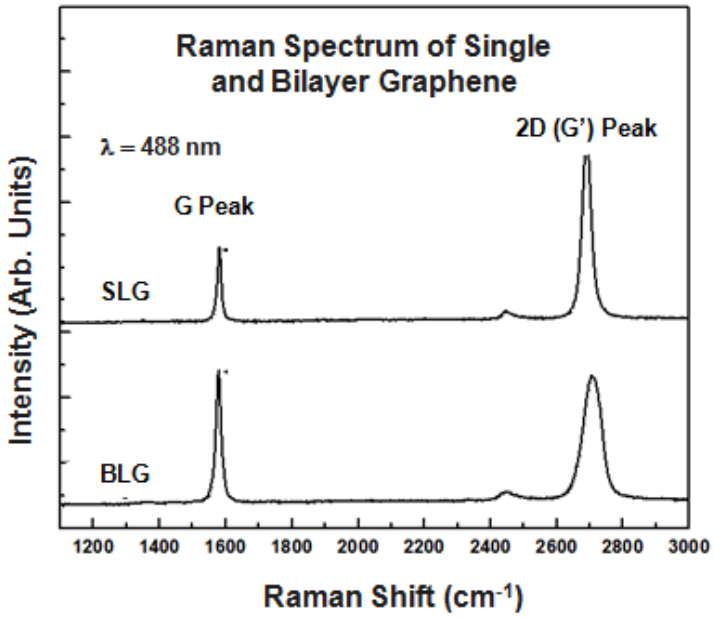

Figure 3.1: Raman spectrum of a nanographite sample. The G peak and 2D (G') bands that were taken with laser excitation energy of 2.41 eV (λ = 488 nm).

3.2.1 Raman as Nanometrology Tool for Graphene

Raman spectroscopy is known to be an effective tool for characterization of graphene and graphene multilayer's on the standard Si/SiO_2 (300 nm) substrates, which allows one to determine non-destructively the number of the graphene layers and assess their quality. The Raman phonon peaks undergo modification when graphene is placed on other substrates due to changes in the nature and density of the defects, surface charges and different strength of the graphene – substrate bonding. In Ref. [4], it was shown that despite the spectrum variations the deconvolution of the double-resonant 2D band allows one to identify the number of graphene layers. The results extend the application of Raman spectroscopy as nanometrology tool for graphene and graphene-based devices.

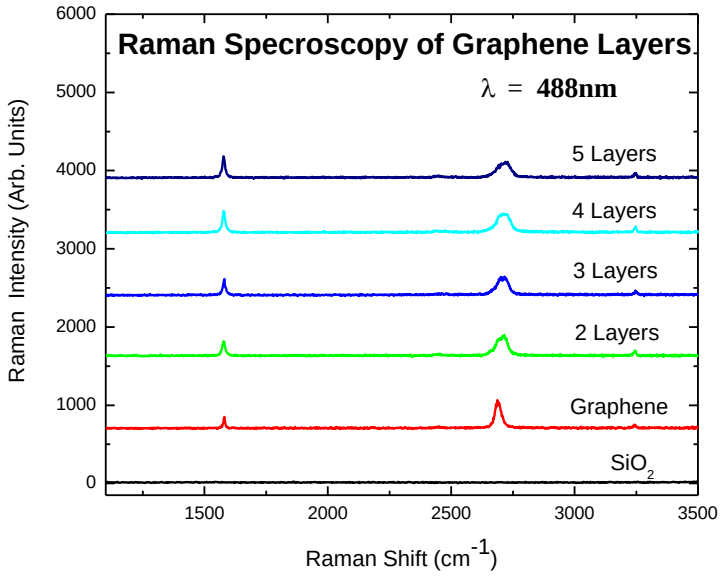

Figure 3.2: Raman spectrum of single, bilayer, 3-layer, 4-layer, and 5-layer graphene. Intensity ratio of 2D band to G peak for few-layer graphene is suppressed compared to single layer graphene.

Here, in Figure 3.2, its demonstrated the sensitivity of the 2D band to the number of graphene layers allowing one to count the atomic layers when graphene on 300nm SiO_2 atop Si substrates. The procedure of separating SLG and FLG on Si/SiO_2 substrates from graphitic flakes is well established and relies on differences in the G-peak and 2D-band. The wave numbers of the deconvoluted peaks for graphene with *n*=1-5 on the standard substrate under 488-nm excitation are summarized in Table 1. Since 2D band is a resonant band the Lorentzian peak positions depend on the excitation energy. As shown in the spectra in Figure 3.3, it's been indicates that the peaks and bulges appearing in the 2D band of BLG can be seen when on other substrates as well [4].

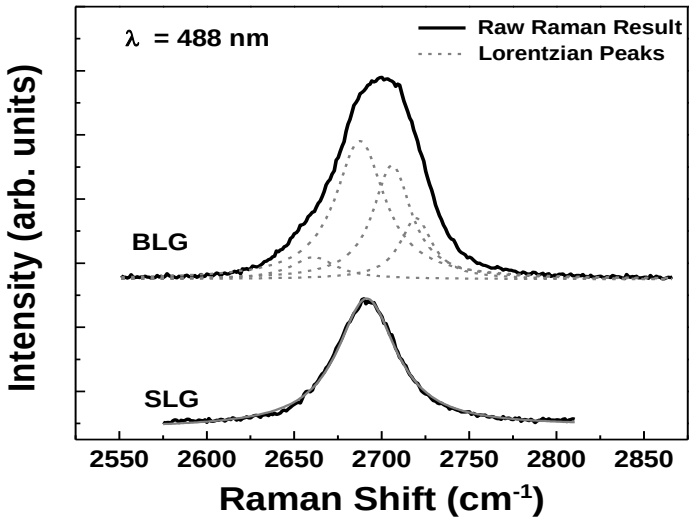

Figure 3.3: 2D band for SLG and BLG on a Si/SiO_2 substrate. Based on the number of Lorentzian elemental peaks in the deconvolution of SLG and BLG spectrums are explained by the double-resonance model. Adapted from Ref. [4].

Number of Layers	Lorentzian Peak Positions (cm^{-1})
n=5	D_{2A} = 2728, D_{2B} = 2762
n=4	D_{2A} = 2702, D_{2B} = 2732
n=3	D_{2A} = 2697, D_{2B} = 2719
n=2	$2D_{1B}$ = 2661, $2D_{1A}$ = 2688 $2D_{2A}$ = 2706, $2D_{2B}$ = 2719
n=1	2D = 2691

Table 2: From the deconvolution of the 2D band for few-layer graphene, layers can be distinguished easily on standard SiO_2/Si substrate. Table was retabulated from Ref. [4].

3.3 Experimental Results

In order to achieve further progress in graphene electronics one has to develop a technology for producing a large area continuous graphene sheets with a controlled number of layers and low defect density. As of today, the highest quality graphene layers were produced by the mechanical exfoliation of graphene from the highly oriented pyrolytic graphite (HOPG) with the help of some adhesive like a scotch tape [1]. Besides using mechanical exfoliation method with standard HOPG and Kish commercial graphite sources, we investigated a new approach for producing high quality graphene layers

using the high-pressure high-temperature (HPHT) growth process and describe the physical properties of the resulting material.

3.3.1 Synthesis Using HPHT Method

Graphene is able to be produced by the high pressure – high temperature (HPHT) growth process from the natural graphitic source material by utilizing the molten *Fe-Ni* catalysts for dissolution of carbon. For this synthesis of graphene, a mono-layer of carbon atoms arranged in a honey comb lattice, and assessment of the properties of obtained graphene layers are observed using the micro-Raman characterization. The resulting large-area graphene flakes were transferred to 300 nm SiO_2-Silicon substrates for the spectroscopic micro-Raman and scanning electron microscopy inspection. The analysis of the *G* peak, *D, T+D* and *2D* bands in the Raman spectra under the 488-nm laser excitation indicate that the high pressure – high temperature technique is capable of producing the high-quality large-area single-layer graphene with a low defect density. The disorder-induced *D* peak around ~1359 cm^{-1} while very strong in the initial graphitic material is completely absent in the graphene layers. The proposed method may lead to a more reliable graphene synthesis and facilitate its purification and chemical doping.

Also known as the temperature gradient process [13], to prepare the graphitic material by HPHT methods the samples were synthesized in the split sphere growth apparatus, which is conventionally used for diamond growth [14]. The detail description of the apparatus has been reported by Abbaschian *et al.* [15]. To produce easily exfoliated graphitic layers we loaded bulk natural graphite on top of the solvent, which was placed

on a substrate of stabilized zirconia infiltrated with *CsCl* (see Figure 3.4 (a-c)). Figure 3.4 (a) shows a schematic of the chamber while Figure 1 (b) illustrates the growth process. In order to grow a mono-crystal material we used metal catalyst consisting of *Fe* - *Ni* alloy and placed a small seed diamond crystal. During the growth process, the graphite source material completely dissolves in the solvent and re-grows on the substrate as either single- or polycrystalline diamond or graphitic layers, depending on the growth conditions (see Figure 3.4 (b)).

Regardless of the catalyst used, the most critical requirement for producing the desired carbon material is the control of the temperature *T* and pressure *P* through the entire process. By varying the growth conditions, we found a regime which leads to the formation of the loose graphitic layers and flakes of graphene rather than diamond. The selected *T* and *P* values were in the range 5 – 6 GPa and 1300 – 1700 ^{o}C, which correspond to the region right below the diamond – graphite equilibrium line in the HPHT phase diagram [12]. Excessive growth rates lead to inclusions and morphological instabilities resulting in strain and high density of defects. For this reason, we kept our mass growth rates low, at about 4 mg/h during the initial stage (less than 40 h), and gradually increased them to about 20 mg/h at the final stage. Such a regime corresponded to an approximately constant deposition rate per unit area (mm/h).

The resulting material, removed from the growth chamber, has a cylindrical shape with ~ 1 cm diameter and height (see Figure 3.4 (c)). Although most of the cylinder material is of graphitic nature, the bottom re-crystallized carbon layers (up to ~1 mm) are

very loosely connected to each other and can be easily peeled off. We have transferred a number of layers to Si/SiO_2 substrates without the help of the adhesives but by simply rubbing the cylinders against the substrates. In order to confirm the number of layers and assess the quality of HPHT graphene we used micro-Raman spectroscopy, which has proven to be the most reliable tool for graphene characterization [3-4]. It was not possible to carry out micro-Raman characterization of the top graphene flakes directly on the cylinders, removed from the growth chamber, because of the large background signal from the underlying carbon material. The obtained graphene flakes are large in size with many exceeding ~10 μm in one of the lateral dimensions (see Figure 3.5 (a)). Figure 3.5 (b) is a scanning electron microscopy (SEM) image of a graphene sample, which was taken to verify the material uniformity [16].

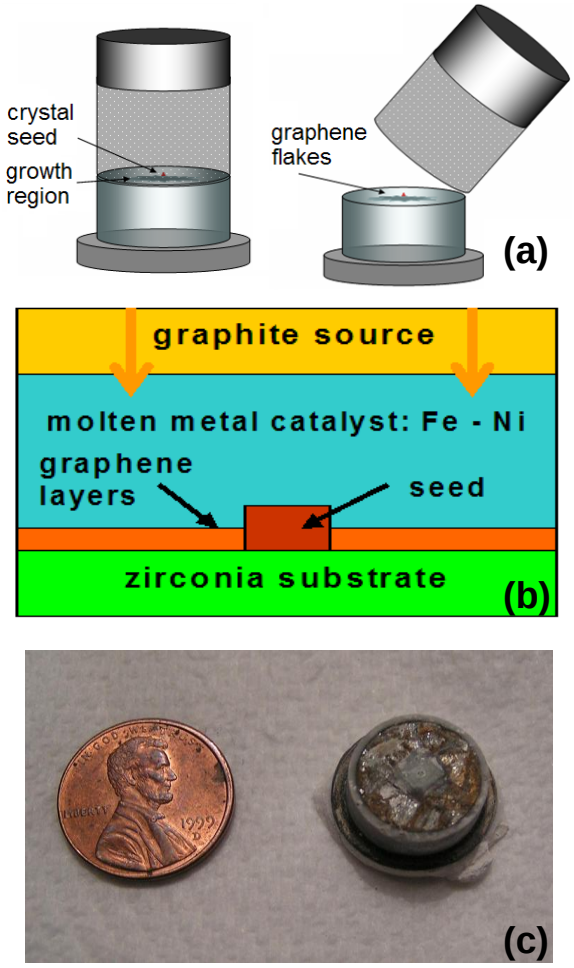

Figure 3.4: (a) Schematic of the graphene growth "cylinder"; (b) illustration of the high pressure – high temperature growth in the "split sphere" apparatus; (c) image of the cylinder with the material after it was removed from the growth chamber. Note that the region in the center, near the seed, is uniform indicating crystalline layers while the material at the edges is rough amorphous carbon. Reproduced in part with permission from: F. Parvizi, D. Teweldebrhan, S. Ghosh, I. Calizo, A.A. Balandin, H. Zhu and R. Abbaschian, *Micro and Nano Letters*, 3, 1, 29-34 (2008). Copyright 2008. Institution of Engineering and Technology.

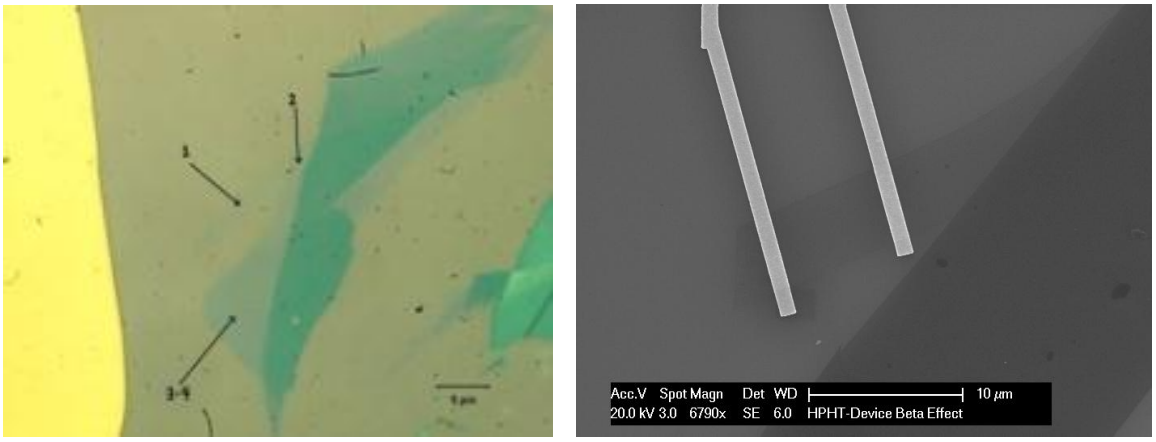

Figure 3.5: (a) Optical image of the HPHT grown graphene flakes. The gray – green color regions correspond to single layer graphene while yellowish regions are bulk graphitic pieces. (b) Scanning electron microscopy image of the edges of a large graphene flake with the dimensions of ~ 10 μm x 3 μm produced via the HPHT growth. The SEM inspection confirmed the uniformity of graphene layers.

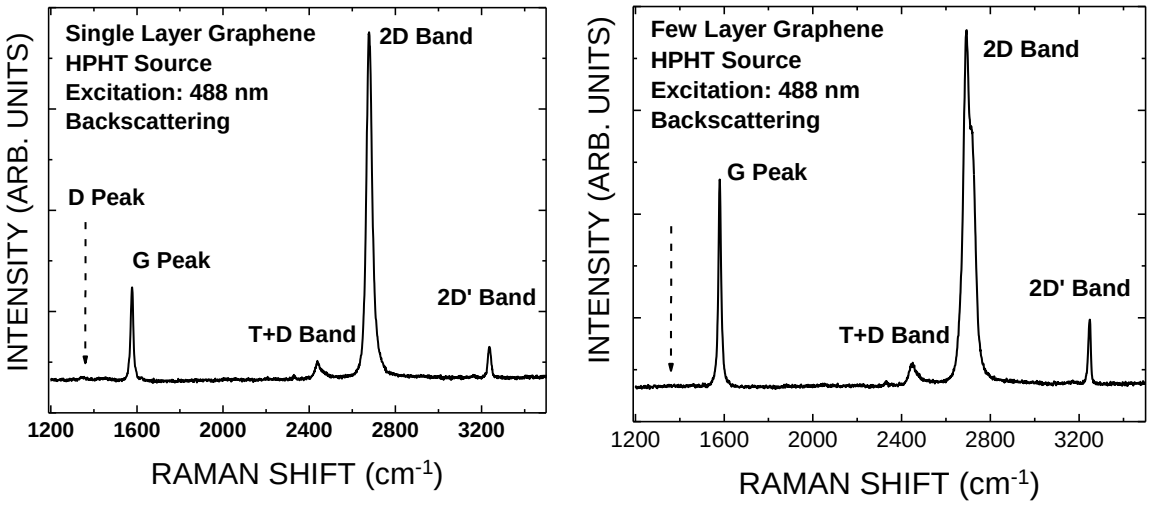

Figure 3.6: Raman spectrum of the single layer graphene (a) and few-layer graphene (b) produced via the HPHT melting growth process with *Fe-Ni* catalysts. The shape and location of the *G* peak and *2D* band were used to count the layers. The absence of the disorder *D* band near 1350 cm^{-1} attests to the high quality of the grown graphene.

Figure 3.6 (a-b) shows a typical spectrum from the HPHT single layer and few-layer graphene. Its absence of the disorder band, D-peak, in the spectra of HPHT graphene and graphene multilayer confirms the quality of the grown material. To understand the evolution of the material during the HPHT growth process and determine the number of graphene layers we analyzed the *G* peak region and the shape of *2D* band in the initial graphite and resulting HPHT material. Figure 3.7 shows a close up of the *G* peak region for the initial bulk graphite loaded to the growth apparatus (marked by squares), HPHT as-grown graphitic layers (marked by triangles) and single layer graphene separated from the top of the HPHT cylinders (marked by circles). The *G* peak position in graphene is slightly up-shifted as compared to graphite, which is in line with Refs. [8-9]. It is interesting to note that the disorder-induced *D* band at 1359 cm^{-1} is very strong in the initial low grade natural graphite source material but completely absent in as-grown HPHT graphitic layers and single layer graphene.

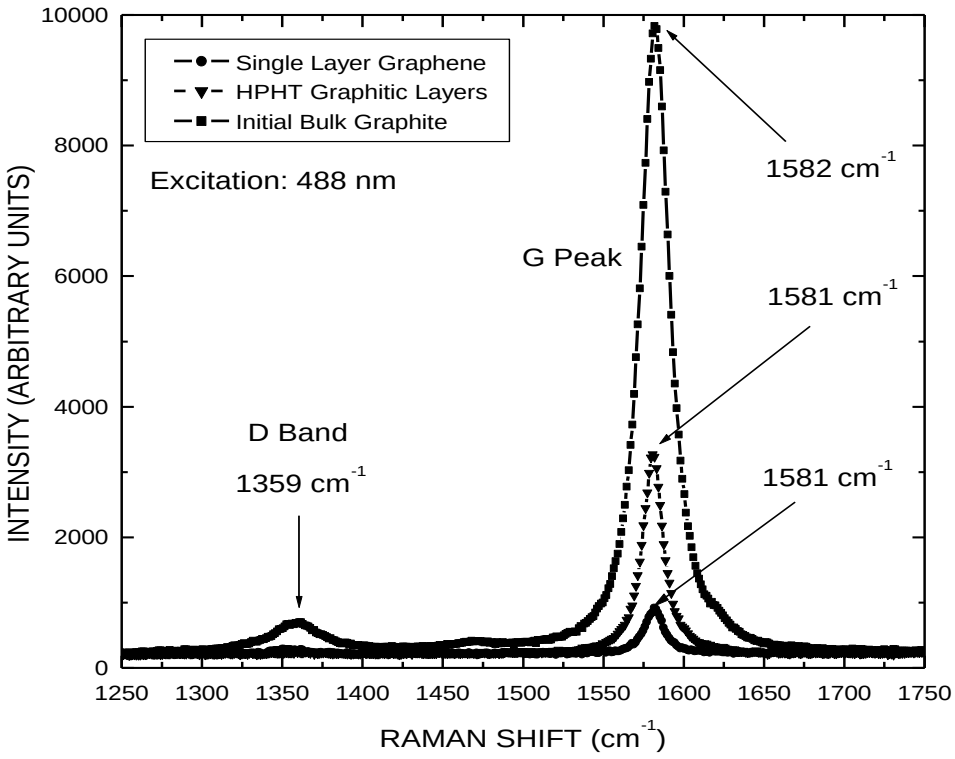

Figure 3.7: Raman spectrum of the initial natural bulk graphite source, as-produced HPHT graphitic layers and single-layer graphene in the *G*-peak region. Note that the disorder-induced *D* band is very strong in the spectra of the initial bulk graphite and it is completely absent in the spectra of graphene. This suggests the material quality improves during the growth process via melting and re-crystallization. Reproduced in part with permission from: F. Parvizi, D. Teweldebrhan, S. Ghosh, I. Calizo, A.A. Balandin, H. Zhu and R. Abbaschian, Micro and Nano Letters, 3, 1, 29-34 (2008). Copyright 2008. Institution of Engineering and Technology.

The absence of the *D* band indicates that HPHT graphene has higher crystalline order and lower defect concentration. The latter was attributed to the fact that in HPHT process carbon is completely dissolved with the help of the molten *Fe – Ni* catalysts and purified during its transport to a growth site and following re-crystallization. One should note here that the stage when carbon is dissolved is suitable for its chemical doping. From the further examination of the figure, one can see that the *G*-peak intensity decrease as

one goes from the initial bulk graphite to as-grown HPHT material, and to the single layer graphene is expected due to the reduction in the number of the interacting carbon atoms.

3.3.2 Raman Detection of DNA polymers

Using Raman Spectroscopy we were able to show that single strand DNA (ss-DNA) fragments act as negative potential gating agents that increase the hole density in graphene. Patterning of bio-molecules on graphene could provide new avenues to modulate the electrical properties. Current-voltage characterization of this hybrid ss-DNA / graphene system indicates a shift of the Dirac point and "intrinsic" conductance after ss-DNA is deposited. The effect of the ss-DNA is to increase the hole density in the graphene. The increased hole density is calculated to be 2×10^{12} cm^{-2}. This increase is consistent with the Raman frequency red shift in the G peak and 2D band and the decrease of the full width half max values (FWHM) in the G peak. Ab initio calculations using density functional theory rule out significant charge transfer or modification of the graphene band structure in the presence of the ss-DNA fragments [17].

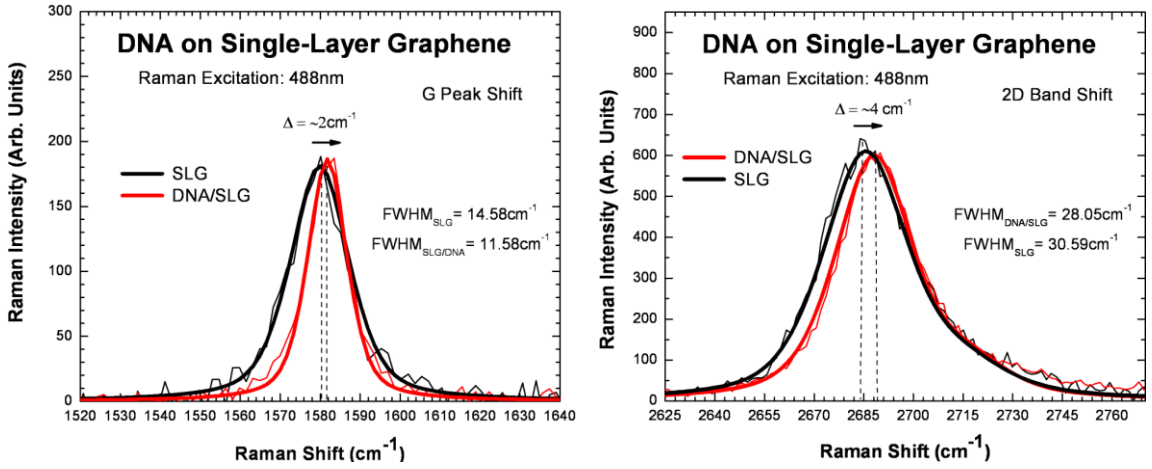

Figure 3.8: Micro-Raman spectroscopy of the signature G-peak and 2D band for pristine graphene and DNA/graphene based system. In (a) the G-peak centered at 1580 cm^{-1}, seen at 488 nm excitation wavelength, shifts and average 2 cm^{-1} after DNA coating. In (b) second order 2D band shifts a value of ~4 cm^{-1} as a result of DNA coating. Both signature peaks also show relative shortening of their respective full width half max values (FWHM) as a result of coating as well. More details on Ref. [17].

3.3.3 Thermal Characterization of Suspended Graphene

Using Raman Spectroscopy we investigation thermal conduction of suspended graphene across trenches in Si/SiO_2 wafer. The measurements were performed using a non-contact micro-Raman spectroscopy based technique developed by Dr. Alexander A. Balandin at UC Riverside. This 'optothermal' technique is based on the different amounts of power dissipated in graphene films, while corresponding temperature rise is determined from the spectral positioning and integrated intensity of graphene's *G* mode.

As the electronic industry moves towards nanometer designs, one of the most important challenges as was mentioned in the motivations is the growing chip power consumption. As the performance of ultra-large scale integrated (ULSI) circuits depends

on temperature *T*, even a small increase in *T* results in reduction of the device lifetime [18]. A possible approach for solving the thermal problem is finding a material with extremely high thermal conductivity *K*, which can be integrated with Si complementary metal-oxide-semiconductor (CMOS) technology. To solve some of these problems, carbon based methods have been considered for such thermal management applications [19-20].

The applicability of material for thermal management also depends on its suitability for integration with CMOS technology. Crystalline diamond and CNTs have proven to be rather difficult materials in this respect. To investigate the thermal properties of graphene, we used Si/SiO_2 substrates with an array of trenches fabricated by the reactive ion etching (RIE). The nominal depth of the RIE trenches was ~300 nm while the trench width *D* varied in the range 1 – 5 μm. Among the samples we selected long graphene flakes with a relatively constant width *W* suspended over the trenches and connected through the few-layer graphene regions to large graphitic pieces at the distance of few μm from the trench edges. The suspended single-layer graphene (SLG) flakes were located with the help of Raman spectroscopy [8-9]. Several long graphene flakes suspended across trenches with the flake length *L* longer than the width, i.e. $L>>W$.

None of the conventional techniques for measuring thermal conductivity of material worked well for the atomically-thick graphene layers. For this reason, Balandin's optothermal method is the best method for studies of thermal transport across suspended confined structures. Here, the laser light is focused in the middle of the

suspended SLG with the spot size of about ~1 μm [23]. A fraction of the excitation light (λ=488 nm) is absorbed by graphene, which results in the heating power P_G, while the remaining light is absorbed by the trench. Due to the small cross-sectional area of the heat conducting channel, even a small power dissipated in graphene can lead to a detectable rise of the local temperature [24].

The heat transport in graphene layer in our experiment is at least partially diffusive. The latter is expected from the phonon MFP data reported for a rather similar material system such as suspended CNTs [21-22, 26-27]. It was found that MFP in CNTs is ~ 250 – 750 nm at RT [26]. In our setup, the distance from the trench edge to multilayer graphite heat sink was in the range 6 – 10 μm. The temperature rise ΔT_G in the middle of the suspended portion of graphene can be established by measuring the shift in position of the graphene *G* peak $\Delta\omega$ and using the peak temperature coefficient χ_G, which we reported earlier [24]. In this case, the micro-Raman spectrometer acts as a thermometer, which gives $\Delta T_G=\Delta\omega/\chi_G$. Although the measurements were performed at RT we induced substantial heating in the middle of the suspended portion of the graphene flake. The average temperature rise along the length of the graphene flake was about ~70-100K.

For the plane-wave heat front propagating in two opposite directions from the middle of SLG, we can write $K=(L/2a_GW)(\Delta P_G/\Delta T_G)$. Here ΔT_G is the change in the temperature in the suspended portion of graphene flake due to the change in the power ΔP_G dissipated in graphene. Finally, the thermal conductivity can be determined as here

$$K = (L/2a_G W)\chi_G(\Delta\omega/\Delta P_G)^{-1}. \qquad [3.1]$$

the power absorbed in SLG can be written as $P_G = \alpha_G a_G(1+R_{Si})I_o A$, where A is the illuminated area, I_o is the laser intensity on the surface, α_G is the absorption coefficient in graphene and R_{Si} is the reflection coefficient of Si. Here we took into account the power, which is reflected from the Si trench and absorbed by the suspended portion of graphene.

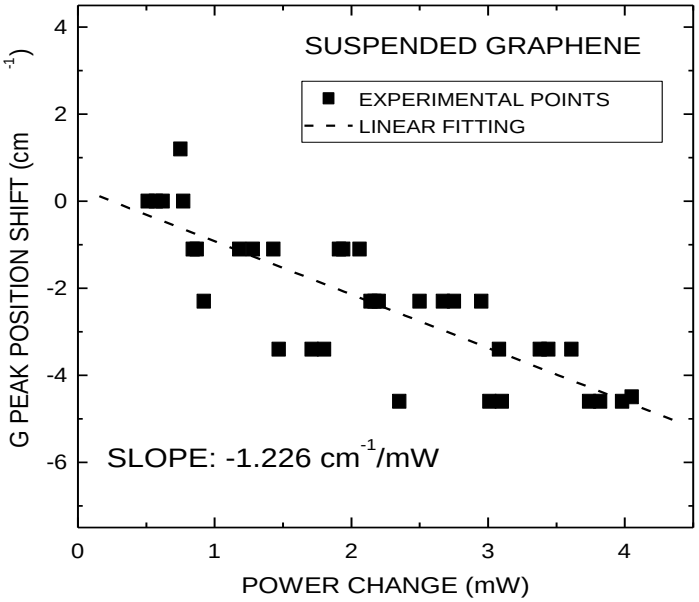

Figure 3.9: The shift in *G*-peak spectral position vs. change in total dissipated power. The slope of the dependence is used for the extraction of the thermal conductivity of graphene. Reprinted with permission from: S. Ghosh, I. Calizo, D. Teweldebrhan, E.P. Pokatilov, D.L. Nika, and A.A. Balandin, *Applied Physics Letters*, 92, 151911 (2008). Copyright 2009, American Institute of Physics.

Figure 3.9 shows a change in the *G* peak position with the total dissipated power P_D for a typical suspended SLG. In this figure the peak position change $\Delta\omega$ is referenced to the value at the lowest excitation power. The extracted slope is $\Delta\omega/\Delta P_D \approx -1.226$ cm-

^{1}/mW. Knowing calibrated intensity of G peak in graphene vs. HOPG for a given sample and power range one can recalculate the measured slope into the value of $\Delta\omega/\Delta P_G$. Using χ_G = – 1.6 ×10^{-2} cm^{-1}/K [24] and plugging into Eq. (1) the values of a_G, L, $\Delta\omega/\Delta P_G$ we obtain for the examined set of SLG samples the averaged values in the range K~ 3080 – 5150 W/mK. One should note that the upper bound of K for graphene is higher than the conventionally accepted values for individual CNTs [21-22].

3.4 Discussion

The process of peeling of graphene from HOPG pieces is not well-controlled, provides only small size graphene flakes, which are time consuming to produce and hardly can be scaled up with standard HOPG and Kish graphite sources. The reported alternative techniques of looking at HPHT molten methods of graphene synthesis provide an advantage to other methods such as radio-frequency plasma-enhanced chemical vapor deposition (PECVD) [9], high-vacuum graphene growth by Si sublimation from 6H-SiC or 4H-SiC (0001) surface [10], electrostatic deposition [11], as well as chemical methods [12]. It was shown that large area graphitic material by HPHT methods were synthesized in the split sphere growth apparatus, which is conventionally used for diamond growth [14].

We observe important implication of extremely high thermal conductivity of graphene for possible use for thermal management in future ULSI circuits. While SLG is

hard to produce, graphene multi-layers are much cheaper and are expected to retain most of the excellent heat conducting property. Graphene layers can be naturally attached to larger graphitic pieces acting as heat sink, thus avoiding the problem of thermal contact resistance, which is a major problem for CNTs. The flat plane geometry of graphene simplifies its integration with Si CMOS circuits for the purpose of thermal management.

From the Wiedemann-Franz law we estimated that the contribution of electrons to the thermal conductivity is less than 1% at RT. From this we can evaluated the phonon MFP Λ in graphene from the expression $K=\frac{1}{2}CV\Lambda$, where C is the specific heat and V is the averaged phonon velocity. The coefficient $\frac{1}{2}$ appears due to the two-dimensional nature of SLG. Using similarity of graphene and CNT material parameters and the data provided in Ref. [26], we estimated from our K values that MFP in graphene is $\Lambda \sim 775$ nm near RT.

3.5 Summary

The changes in the Raman spectrum of graphene allows one to identify the number of graphene layers, crystal quality analysis, thermal detection, and monitoring change in carrier concentration were discussed. The procedure for producing large area graphene films using an HPHT method were shown as a new method for growth of the high-quality large-area graphene layers from the natural graphite. The proposed method may lead to a larger scale graphene synthesis and a possibility of the efficient purification

and chemical doping of graphene during the melt phase of the growth. The evolution of the disorder *D* peak as one goes from the initial source carbon to the graphitic layers and then to graphene suggests that the density of the defects reduces and the quality of material improves. We were able to demonstrated that ss-DNA fragments act as a negative potential gating agents that increase the hole density in graphene. Heat transport in graphene layer could be determined by monitoring the temperature rise ΔT_G in the middle of suspended portion of graphene by measuring the shift in position of the graphene *G* peak $\Delta\omega$ and using the peak temperature coefficient χ_G. This allows micro-Raman spectrometer to act as a thermometer, which gives $\Delta T_G=\Delta\omega/\chi_G$. Although the measurements were performed at RT, the induced substantial heating in the middle of the suspended portion of the graphene flake. These results are important for extending the application of Raman spectroscopy of graphene for a wide variety of graphene and graphene-based devices applications.

References

[1] K.S. Novoselov, A. K. Geim, S. V. Morozov, D. Jiang, Y. Zhang, S.V. Dubonos, I.V. Grigorieva, and A. A. Firsov, *Science*, **306**, 666 (2004).

[2] F. Miao, S. Wijeratne, Y. Zhang, U.C. Coskun, W. Bao, and CN Lau, *Science*, **317** 1530 (2007).

[3] A .C. Ferrari, J.C. Meyer, V. Scardaci, C. Casiraghi, M. Lazzeri, F. Mauri, S. Piscanec, D. Jiang, K.S. Novoselov, S. Roth, and A.K. Geim, *Phys. Rev. Lett*. **97**, 187401 (2006); A. Gupta, G. Chen, P. Joshi, S. Tadigadapa, and P.C. Eklund, *Nano Letters* **6**, 2667 (2006).

[4] I. Calizo, D. Teweldebrhan, W. Bao, F. Miao, C. N. Lau, and A. A. Balandin, *J. Phys. C*.,**190**, 012008 (2008).; I. Calizo, F. Miao, W. Bao, C.N. Lau and A.A. Balandin, *Appl. Phys. Lett*., **91**, 071913 (2007).

[5] R.P. Vidano, D.B. Fischbach, L.J. Willis, T.M. Loehr, *Solid State Comm*., **39**, 341 (1981).

[6] P.H. Tan, Y.M. Deng and Q. Zhao, *Phys. Rev. B*, **58**, 5435 (1998).

[7] P.H. Tan, S. Dimovski and Y. Gogotsi, *Phil. Trans. R. Soc. Lond. A*, **362**, 2289 (2004).

[8] C. Thomsen and S. Reich, *Phys. Rev. Lett*., **85**, 5214 (2000).

[9] J.J. Wang, M.Y. Zhu, R.A. Outlaw, X. Zhao, D.M. Manos, B.C. Holloway, V.P. Mammana, *Appl. Phys. Lett*., **85**, 1265 (2004).

[10] J. Hass, R. Feng, T. Li, X. Li, Z. Zong, W.A. de Heer, P.N. First, E.H. Conrad, C.A. Jeffrey, and C. Berger, *Appl. Phys. Lett*., **89**, 143106 (2006).

[11] A.N. Sidorov, M. M. Yazdanpanah, R. Jalilian, P. J. Ouseph, R. W. Cohn, and G. U. Sumanasekera, *Nanotechnology*, **18**, 135301 (2007).

[12] S. Horiuchi, T. Gotou, M. Fujiwara, T. Asaka, T. Yokosawa, and Y. Matsui, *Appl. Phys. Lett*., **84**, 2403 (2004).

[13] F.P. Bundy, *Science*, **137**, 1057 (1962).

[14] Y.N. Palyanov, Y. Malinovsky, Y.M. Borzdov and A.F. Khokryakov, *Doklady Akademii Nauk SSSR*, **315**, 233 (1990).

[15] R. Abbaschian, H. Zhu, and C. Clarke, *Diamond & Related Materials*, **14**, 1916 (2005).

[16] F. Parvizi, D. Teweldebrhan, S. Ghosh, I. Calizo, A. A. Balandin, H. Zhu, and R. Abbaschian, *Micro & Nano Lett.*, **3**, 29 (2008).

[17] J. Lin, D. Teweldebrhan, K. Ashraf, G. Liu, X. Jing, Z. Yan, R. Li, M. Ozkan, R.K. Lake, A.A. Balandin, and C.S. Ozkan, *Small*, **6**, 1150 (2010).

[18] A. Vassighi and M. Sachdev, *Thermal and Power Management of Integrated Circuits*, Springer, New York, NY, (2006).

[19] S. Jin and H. Mavoori, *J. Electron. Mat.*, **27**, 1148 (1998).

[20] M.J. Biercuk, M.C. Llaguno, M. Radosavljevic, J.K. Hyun and A.T. Johnson, *Appl. Phys. Lett.*, **80**, 2767 (2002); S.T. Huxtable, D.G. Cahill, S. Shenogin, L. Xue, R. Ozisik, P Barone, M. Usrey, M.S. Strano, G. Siddons, M. Shim, and P. Keblinski, *Nature Materials*, **2**, 731 (2003).

[21] P. Kim, L. Shi, A. Majumdar, and P. L. McEuen, *Phys. Rev. Lett*., **87**, 215502 (2001).

[22] E. Pop, D. Mann, Q. Wang, K. Goodson, and H. Dai, *Nano Lett*., **6**, 96 (2006).

[23] M. Kuball, S. Rajasingam, A. Sarua, M. J. Uren, T. Martin, B. T. Hughes, K. P. Hilton, and R. S. Balmer, *Appl. Phys. Lett.*, **82**, 124 (2003).

[24] A. A. Balandin, S. Ghosh, W. Bao, I. Calizo, D. Teweldebrhan, F. Miao, and C. N. Lau, *Nano Lett.*, 8, 902 (2008); S. Ghosh, I. Calizo, D. Teweldebrhan, E.P. Pokatilov, D.L. Nika, A.A. Balandin, W. Bao, F. Miao and C. N. Lau, *Appl. Phys. Lett.*, **92**, 15, 151911 (2008); S. Ghosh, W. Bao, D.L. Nika, S. Subrina, E.P. Pokatilov, C.N. Lau and A.A. Balandin, *Nature Materials*, **9**, 7, 555, (2010).

[25] I. Calizo, A. A. Balandin, W. Bao, F. Miao, and C. N. Lau, *Nano Lett*., **7**, 2645 (2007).

[26] C. H. Yu, L. Shi, Z. Yao, D. Y. Li, and A. Majumdar, *Nano Lett.*, **5**, 1842 (2005).

[27] H. Y. Chiu, V. V. Deshpande, H. W. C. Postma, C. N. Lau, C. Miko, L. Forro, and M. Bockrath, *Phys. Rev. Lett.*, **95**, 4 (2005).

[28] C. Nolen, G. Denina, D. Teweldebrhan, B. Bhanu, and A. A. Balandin, *ACS Nano*, **5**, 914 (2011).

Chapter 4

Low-Energy Electron-Beam Irradiation Effects on Graphene and Graphene Devices

4.1 Motivations

Graphene characterization and device fabrication require an extensive use the scanning electron microscopy (SEM), transmission electron microscopy (TEM) and focused ion beam (FIB) processing. These and related techniques involve electron beam (e-beam) irradiation of the samples, which may result in damage and disordering. The radiation induced defects are expected to lead to significant deterioration of the electron and heat conduction properties. Despite the importance of this issue for device applications no investigation of the e-beam effects on graphene properties has been reported so far. In addition to the practical significance, the influence of the irradiation on graphene properties is of major fundamental science interest. A wide variety of physical properties

of carbon nanostructures is determined by the possibility of influencing their lattice structure, including by inducing defects.

4.2 Defects and Disorder in Carbon Materials

One of the methods for modifying the properties of carbon materials is the formation of defects through e-beam irradiation [1]. The effect of the particle and sub-particle irradiational interaction with bulk graphite has been studied extensively due to graphite applications in thermal nuclear reactors [2-4]. At the same time, no irradiation data is available for single-layer graphene (SLG) and bi-layer graphene (BLG). Here we report the first investigation of the modification in graphene lattice induced by the low and medium energy e-beam irradiation.

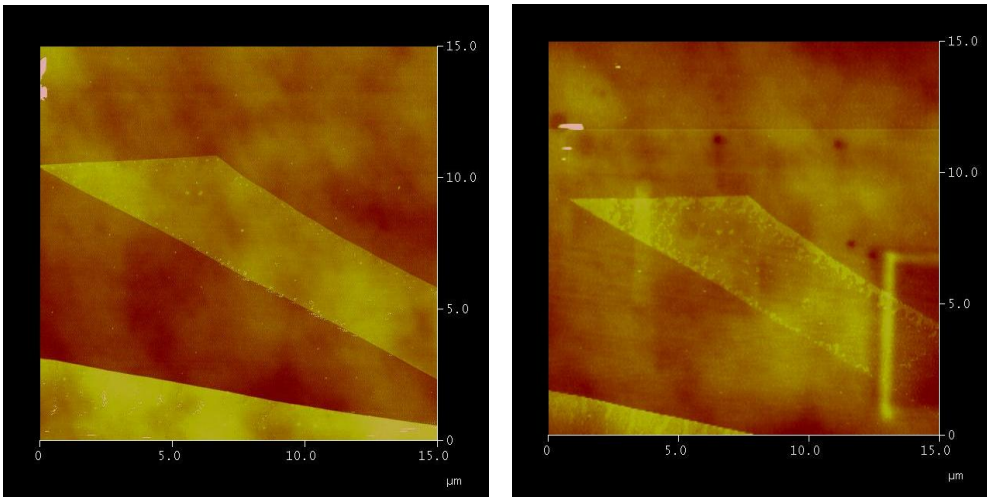

Figure 4.1: AFM topography indicates differences between irradiated and non-irradiated graphene.

4.2.1 Raman Spectrum of Disordered Graphene

Raman spectroscopy methods are capable for detecting small changes in the crystal structure and have been used extensively in the analysis of the irradiation damage on other carbon and carbon-based nanostructure materials [3, 5, 6]. These possible consequences of the irradiation would lead to changes in the vibration, i.e. phonon modes of graphene. For this reason we studied micro-Raman spectroscopy effects that result from electron beam irradiation in graphene and graphene field effect transistors (GrFETs). As few tuning methods of graphene properties have been studied, new methods for controllably modifying the properties of graphene is by introducing different concentration of disorder or defects to its pristine crystal structure.

4.3 Experimental Results

We report micro-Raman investigation of changes in the phonon modes of single layer and bi-layer graphene induced by the low and medium energy electron-beam irradiation. All Raman spectra were measured using Renishaw micro-Raman spectrometer under the 488 nm excitation. The spectra were recorded in the backscattering configuration through 50x objective at RT. In order to prevent local heating the excitation power was kept below 2.0 mW. Previously, it was established that Raman spectrum of graphene is rather sensitive to the temperature variations [8].

Graphene samples were produced by the mechanical exfoliation from three different types of initial carbon material: (i) bulk highly oriented pyrolitic graphite (HOPG), (ii) Kish graphite and (iii) high-pressure high-temperature (HPHT) graphitic layers. Graphene synthesis through HPHT process were determine to have high quality also as discussed in the previous chapter (section 3.3.1) and details can be found in Ref. [9]. For this reason we refer to the material as graphene whether it was produced from HOPG or HPHT source. All graphene flakes were placed on the standard Si/SiO_2 (300 nm) substrates and initially identified with an optical microscope.

4.3.1 Graphene Susceptibility to Electron-Beam Irradiation

SLG and BLG sample were isolated with the help of micro-Raman spectroscopy using a 2D-band deconvolution procedure [10]. The SEM image of graphene with indicated SLG and BLG regions is presented in Fig 4.2.

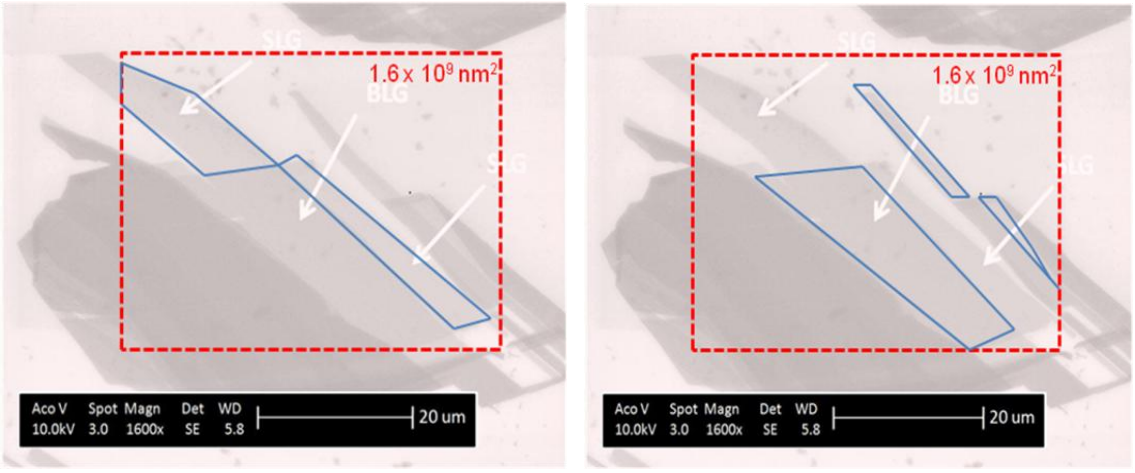

Figure 4.2: SEM of selected single layer and bilayer regions within fixed exposure area.

With low-energy acceleration energy, 5 keV - 20 keV, electron irradiation was performed with the help of the XL-30 FEG field-emission system. The graphene samples were subjected to continuous e-beam from the electron gun of the electron microscope focused on an area. In Fig. 4.2 it is shown an area of 1.6×10^9 nm^2 of exfoliated thin film regions with selected which contains both single layer and bilayer regions for investigation. Under a beam current of ~0.15 nA, irradiation is investigated with an electron beam dosage density of 3.905×10^{14} electrons $cm^{-2}s^{-1}$, depending upon the selected region (as the cross-section areas of SLG and BLG differ within the exposed regions).

To ensure free of contaminant, the samples were kept under vacuumed conditions with a base pressure at 8.5×10^{-4} Torr. A constant emission current of 235 μA is used throughout exposure for our samples. The working distance between the samples and the tip of the electron gun was kept at a relative constant distance, in the Fig. 4.2 the working distance WD = 6.0 +/- 1mm. Since the flux has been maintained constant for each of the experiments the electron dose is proportional to the irradiation time.

Time (Sec)	Irradiation Dosage (e^-/cm^2)
0	0
420	2.34×10^{16}
600	3.34×10^{16}
900	5.02×10^{16}
1200	6.69×10^{16}
1800	1.06×10^{17}
2700	1.51×10^{17}

Table 3: The irradiation dosage (fluency) of electron beams on graphene at ~0.15 nA beam current. With all variables fixed the dosage is depended on exposure time.

4.3.2 Raman Spectrum of Irradiated Graphene

In Figure 4.3 we show the effects observed in Raman spectra of SLG before and after electron beam irradiation exposure. As one can see, the graphene spectra manifest three important features: disorder D and zone-center G peaks near ~1350 cm^{-1} and ~1580 cm^{-1}, respectively, as well as the second-order 2D band and 2D' band at ~2700 cm^{-1} and ~3250 cm^{-1} under laser wavelengths of 488 nm and 633 nm.

It is important to notice here that in pristine graphene samples the disorder D peak is absent. The latter indicates the high quality of graphene and its crystalline nature. It should be noted the dependence of the D-peak intensity dependence different laser energies. Here both the 488 nm and 633 nm spectrums are taken at the same location with

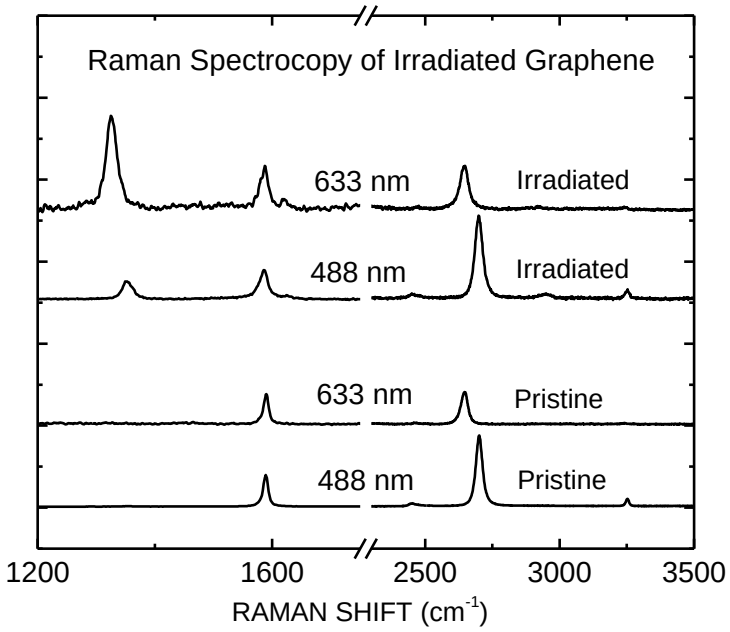

Figure 4.3: Raman spectra of graphene before and after e-beam irradiation under 488 nm and 633 nm laser excitation. Reprinted with permission from: D. Teweldebrhan and A.A. Balandin, *Applied Physics Letters*, 95, 246102 (2009). Copyright 2009, American Institute of Physics.

the same irradiative dosage. The D peak is made up of phonons of A_{1g} symmetry near the K-zone boundary. These phonons are not Raman active due to the momentum conservation in the scattering process. The peak only appears in the presence of defects or structural disorder [7]. A rather intriguing result is that even a very short time exposure, e.g. few minutes, of SLG to 20 keV e-beam irradiation leads to an appearance of large disorder D peak. The intensity of the D peak decreases with increasing dose of the irradiation. The G peak broadens under e-beam irradiation. The peak at ~1620 cm^{-1}, referred to as D', was detected after the second step of irradiation. This peak was attributed to the intra-valley double-resonance process in the presence of defects [11].

4.3.2.1 Non-monotonic I_D/I_G Defect Concentration

The irradiation-induced evolution of the Raman spectra of BLG is similar to that of SLG. The disorder D peak, completely absent in spectrum of pristine BLG, appears strong after few-minutes e-beam irradiation even for the low-energy excitation of 5 KeV. As a result of the low or medium energy irradiation, we are able to observe the appearance of a second-order combination D+D' band near 2940 cm^{-1} in both SLG and BLG. The appearance of D peak and broadening of G peak and 2D band indicate disorder as a result of e-beam irradiation. Another observation from these spectra is that the lattice damage in graphene appears at smaller e-beam energies and exposure times (few minutes) as compared to other carbon materials. For examples, the exposure times utilized to induce similar damage in carbon nanotubes (CNTs) were few hours rather than minutes [6].

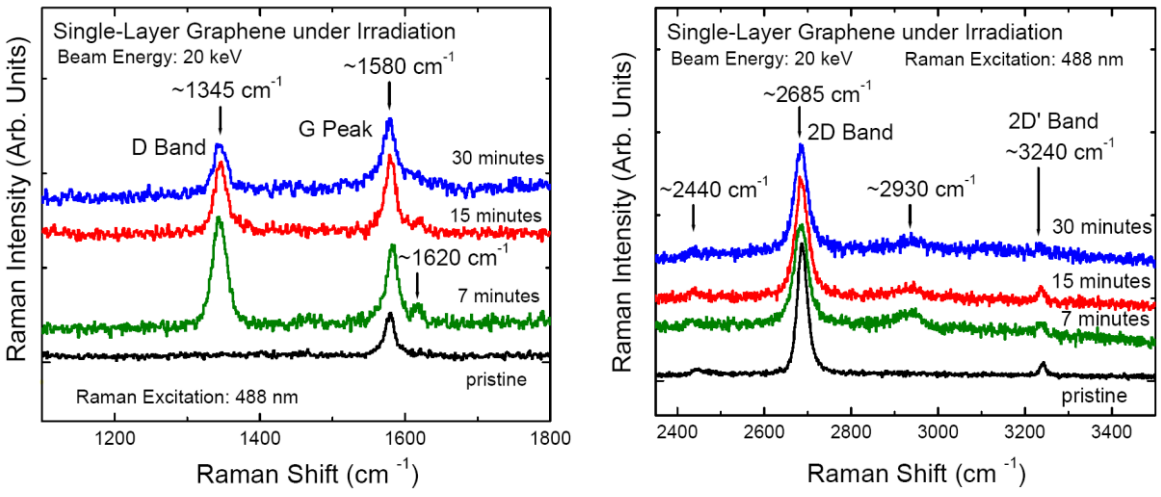

Figure 4.4: First order and second order Raman spectrums for Irradiated graphene. Reprinted in part with Premission: D. Teweldebrhan and A.A. Balandin, *Applied Physics Letters*, 94, 013101 (2009). Copyright 2009, American Institute of Physics.

To rationalize these results, we plotted the ratio of D and G peak intensities I(D)/I(G) as a function of the e-beam irradiation time (see Fig. 4.5). After the first few minutes of irradiation the ratio I(D)/I(G) attains its maximum and then falls rapidly. The continuation of the irradiation results in a slower decrease or saturation of I(D)/I(G). This trend was observed for both SLG and BLG in the examined e-beam energy ranges (5-20 keV). It is illustrative to compare the dependencies in Fig. 4.5 with the amorphization trajectory proposed by Ferrari and Robertson for the disordered, amorphous and diamond – like carbon [7, 12]. The trends summarized by the amorphization trajectory indicate that I(D)/I(G) increases as one goes from graphite to nanocrystalline (nc) graphite and then decreases with increasing disorder when material becomes more of an amorphous-like nature. This amorphization trajectory appears suited well for our case when crystalline graphene under e-beam irradiation first transforms into nanocrystalline phase and then, as the radiation damage increases, becomes more disordered.

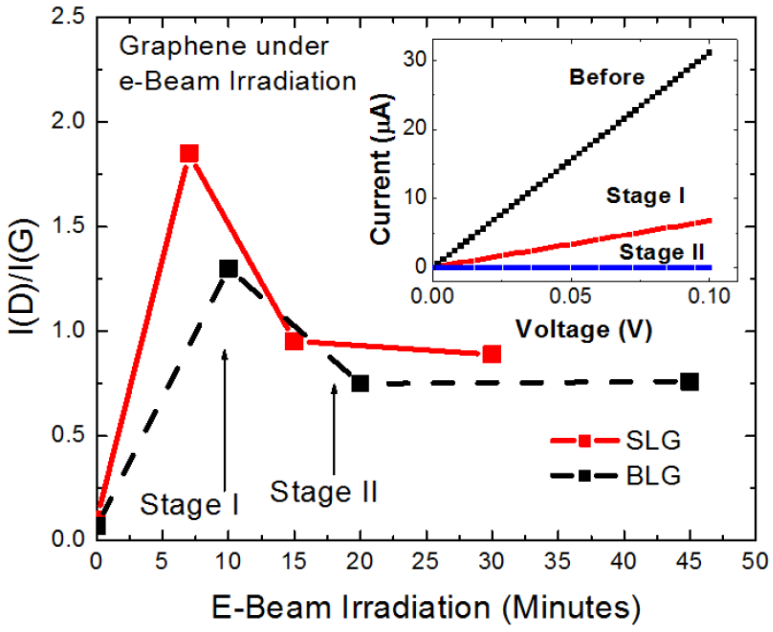

Figure 4.5: Evolution of the ratio of the intensities of the D andG peaks as a function of the irradiation exposure for single layer (SLG) in red and bilayer graphene (BLG) in black. Using Tuintra-Koening relation of grain size to Irradiation fluence was determined. Reprinted in part with Premission: D. Teweldebrhan and A.A. Balandin, *Applied Physics Letters*, 94, 013101 (2009). Copyright 2009, American Institute of Physics.

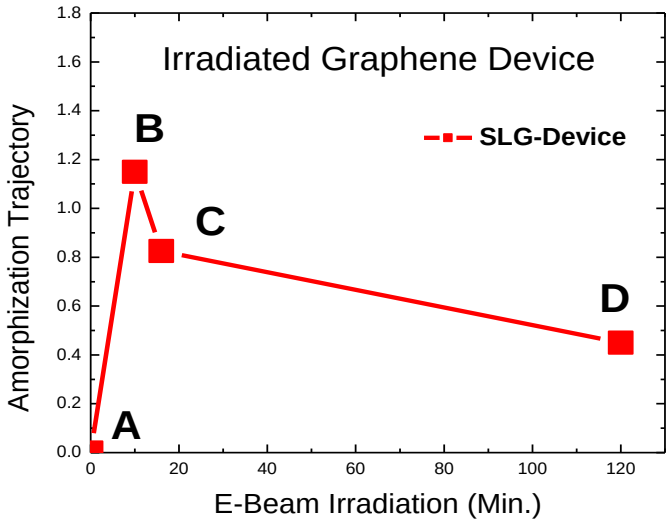

Figure 4.6: Evolution of the ratio of the intensities of the D andG peaks as a function of the irradiation for single layer (SLG) giving a 1/T or 1/La like dependence for up to 2hrs of irradiation.

It's known that the presents of the D-peak is clear indication of defects and disorder, but as a result of broadening of all selective graphitic peaks within the Raman spectra (i.e. D, G, and 2D) a possible detectable method for understanding the quantity or nature of disorder which is currently unknown [12, 13]. We take a look at the effect exposure duration has on the FWHM of single layer graphene. As a result of irradiation, the FWHM in SLG shows an initial spike broadening and levels off for the closely related D and 2D peaks. With changes of ~12 cm^{-1} and 24 cm^{-1} after seven minutes of exposure, respectively. In graphene, a relative doublet structure relation between the D peak and 2D peak seems to be reserved. This is not the case for multilayer graphene, as the 2D band shows and increasing FWHM with increased irradiation time. The 2D band is used for identifying the number of graphene layers and posses a strong indication of c-axis ordering as well as slight curvature effects in sing walled carbon nanotubes [10].

We carefully also examined the Raman spectrum and electrical transport effects of graphene based field effect transistors after each irradiation step. The details of irradiation process of graphene devices and electrical transport effects will be discussed more in section 4.3.4. Here we analysis the Raman spectrum seen in these devices. In work discussed above, we had varied the acceleration energy between 5-20 keV under a constant beam current of ~0.15 nA. Here we observe the effects of using a beam current in ~pA range for a longer duration to match the same dosage levels as our prior analysis.

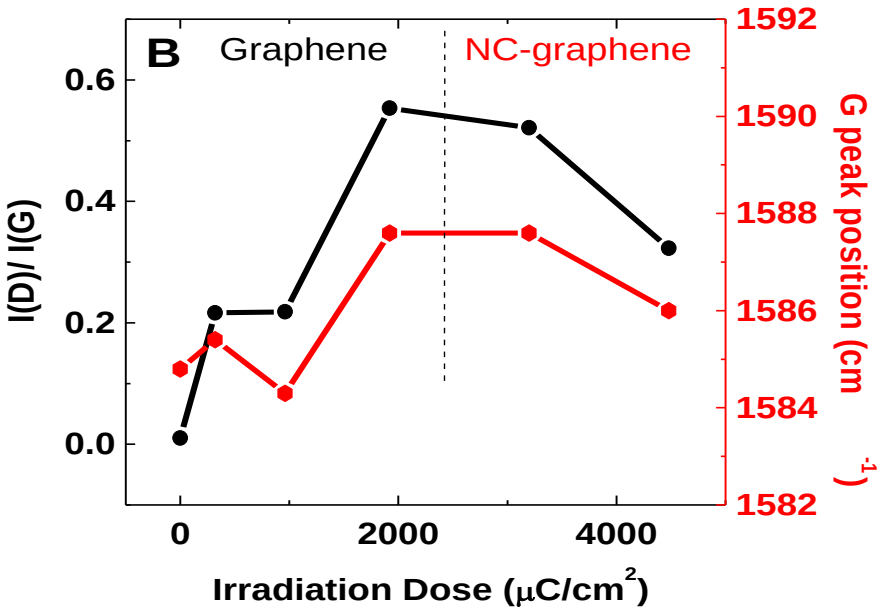

Figure 4.7: I(D)/I(G) ratio for irradiation under 30 pA is shown. These trends suggest the graphene experience a structure change from graphene to nanocrystalline graphene.

As can be seen in Figure 4.7, we notice that a disorder D peak appears after the electron beam irradiation. The ratio I(D)/I(G) reveals a clear and reproducible non-monotonic dependence on the irradiation dose. This behavior was observed in all devices and the trend is consistent with our earlier studies. A similar trend was reported for graphite where the ratio I(D)/I(G) was also increasing with the irradiation dose. At these low levels of beam current (~pA) it was seen that the intensity of I(D)/I(G) ratio is suppressed in SLG as compared to previous (~nA) measurements. The bond breaking in such cases is likely chemically induced since the electron energy is not sufficient for the ballistic knock out of the carbon atoms, ~86 keV [14]. Generally increased 2D peak FWHM width, together with the generally decreased I(2D)/I(G) ratio in the first 4 steps of irradiation indicating the accumulation of the charge impurities [18]. This phenomenon

is consistent with the I(D)/I(G) evolution. The abrupt change of the last step may due to a difference defect mechanism from a phase change. Other factors contributing to the growth of the disorder D band can be contaminant molecules or water vapor, which dissolve under irradiation and may form bonds with the carbon atoms of the graphene lattice.

The change in the G peak position under the electron beam irradiation is also shown in Fig. 4.7. The G peak position shifts to higher wave numbers with increasing irradiation dose (with exception for the 2^{nd} step). But after certain dose (step four) the peak position starts to move to the lower wave numbers. A similar trend was also observed in graphite [7]. It is reasonable to believe that e-beam irradiation leads to disorder in graphene's crystal lattice via formation of defects and sp^3 bonds.

4.3.3 Selective Irradiation and Nano-Patterning of Graphene

We look at the possibility of selective area irradiation using e-beam to pattern regions of single layer graphene. Below, in Figure 4.8, is an optical image and schematic of single layer graphene region and schematics illustrating controlled irradiational sectioning of regions in red. Raman spectra mappings of respective G-Peak, 2D-band, D-peak, and ID/IG ratio both prior and post electron beam irradiation show that sharp features that separate each respective region. We also note that can the single layer regions are more susceptible to irradiation that the few layer regions. Other possible mechanisms for E-beam patterning methods of single layer graphene include (i) Direct contact metal on graphene, (ii) Masking shadowing, or (iii) direct writing.

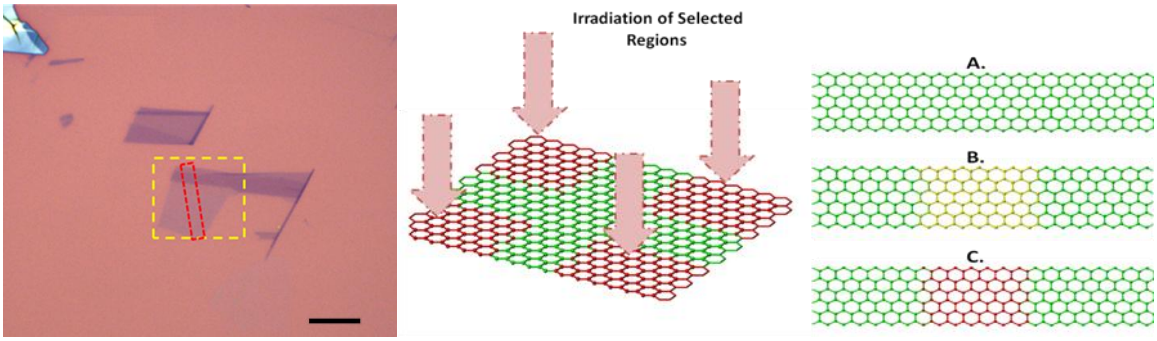

Figure 4.8: Selective area irradiation using e-beam to pattern regions of single layer graphene. (a) Optical image of single layer graphene region and schematics illustrating controlled irradiational sectioning of regions.

.

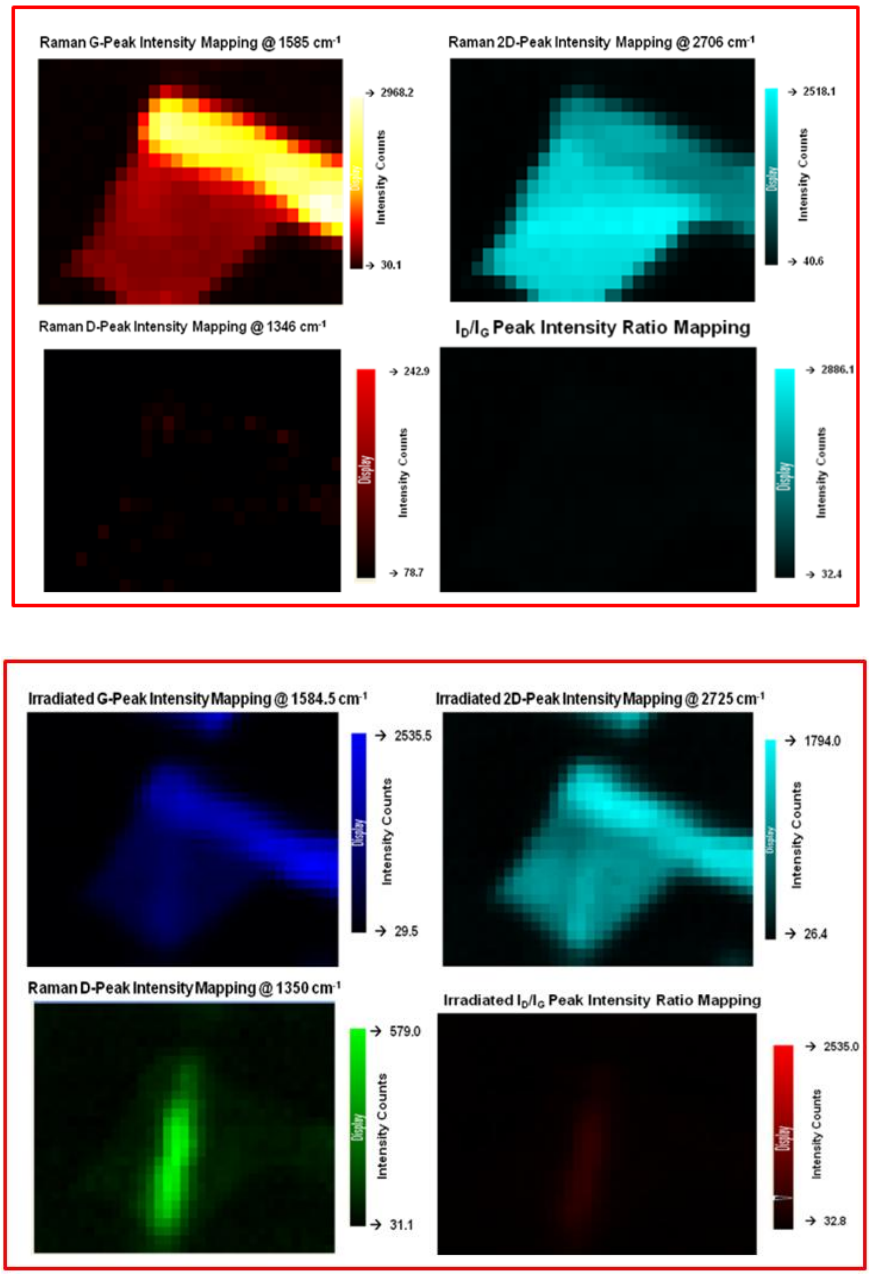

Figure 4.8 continued: Raman spectra mappings of respective G-Peak, 2D-band, D-peak, and ID/IG ratio both prior (b) and post (c) electron beam irradiation. It can be seen that the single layer regions are more susceptible to irradiation that the few layer regions.

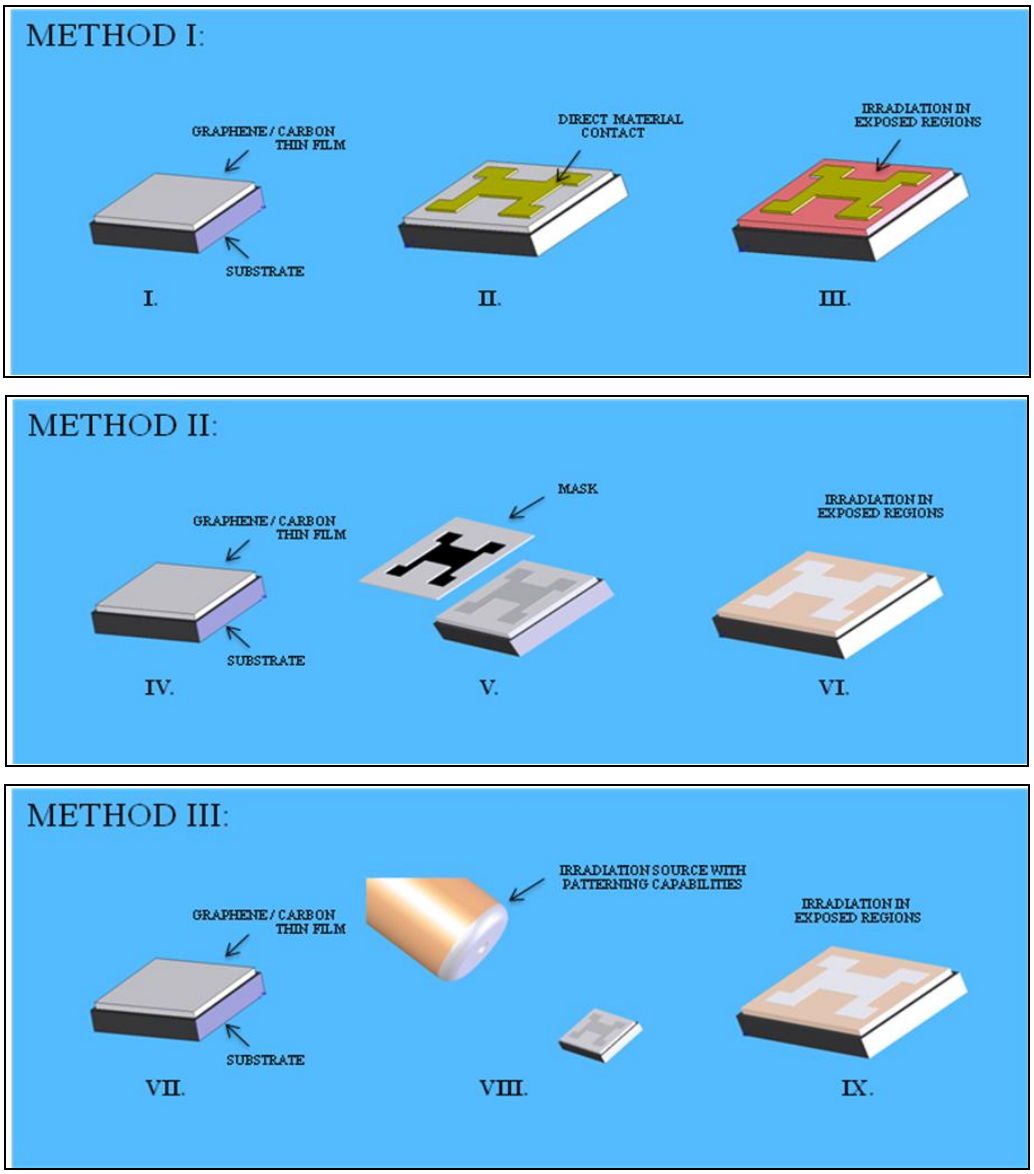

Figure 4.9: Three possible mechanisms for e-beam patterning methods of single layer graphene. (i) Direct contact metal on graphene, (ii) Masking shadowing, or even as we have demonstrated (iii) direct writing.

4.3.4 Tuning of Graphene Devices via Electron Irradiation

It's important to understand how the corresponding electrical transported properties of irradiated single layer graphene as a function irradiation dose. Here, a compare the correlate the current – voltage characteristics with the evolution of Raman spectrum of electron beam irradiated GrFETs. Graphene back-gate devices were fabricated with the electron beam lithography (EBL). We defined the source and drain regions and then followed with evaporation of Cr/Au with thickness of 10 nm and 60 nm respectively. The graphene back gate devices were fabricated with the electron beam lithography (EBL). We conducted electron beam irradiation using Leo SUPRA 55 electron-beam lithography (EBL) system, which allows for accurate control of the exposed area and irradiation dose. Special precautions have been taken to avoid additional unintentional e-beam irradiation. The alignment program in the utilized EBL system offers a way to scan only the alignment marks without exposing other locations. We used the gold alignment marks located more than 30 μm away from the graphene device to avoid unintentional irradiation during the scanning steps.

For these experiments we selected the accelerating voltage of 20 keV and the working distance of 6 mm (the same as in EBL process). The area dosage was calculated and controlled by the nanometer pattern generation system (NPGS). NPGS allowed us to control the scanning distance from point to point and set the dwelling time on each point. The beam current, used in calculation of the irradiation dose, was measured using a Faraday cup. The beam current for all the irradiation experiments in this work was 30.8

pA. The experiments were conducted in a following sequence. First, the back gated graphene devices were irradiated with a certain dose of electrons. Second, the irradiated graphene devices were examined using micro-Raman spectroscopy to detect any changes with the Raman signatures of graphene. Third, the current-voltage (I-V) characteristics were measured to examine the changes of electrical properties. After I-V data were collected, the irradiation dose was increased and all steps repeated.

The electron beam irradiation was performed inside the SEM vacuum chamber with a low pressure (10^{-7} Torr) whereas the Raman spectroscopy and electrical measurements were carried out at ambient conditions. The electrical measurements were performed with an Agilent 4142B instrument. The devices and irradiation process were intentionally designed in such a way that only graphene channel is exposed to the e-beam while the metal contacts are not irradiated. The latter allowed us to avoid any possible changes in metal contact resistance after the irradiation.

We started by measuring the electrical resistance between the source and drain as a function of the applied gate bias. Fig. 4.10 shows the evolution of the electrical characteristics of SLG device after each irradiation step. The electron irradiation dose for each step is indicated in the figure's legend. As one can see, the ambipolar property of graphene is preserved after irradiation within the examined dosage range. The observed up shift of the curves indicates increasing resistivity of graphene over a wide range of carrier concentration. The increase is especially pronounced after the 4^{th} step with a higher irradiation dose (1280 $\mu C/cm^2$).

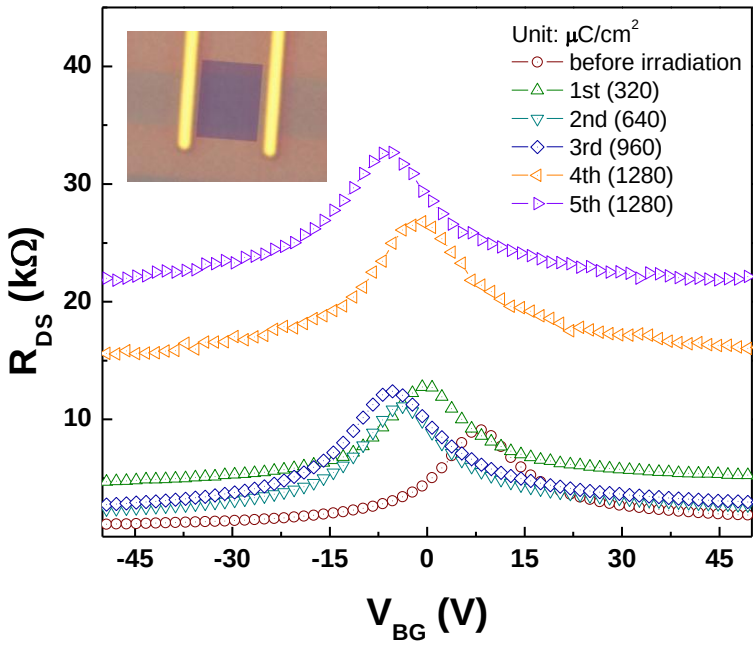

Figure 4.10: Transfer characteristics of SLG evolution with increasing dosage of irradiation. The irradiation dosage for each step is noted. The inset is the optical image of a typical graphene device. The metal electrodes are used as source and drain, and heavily doped silicon is used as back gate electrode. The light blue strip is graphene flake. The purple rectangular region is the irradiation area which covers all the graphene part between source and drain while excludes two electrodes in case of any possible changes of contact brought by the irradiation in the experiment.

In order to analyze the results and rule out the role of the contact resistance we used the following equation to fit our resistance data [18, 19]:

$$R_{DS} = R_{Cont} + \frac{L}{W}\left(\frac{1}{e\mu\left(\sqrt{n_0^2 + n_{BG}^2}\right)}\right) + \frac{L}{W}\rho_{irr} \qquad [4.1]$$

where R_{Cont} is the contact resistance, μ is the mobility, e is the elementary charge, L and W are the length and width of the channel, respectively. In Eq. (1) n_0 is the background

charge concentration due to random electron – hole puddles [15] and n_{BG} is the charge induced by gate bias calculate from the equation:

$$n_{BG} = \frac{C_{BG}\left|V_{BG} - V_{BG,\min}\right|}{e}, \qquad [4.2]$$

where C_{BG} is the gate capacitance per unit area taken to be 0.115 mF for 300 nm SiO_2 substrate.

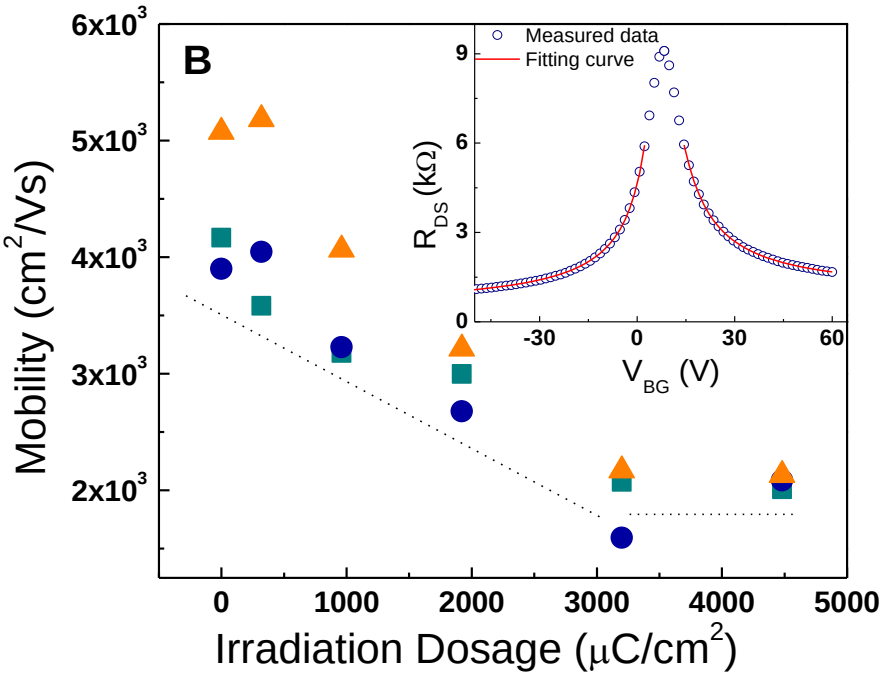

Figure 4.11: Mobility of 3 SLG devices decreases almost linearly with irradiation dosage. After the 4th step the inset shows fitting result of one device. Adapted from Ref. [19].

The inset to Figure 4.11 shows the result of the fitting Eq. 4.1 and 4.2 to the data R_{DS} for SLG device before e-beam irradiation. Note that the fitting does not cover the interval close to the charge neutrality point because this region is characterized by a large uncertainty in the data. The fitting was conducted separately for the negative and positive

gate bias regions. For simplicity, curve fitting results are from the p-type branch. The fitting gives the contact resistance of 446 Ω, the initial mobility μ=5075 cm^2/Vs, and the charge impurity concentration of 2.13×10^{11} cm^{-2}, which are very close to the typical values for clean graphene samples [17]. During the experiments the irradiated regions excluded the contacts. For this reason, the contact resistance should not change during the measurements and we can estimate the resistance of the irradiated graphene channels by subtracting the contact resistance from the total resistance. To fit our results for irradiated graphene devices we modified equation provided by adding the term $R_{Ird,}=(L/W)\rho_{Ird}$, which is the resistance increment induced by e-beam irradiation. Fig. 4.11 also shows the evolution of the mobility due to e-beam irradiation for three SLG devices. We note that the mobility decreases almost linearly and drops by 50~60% over the examined irradiation dose.

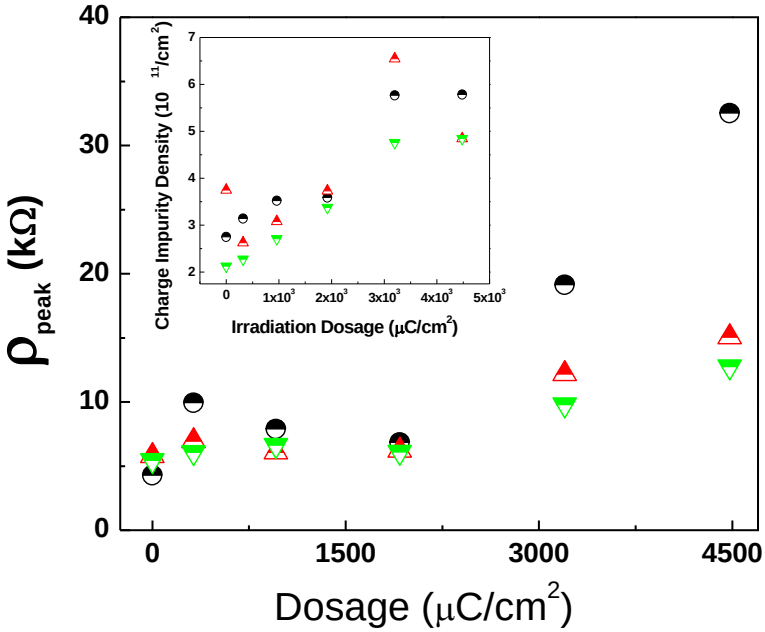

Figure 4.12: Evolution of SLG resistivity with irradiation dosage. Inset shows the effect of e-beam irradiation on charge impurity density for SLG.

The decrease of the I(2D)/I(G) ratio was previously attributed to increasing concentration of charged defects or impurities [18]. Our electrical measurements are consistent with this interpretation indicating a growing density of the charged impurities with increasing irradiation dose (see inset to Fig. 4.12). Fig. 4.12 shows evolution of the resistivity near the charge neutrality point with the irradiation dose. One can see a clear trend of increasing ρ_{max} with the irradiation dose. Since the contacts were not irradiated during the experiment, the overall increase of device resistance is due to the increasing resistivity of the irradiated graphene. This can be understood by the induced defects that create an increasing number of scattering centers in the graphene lattice. Note that the ρ_{max} increases by a factor of ~ 3 to 7 for SLG devices.

4.3.5 Thermal Reversibility in Irradiated Graphene

It was discovered that the irradiation induced changes in the properties of SLG are reversible to some degree. The I-V characteristics can be at least partially recovered by annealing or storing the devices over a long period of time in a vacuum box. The annealing may help to repair the bonds and clean the surface from the organic residues while keeping devices in vacuum may be as a result of loss of the irradiation induced charge. As can be seen in Figure 4.13, the electron beam irradiation trajectory on our SLG devices is altered as the annealing is incorporated during the process. When the sample is annealed at ~510 K for a few minutes, we note the diminishing of the I(D)/I(G) ratio, as can be seen indicated in red between irradiation trials 1-2, 4-5, and 7-8. We also observe how other thermal treatment methods, which are commonly known for removal of absorbents that may adhere on the surface of graphene under ambient conditions and

differentiate how they differ from the effect that irradiation creates on our graphene devices. Under ambient conditions, Raman Spectroscopy does not indicate absorbents on the surface of graphene for typical graphene samples both before and after common pre-heating processes. While electrical transport measurement are relatively very sensitive to such absorbents as shown by the minimum conducting point shifting and drastic mobility enhancements. To minimize such adsorbents, irradiation is conducted under vacuum conditions and then annealed. This way we are assured that the disordered D-peak appearance and removal as a result of our post annealing process is solely introduced as a result of irradiation based defects or disorders created in the graphene devices. Ambient condition disorders do not create D-peaks in graphene, while irradiation disorders do.

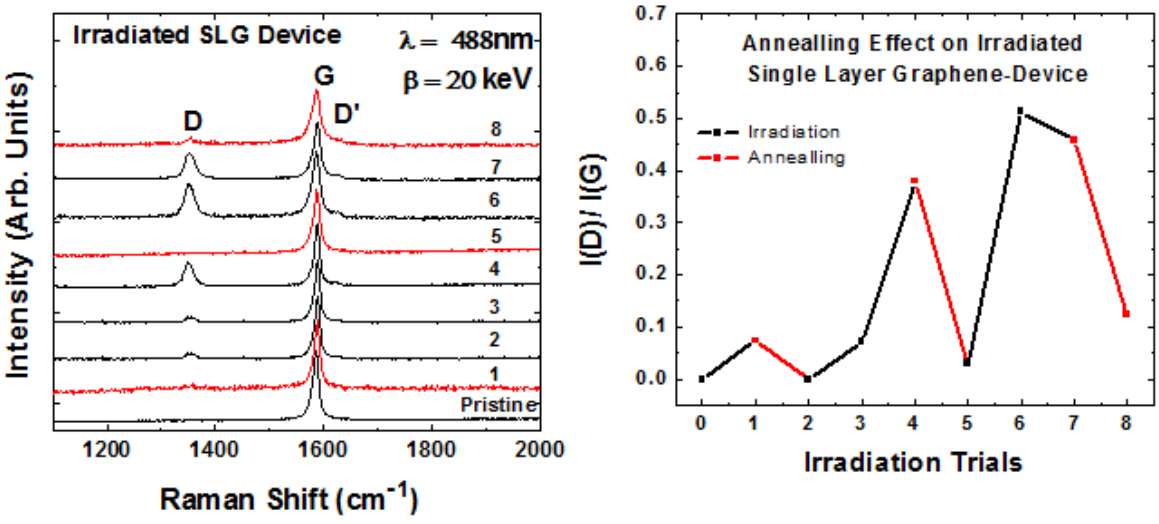

Figure 4.13: a) SLG devices is altered as the annealing is incorporated during the process at ~500K. b) The diminishing effect due to annealing of the I(D)/I(G) ratio, can be seen indicated in red between irradiation trials 1-2, 4-5, and 7-8.

As result of vacuum pumping using a mechanical pump system we also observe the restoration of graphenes electronic properties. It also can be seen that over a two month period of high vacuum treating the resistance measurements of vacuum treated graphene device resemble to that of pre-irradiated conditions. Under such conditions, the mobility actually almost returns to its original value. The latter suggests that the e-beam irradiation results in creation of the charged defects, which are more efficient in carrier scattering than neutral defects.

The devices was exposed to an *insitu* electron beam irradiation at varies dosages and the drain-source current (I_{ds}) was monitored at changing drain-source voltage (V_{ds}) from 0 – 100 mV range. The electron kinetic energy was held constant at 20 keV. It should be noted that the electron energy of 20 keV is considered to be much less destructive than lower energies, such as 5 keV and 1 keV [20]. General electrical measurements trends of our samples, indicates the electric properties of single and few layer graphene device were converted from being highly conductive material, before exposure to irradiation, to that of an electrically insulating amorphous material after Stage II simply by low-energy electron irradiation [13]. At stage I of the amorphization trajectory for single layer graphene, when crystalline graphene under e-beam irradiation transforms into *nc* phase, electrically the irradiated thin films show semi-conductive properties and shows that defects formed acts as a transport barrier.

The temperature dependence of the device characteristics after relative irradiation dosages was also examined. After just a few minutes of electron irradiation around nano-crystalline graphene (nc-G), it was seen that as a result of sweep annealing from

temperature 300K to 500K of whole device atop a heating chuck that partial restoration of the crystalline structure is observed and depicted to be consistent from Raman spectra's across exposed regions of the graphene plane. Previously, we were able to observe quenching effects that indicated semiconductor behavior in our pristine graphene devices [27]. We observed that there are much less effects observed in restorations resulting from the amount of annealing time at a particular temperature in pristine graphene as compared to the annealing temperature after irradiation. The Raman spectrums are indicative of such changes that result from annealing an irradiated graphene device at beam energy of 20 keV.

We carried out transport measurements of drain-source current (I_{ds}), which was monitored at changing drain-source voltage (V_{ds}) from 0 – 100 mV ranges for these devices verify the effects we observe in our Raman analysis. Restoration of electrical properties in a single layer graphene device was observed as deformation effects of electron beam irradiation was altered and fluctuated as a result of annealing. The characteristic I_{ds} vs. V_{ds} are plotted and show that a 1.5 kΩ resistance for pristine graphene before irradiation was measure when a small voltage of 0.1V was applied. After irradiation exposure dose density of ~ 5.02 x 10^{16} e^-/cm^2, the resistance in the device was increased to about 5 kΩ, corresponding to structural deformation in graphene to the nc-G phase. As a result of annealing at 500 K, we are able to obtain restoration in I-V characteristic back to a more conductive resistance of 1.75 kΩ. Similar results were observed as a result of Joule heating in crystalline graphene ribbons [26]. Reversibility back to pristine properties from nc-G are possible and relative amount of reconstruction

of crystalline structure is dependent on annealing temperature. This was not the case for exposure dose density exceeding 1.0 x 10^{17} e^-/cm^2, where amorphous sp^2 only is present. Annealing up to 600 K for time periods exceeding 2 hours fail to create restoration within the electronic properties of the graphene device.

It can be seen that the significant changes result in suppression of the appearance of relative disorder related Raman peaks at ~1350 cm^{-1} and ~1620 cm^{-1}. This is consistent with annealing results also for graphite obtained by others [21, 22]. From amorphization trajectory of graphene and the Tuinstra – Koening [24] relation, experimental results have shown their strong dependence on each other as I_D/I_G decreases with that of increasing grain size (L_a) [23, 24].

The obtained results have important implications for graphene characterization and graphene device fabrication, which relay on the electron microscopy and focused ion beam processing. The graphene I(D)/I(G) ratio dependence on the irradiation time is consistent with that reported for multi-wall CNTs [17] but required less exposure to produce noticeable changes. The precise nature of the defects caused to SLG and BLG lattice is not clear at present. The threshold acceleration voltage of knock-on damage, i.e. ballistic ejection of an atom, for single-wall CNTs is about 86 keV [30, 31]. Assuming that the threshold is similar for graphene, the radiation modification in the lattice induced in our case must be different from the knock-on damage.

It is known from the theory of heat conduction in graphene that the lattice thermal conductivity can be strongly reduced by the defects and disorder [30-32]. The small-dose

irradiation can become an effective tool for shifting the position of the minimum conduction point or inducing a carrier transport gap. The low-energy e-beam irradiation is known [6-7] to produce substantial damage, including bond breaking, in carbon nanotubes (Ref. [7] 1 keV electrons with the dose up to 8×10^{17} cm^{-2} were used). In graphite, some of the radiation defects can be removed after low temperature treatment. For example, Niwase [8] studied the irradiation-induced amorphization of graphite and reported that many defects were repaired at temperature ~473 K.

It was recently shown that graphene devices reveal a rather low level of $1/f$ noise but can degrade as a result of aging and environmental exposure. The e-beam irradiation may lead to further increase in the noise level in graphene devices. For this reason, special protective cap layers may be required for communication and radiation-hard applications. From the other side, the e-beam irradiation may lead to a new method of *defect engineering* of graphene physical properties. The controlled exposure of graphene layers to electron beams can be used to convert certain regions to the highly resistive or electrically insulating areas needed for fabrication of graphene circuits. Irradiation can also be used to reduce the intrinsically high thermal conductivity to the very low values required for the proposed thermoelectric applications of graphene.

4.4 Summary

In general, the expected changes due to the irradiation include the transformation of the crystalline sp^2 lattice into disordered state; displacement of atoms from the lattice;

radiolysis; excitation of phonons and Plasmon, or attachment of random water molecules. It was shown that the single layer graphene is much more susceptible to e-beam irradiation than bilayer and few layer graphene films. The appearance of the disorder induced D peak in graphene. The mobility and electrical resistivity of graphene devices can be varied by the e-beam irradiation over a wide range of values. As a result of thermal annealing and vacuum pumping levels it is shown that some restoration can also occur in the Raman spectra and electrical properties, respectively. The obtained results may lead to a new method of defect engineering of graphene properties. The results also have important implications for fabrication of graphene nano-devices, which involve scanning electron microscopy and electron beam lithography.

The obtained results have important consequences for graphene device fabrication. From one side, the high sensitivity of graphene to e-beam irradiation can be exploited for controllable modification of graphene crystal structure at nanoscale, i.e. nanofabrication. For example, certain regions of SLG, which is a perfect conductor of electricity and heat, can be easily converted to electrical and thermal insulators by e-beam irradiation with accurately selected radiation doses. The latter can be useful in fabrication of graphene interconnects for nanoscale circuits. From another side, these results suggest that graphene device applications in the systems subjected to radiation, e.g. working in radiation hard conditions of outer space, require additional protection layers or special shielding.

References

[1] M. Takeuchi, S. Muto, T. Tanabe, S. Arai and T. Kuroyanagi, *Philos. Mag. A*, **76** 691 (1997).

[2] K. Niwase, *Phil. Mag. Lett*., **82**, 401 (2002); K. Niwase, *Mat. Sci. and Eng. A*, **400**, 101-104 (2005).

[3] J. Liu, M. D. Hou, C. Trautmann, R. Neumann, C. Muller, Z. G. Wang, Q. X. Zhang, Y. M. Sun, Y. F. Jin, H. W. Liu, H. J. Gao, *Nucl. Instrutruments and Methods Phys. Res. B*, **212**, 303-307 (2003).

[4] M. Zaiser, and F. Banhart, *Phys. Rev. Lett.*, **79**, 3680 (1997).

[5] G. Compagnini, and G. Baratta, *Appl. Phys. Lett.*, **61**, 1796 (1992).

[6] S. Gupta, and R. J. Patel, *J. Raman Spectrosc.*, **38**, 188 (2007).

[7] A. C. Ferrari, and J. Robertson, *Phys. Rev. B*, **61**, 14095 (2000).

[8] I. Calizo, A.A. Balandin, W. Bao, F. Miao, and C. N. Lau, *Nano Lett.*, **7**, 2645 (2007).

[9] F. Parvizi, D. Teweldebrhan, S. Ghosh, I. Calizo, A. A. Balandin, H. Zhu, and R. Abbaschian, *Micro & Nano Lett*., **3**, 29 (2008).

[10] A.C. Ferrari, J. C. Meyer, V. Scardaci, C. Casiraghi, M. Lazzeri, F. Mauri, S. Piscanec, D. Jiang, K. S. Novoselov, S. Roth, and A. K. Geim, *Phys. Rev. Lett*., **97**, 187401 (2006); A. Gupta, G. Chen, P. Joshi, S. Tadigadapa, and P. C. Eklund, *Nano Lett.*, **6**, 2667 (2006).

[11] D. C. Elias, R. R. Nair, T. M. G. Mohiuddin, S. V. Morozov, P. Blake, M. P. Halsall, A. C. Ferrari, D. W. Boukhvalov, M. I. Katsnelson, A. K. Geim, and K. S. Novoselov, *Science*, **323**, 610, (2009).

[12] A. Ferrari, *Solid State Comm.*, **143**, 47 (2007).

[13] K. Sato, R. Saito, Y. Oyama, J. Jiang, L.G. Cancado, M.A. Pimenta, A. Jorio, Ge.G. Samsonidze, G. Dresselhaus, M.S. Dresselhause, *Chem. Phys. Lett.*, **427**, 117 (2006).

[14] D. Teweldebrhan and A. A. Balandin, *Appl. Phys. Lett*., **94**, 013101 (2009).

[15] D. Teweldebrhan and A.A. Balandin, *Appl. Phys. Lett.*, **95**, 246102 (2009).

[16] S. Kim, J. Nah, I. Jo, D. Shahrjerdi, L. Colombo, Z. Yao, E. Tutuc and S. K. Banerjee, *Appl. Phys. Lett.*, **94**, 062107 (2009).

[17] S. Adam, E. H. Hwang, V. M. Galitski, and S. Das Sarma, *PNAS*, **104**, 18392 (2007).

[18] Z. Ni, T. Yu, Z. Luo, Y. Wang, L. Liu, C. Wong, J. Miao, W. Huang and Z. Shen, *ACS Nano*, **3**, 569 (2009).

[19] G. Liu, D. Teweldebrhan, and A.A. Balandin, *IEEE Trans. Nanotech.*, (2010). DOI: 10.1109/TNANO.2010.2087391;

[20] S. Suzuki, S. Fukuba, K. Kanzaki, Y. Homma, and Y. Kobayashi, *Proc. 5th IEEE Conf. Nanotechnol.*, WE-A4-2, Nagoya, Japan, (2005).

[21] B. S. Elman, M. S. Dresselhaus, G. Dresselhaus, E. W. Maby, and H. Mazurek, *Phys. Rev. B*, **24**, 1027 (1981).; K. Sato, R. Saito, Y. Oyama, J. Jiang, L.G. Cançado, M. A. Pimenta, A. Jorio, Ge. G. Samsonidze, G. Dresselhaus and M. S. Dresselhaus, *Chem. Phys. Lett*., **427**, 117 (2006).

[22] R. B. Wright, R. Varma, and D.M. Gruen, *J. Nucl. Mater.*, **63**, 415 (1976).

[23] F. Tuinstra and J.L. Koening, *J. Chem. Phys.*, **53**, 1126 (1970).

[24] L.G. Canado, K. Takai, T. Enoki, M. Endo, Y.A. Kim, H. Mizusaki, A. Jorio, L.N. Coelho, R. Magalhaes-Paniago and M.A. Pimenta, *Appl. Phys. Lett*., **88**, 163106 (2006).

[25] J. Campos-Delgado, J. M. Romo-Herrera, X. Jia, D. A. Culle, H. Muramatsu, Y. A. Kim, T. Hayashi, Z. Ren, D. J. Smith, Y. Okuno, T. Ohba, H. Kanoh, K. Kaneko, M. Endo, H. Terrones, M. S. Dresselhaus, and M Terrones, *Nano Lett*ers, **8**, 2773 (2008).

[26] Q. Shao, G. Liu, D. Teweldebrhan and A. A. Balandin, *Appl. Phys. Lett*., **92**, 202108 (2008).

Chapter 5

Mechanical Exfoliation of Atomically-Thin Bi_2Te_3 Films

It has been predicted theoretically that the thermoelectric figure of merit *ZT* can be drastically increased in crystalline Bi_2Te_3 quantum wells with the thickness of just few atomic layers (~1 nm) owing to either charge carrier confinement or acoustic phonon confinement. Conventional chemical vapor deposition, electrochemical or other means are not suitable for fabrication of crystalline structures with such a thickness. In this chapter, we characterize and show that quasi 2-D crystals of bismuth telluride can be mechanically exfoliated following a "graphene-like" procedure. Stacks of quasi-2D layers of Te-Bi-Te-Bi-Te are members of a new type of recently discovered materials referred to as *topological insulators* (TIs)

5.1 Motivations

Bismuth telluride (Bi_2Te_3) is a unique material with a potential for diverse range of applications. Since the discovery of its extraordinary thermoelectric properties, Bi_2Te_3 has become a vital component for thermoelectric industry [1-3]. Bulk Bi_2Te_3-based materials are known to have the highest thermoelectric figure of merit, $ZT \sim 1.14$ at room temperature (RT). The thermoelectric figure of merit is defined as $ZT=S^2\sigma T/K$, where $S=-\Delta V/\Delta T$ is the Seebeck coefficient (ΔV is the voltage difference corresponding to a given temperature difference ΔT), σ is the electrical conductivity and K is the thermal conductivity, which has contributions from electrons and phonons. It is clear from ZT definition that in order to improve thermoelectric figure of merit one should increase the thermopower $S^2\sigma$ and decrease the thermal conductivity. Different approaches have been tried in order to enhance the thermoelectric properties of Bi_2Te_3 or its alloys. These approaches included the composition change from its stoichiometry, the use of polycrystalline materials with different grain sizes, intentional introduction of structural defects and incorporation of different dopants, e.g. Sb or Se, into Bi_2Te_3 lattice. The optimization of bulk Bi_2Te_3 led to incremental improvements but no breakthrough enhancement in ZT was achieved.

More promising results (ZT ~2.4 for p-type material at RT) were achieved with Bi_2Te_3/Sb_2Te_3 superlattices produced by the low-temperature deposition [4]. A recent study indicated that the low-dimensional structuring of BiSbTe alloys [5] also allows for

ZT enhancement to ~1.5 at RT. But still higher *ZT* values are needed for a major practical impact. It has been shown that *ZT* above 3 or 4 at RT are needed in order to make thermoelectric cooling or power generation competitive with conventional methods [6]. Such an increase in *ZT* would lead to a "thermoelectric revolution" and allow one for much more environmentally friendly power generation and cooling.

It follows from many theoretical predictions that a drastic improvement in *ZT* can be achieved in low-dimensional structures where electrons (holes) are strongly confinement in one or two dimensions [7]. Hicks and Dresselhaus [8] predicted that *ZT* can be increased in Bi_2Te_3 quantum well by a factor of ~13 over the bulk value. This would require a complete carrier confinement in a quantum well with a width *H* on the order of ~1 nm and an optimized position of the Fermi level. According to Dresselhaus *et al*. [7-8], quantum confinement of charge carries in quantum wells leads to a drastic *ZT* improvement due to the increase in the carrier density-of-states (DOS) near the Fermi level and corresponding increase in the thermopower. The crucial condition for such mechanism is quantum confinement of carriers in quantum wells, which is only possible if materials are crystalline and essentially free of defects. The thickness of the thin film required to achieve the quantum confinement conditions has to be on the order of few atomic layers. Note that in the superlattices commonly used in thermoelectric studies the charge carries are only partially confined if confined at all due to the small potential barrier height and relatively low material quality. The barrier height has a pronounced effect on *ZT*. Broido and Reinecke [9] have shown theoretically that *ZT*=3 can be achieved in Bi_2Te_3 superlattices with infinite potentials when the quantum well width (i.e.

thickness of the thin film) is H~3 nm. In the structures with incomplete quantum confinement the maximum ZT decreases to ~2.5 and the required width becomes as small as ~2 nm.

Balandin and Wang [10] proposed a different strategy for increasing ZT in low-dimensional structures by reducing its thermal conductivity via spatial confinement of acoustic phonons, which carry bulk of heat in thermoelectric materials. The improvement of thermoelectric properties via phonon engineering [10-11] also can be achieved in thin films or nanowires with the thickness of just few atomic layers and high quality of interfaces. In nanostructures with rough interfaces, the thermal conductivity can be reduced due to phonon scattering on boundaries and defects [12-14]. At the same time, defects and disorder can also lead to electron mobility degradation limiting the improvement. The phonon – confinement mechanism of the thermal conductivity reduction, proposed by Balandin and Wang [10], originates from the decreased phonon group velocity of the confined acoustic phonon modes, which results in the increased scattering on point defects [10-11]. This mechanism works even in atomic films with smooth interfaces and can be utilized without degrading the electron mobility.

Thus, in order to employ the full strength of the low-dimensional confinement effects for improving thermoelectric figure of merit either via the electron band-structure and phonon engineering one needs to produce quasi-two-dimensional (2D) structures with a few-atomic layer thickness and high quality interfaces. Conventional chemical vapor deposition, electrochemical or other means are not capable for producing such quality structures. Molecular beam epitaxy (MBE) of low-dimensional thermoelectric

materials was also much less successful than that of optoelectronic or electronic materials due to the lattice mismatch and other factors. These considerations create very strong motivations for the search of alternative approaches to fabrication of the stacks of quasi-2D crystals made of Bi_3Te_3-based materials.

5.2 Bi_2Te_3 Crystal Structure and Van der Waal Gaps

Bi_2Te_3 has the rhombohedral crystal structure of the space group D_{3d}^5 – R(-3)m with five atoms in one unit cell. The lattice parameters of the hexagonal cells of Bi_2Te_3 are a_H= 0.4384 nm and c_H = 3.045 nm [14]. Its atomic arrangement can be visualized in terms of the layered sandwich structure (see Figure 5.1). Each sandwich is built up by five mono-atomic sheets, referred to as quintuple layers, along the c_H axis with the sequence – [$Te^{(1)}$-Bi-$Te^{(2)}$-Bi-$Te^{(1)}$] – [$Te^{(1)}$-Bi-$Te^{(2)}$-Bi-$Te^{(1)}$] –. Here superscripts (1) and (2) denote two different chemical states for the anions. The outmost atoms $Te^{(1)}$ are strongly bound to three planar $Te^{(1)}$ and three Bi metal atoms of the same quintuple layers and weakly bound to three $Te^{(1)}$ atoms of the next sandwich. The binding between adjacent $Te^{(1)}$ layers originates mostly from the weak van der Waals forces although other long-range Coulomb forces play role in the bonding. The stronger bonds inside the quintuple layers are of the covalent or partially ionic nature. The presence of the van der Waals gap between the quintuples results in easy cleavage plane between adjacent $Te^{(1)}$ - Te(1) layers. The bond strength within the quintuple layers is not the same. The Bi-$Te^{(1)}$ bond is stronger than Bi-$Te^{(2)}$ bond, which is the second weakest point within the crystal

structure. It is believed that the Bi-Te(2) bond is covalent while the Bi-Te(1) binding includes both covalent and ionic interaction.

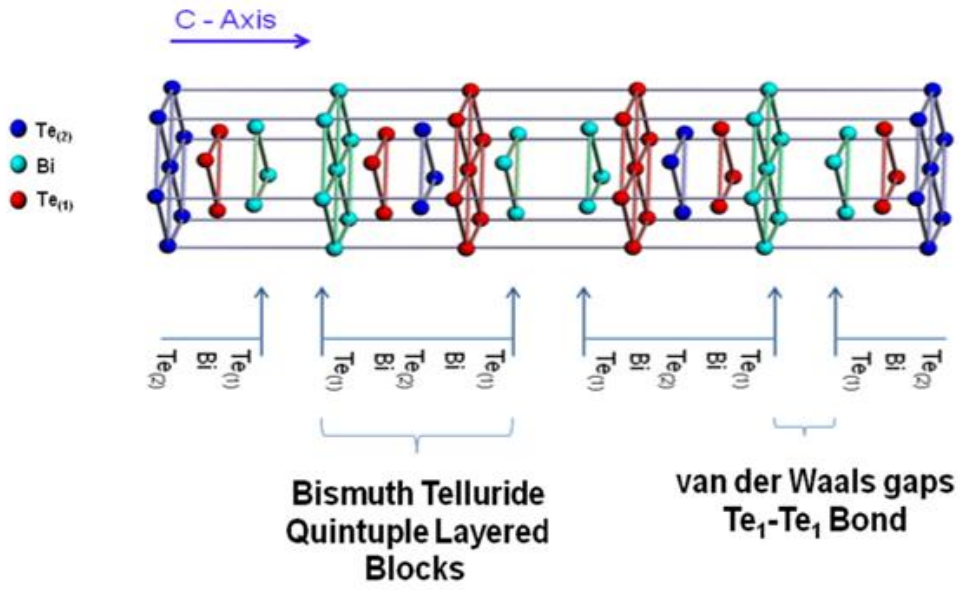

Figure 5.1: Schematic of Bi_2Te_3 crystal structure of D_{3d}^5 – R(-3)m space group showing quintuple layers and location of the van der Waals gaps. The $Te^{(1)}$-$Te^{(1)}$ bond is the weakest while Bi-$Te^{(1)}$ bond is the strongest. The mechanical exfoliation mostly results in breaking the $Te^{(1)}$-$Te^{(1)}$ van der Waals bond and formation of quintuples although in some cases intra-quintuples bonds also break leading to bi-atomic and tri-atomic layers.

5.3 Experimental Results

5.3.1 Exfoliation and Characterization

Here we look at the use of "graphene-inspired" exfoliation of crystalline bismuth telluride films with a thickness of a few atoms. The atomically thin films were suspended across trenches in Si/SiO_2 substrates, and subjected to detail material characterization.

The presence of the *van der Waals gaps* allowed us to disassemble Bi_2Te_3 crystal into its *quintuple* building blocks – five mono-atomic sheets – consisting of $Te^{(1)}$-Bi-$Te^{(2)}$-Bi-$Te^{(1)}$.

In order to isolate bismuth telluride quintuples and break them into atomic planes we employ a method similar to the one used for exfoliation of single-layer graphene [18-21]. Through a mechanical cleavage process we separated thin films from crystalline bulk Bi_2Te_3. The process was repeated several times to obtain the layers with just few-atomic planes. Owing to the specific structure of Bi_2Te_3 crystal along c_H direction (c_H = 3.045 nm is very large lattice constant as compared to other materials) we were able to verify the number of layers using the optical inspection combined with the atomic force microscopy (AFM) and the scanning electron microscopy (SEM). The thickness of the atomic quintuple is H~1 nm. The step-like changes in the cleaved layers highest of ~1 nm can be distinguished well with AFM. The produced atomic layers were placed on Si substrates containing 300 nm thick SiO_2 capping layer. The silicon oxide thickness was selected by analogy with that for graphene on Si/SiO_2 [18-21]. We then isolated and separate individual crystal planes which exhibited high crystal quality with little to no structural defects. The mechanical cleavage of Bi_2Te_3 has led to a high portion of quintuples with five atomic planes. In some cases we observed atomic planes with the thickness smaller than that of the quintuple layers. The produced flakes had various shapes and sizes ranging from ~2 μm to 30 μm. Some flakes had correct geometrical shapes indicative of the facets and suggesting the high degree of crystallinity. We selected large uniform Bi-Te flakes with the dimensions of ~ 20 – 30 μm for fabrication

of metal contacts for electrical characterization. For detail material characterization, we suspended some of the Bi-Te atomic films over trenches in SiO_2/Si substrates. The trenches were fabricated by the reactive ion etching (RIE). They had a depth of ~300 nm and widths ranging from 1 to 5 μm. By suspending the ultra-thin atomic films over these trenches we reduced the coupling to the substrate. The latter allowed us to achieve better understanding of the intrinsic properties of the atomically thin layers.

5.3.2 Atomically-Thin Crystal Characterization

The isolated Bi-Te atomic layers were investigated using a high-resolution field-emission scanning electron microscope (XL-30 FEG) operated at 10-15 kV. The diffraction patterns of the crystalline structures of the layers were studied using transmission electron microscopy (TEM). The sample preparation for TEM (FEI-PHILIPS CM300) inspection was carried out through ultrasonic separation in ethanol (C_2H_5OH) solution. The sonication was most effective with 500 μL of C_2H_5OH solution where the molar concentration of Bi-Te films was held at a constant 1.41 x 10^{-1} moles/liter throughout the solution. AFM studies were performed using VEECO instrument with the vertical resolution down to ~0.1 nm. Raman spectroscopy was performed for better material identification and characterization of intrinsic properties of the resulting films. A micro-Raman spectrometer (Renishaw RM 2000) was used in a backscattering configuration excited with a visible laser light (λ = 488 nm). The spectra were collected through a 50x objective and recorded with 1800 lines/mm grating providing the spectral resolution of ~ 1 cm^{-1} (software enhanced resolution is ~0.5 cm^{-1}).

All spectra were recorded at very low power levels P<0.5 mW measured with the power meter (Orion) at the sample surface. The low power levels were essential to avoid local laser heating, which was much more pronounced than in other material systems due to the extremely low thermal conductivity of Bi_2Te_3. The details of our Raman instrumentation and measurement procedures were reported by us earlier in the context of graphene investigation [22-24]. The electrodes and contact pads for the ultrathin Bi-Te layers on SiO_2 were fabricated and defined by the electron beam lithography (EBL) system (Leo 1550) followed by the metal deposition of 7-nm/70-nm Ti/Au metals with the electron beam evaporator (Temescal BJD-1800). The electrical measurements were carried out using a probe station (Signatone) at ambient conditions.

The quintuples, atomic tri-layers and bi-layers we were identified via combined optical, SEM, AFM and TEM inspection (see Supplemental Materials). Our prior extensive experience with graphene and few-layer graphene [22-24] was instrumental in our ability to separate weakly distinguishable optical features in Bi-Te atomic layers placed on SiO_2/Si substrates. A relatively large thickness of the unit cell (c_H = 3.045 nm) made SEM and AFM identification rather effective. The representative high-resolution SEM micrographs and AFM images presented in Figure 5.2 (a-f) show SEM, AFM and TEM images of Bi-Te quasi-2-D crystals with the lateral sizes ranging from a few microns to tens of microns. In Figure 5.2, one can see SEM micrograph of high quality crystalline films with the lateral dimensions of 1-4 μm and a thickness of few-atomic planes. Due to the atomic thickness of the films the overlapping regions are seen with a very high contract. The larger area flakes (>20 μm) tended to be attached to thicker

Bi_2Te_3 films (Figure 5.2 (b)). It was our experience that for thicker films the use of the tilted SEM images was more effective in visualizing the quintuples and atomic-layer steps. Although [$Te^{(1)}$-Bi-$Te^{(2)}$-Bi-$Te^{(1)}$] quintuple layers were more readily available among the separated flakes, some regions of flakes had sub-1-nm thickness and appeared as bound atomic planes of Te-Bi-Te or Bi-Te or even as mono-layers protruding from few-atomic-layer films. Figure 5.2 (c) show suspended few-quintuple and single quintuple films, respectively. In Figure 5.2 (d, e) we present a typical AFM image of steps in the separated films with clear layered structure. One step with the height of ~1 nm corresponds to a quintuple while two steps per a profile height change of ~ 1 nm indicate sub-quintuple units (e.g. bi-layer and a tri-layer). The structural analysis at the nanometer scale was carried out using TEM and the selected area electron diffraction (SAED) technique. The images for this type of characterization were taken with the electron beam energy of 300 kV. The exfoliated samples were dissolved in ethanol and placed on copper grids. The TEM image in Figure 5.2 (f) shows that the exfoliated Bi-Te flakes dissolved in solution retain their flat structure and do not form clusters after being subjected to ultrasonic vibrations and processing.

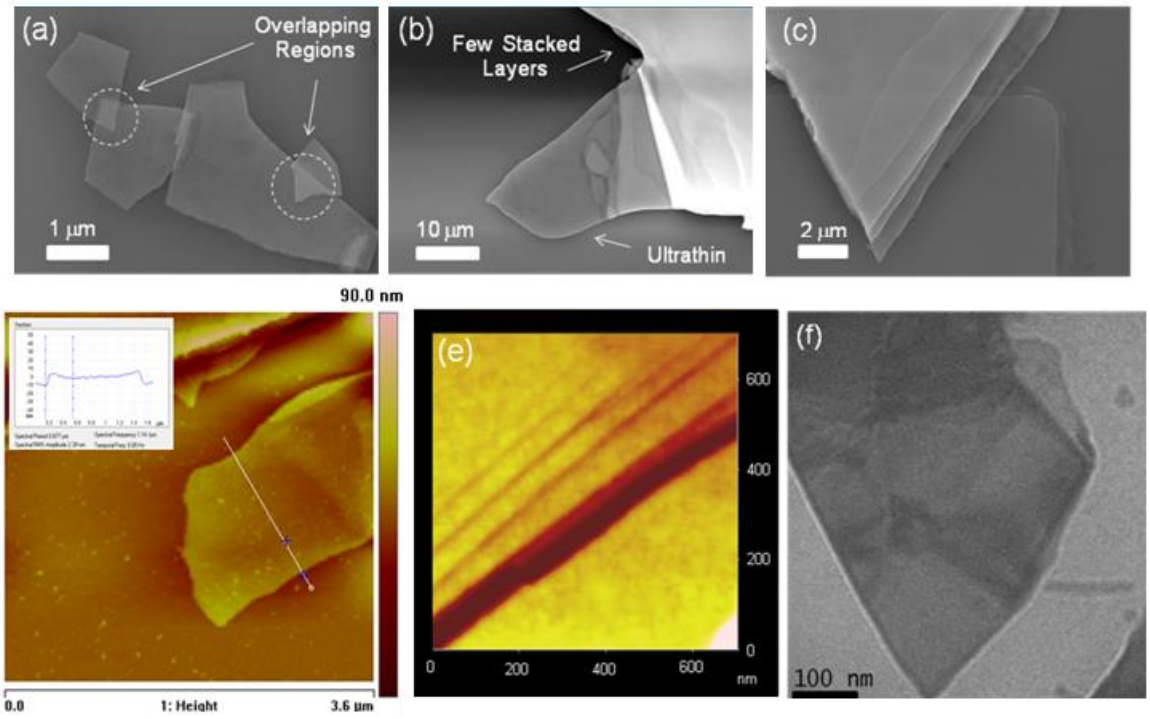

Figure 5.2: Images of quasi-2D bismuth telluride crystals showing (a) SEM micrograph of the overlapping few-layer Bi-Te atomic crystals; (b) large-area atomically-thin crystal attached to thick Bi_2Te_3 film; (c) suspended films with visible quasi-2D layers; (d) suspended few-atom-plane film; (e) AFM micrograph of few-atomic-layer steps in the cleaved films; and (f) TEM micrograph of the quasi-2D bismuth telluride film. Reprinted with Permission from D. Teweldebrhan, V. Goyal, and A.A. Balandin, *Nano Letters*, 10, 1209–1218 (2010).

In Figure 5.3 (a) below, we present an electron diffraction pattern, which indicates that the separated atomically-thin layers of bismuth telluride are crystalline after all processing steps. The elemental composition and stoichiometry of the atomically thin Bi-Te layers were studied by the energy dispersive spectrometry (EDS). The data were recorded for the suspended films (like those shown in Figure 5.3 (c-d)). Representative EDS spectra for a suspended quasi-2-D crystal and a thick Bi_2Te_3 film (used as a "bulk" reference) are shown in Figure 5.3 (b-c). Note that the most pronounced peaks in Figure

5.3 (b) are those of Si and oxygen (O) proving the electron beam penetration through the suspended atomically-thin film. The Si and O peaks are absent in Figure 5.3 (c) for thick Bi_2Te_3 crystal, which absorbes the elecrton beam completely.

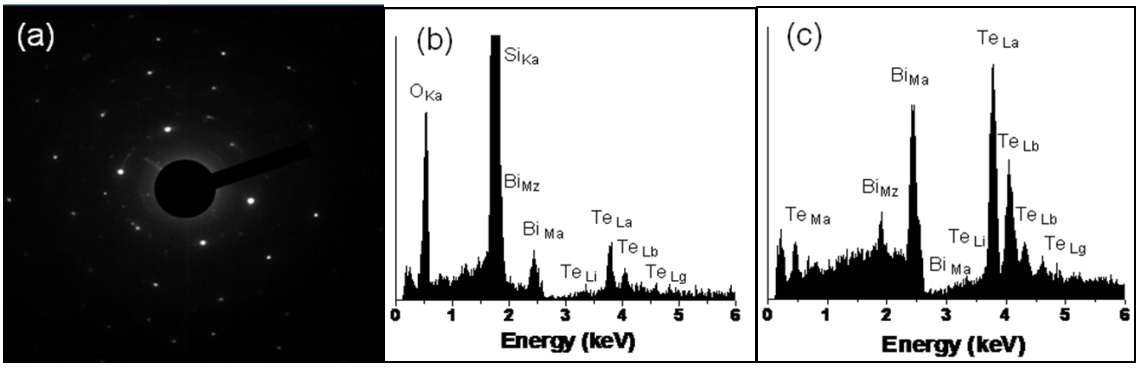

Figure 5.3: Structural and compositional characterization data showing (a) electron diffraction pattern indicating that quasi-2D Bi-Te films are crystalline; (b) EDS spectrum of the suspended atomic film of bismuth telluride; and (c) EDS spectrum of the reference thick film. Note that the dominant peaks in the EDS spectrum of the quasi-2D Bi-Te film shown in (b) are those of Si and O proving transparency of the atomic film for the electron beam. These peaks are absent in the spectrum of the reference bulk Bi_2Te_3. Reprinted with Permission from D. Teweldebrhan, V. Goyal, and A.A. Balandin, *Nano Letters*, 10, 1209–1218 (2010).

For one of the films, which had a thickness of ~40 atomic planes (~8 quintuple layers), and occupied an intermediate position between quasi-2D crystals and bulk Bi_2Te_3 crystals we found that the molar contents of Bi and Te were found to be ~34.7% and 65.3%, respectively. Although the film is crystalline and the stoichiometry for the [$Te^{(1)}$-Bi-$Te^{(2)}$-Bi-$Te^{(1)}$] quintuple layers is preserved, one can talk about an apparent deviation from the stoichiometry due to the fact that the film is not truly bulk. For the large bulk bismuth telluride crystals used for exfoliation of the ultra-thin films we consistently found 40% to 60% ratio of Bi to Te corresponding to Bi_2Te_3 formula. The analysis of the

measured EDS spectrum of the suspended film, which made up ~10% of the total wt%, had a molar content percentage between Bi and Te of ~33.2% and 66.8%, respectively. Thus, the structural make up of that particular ultra-thin film has 1 to 2 ratio of Bi to Te atoms (e.g. Te-Bi-Te), which differs strongly from conventional bulk crystals.

5.3.3 Raman Spectroscopy Characterization of Bi_2Te_3 and Bi_2Se_3

We now turn to the analysis of Raman spectrum of the atomically-thin bismuth telluride films. Bi_2Te_3 has five atoms in its unit cell and, correspondingly, 15 phonon (lattice vibration) branches near the Brillouin zone (BZ) center (phonon wave vector q=0) [27]. Twelve of those 15 branches are optical phonons while the remaining 3 are acoustic phonons with the $A_{2u} + E_u$ symmetry. The 12 optical modes are characterized by $2A_{2u} + 2E_u + 2A_{1g} + 2E_g$ symmetry. Each of the E_g and A_{1g} mode are two-fold degenerate. In these phonon modes, the atoms vibrate in-plane and out-of-plane (i.e. perpendicular to the film plane), respectively [28]. We focused our analysis on the phonon peaks in the spectral range from 25 cm^{-1} to 250 cm^{-1}.

Figure 5.4 (a-b) show SEM image of the Bi-Te atomic film with the locations where the Raman spectra were taken as well as the spectra themselves. These spectra were recorded at very low excitation laser power (~0.22 mW on the sample surface) to avoid local heating. The examined flake was placed in such a way that it had a suspended region as well as regions rested on Si and SiO_2. The observed four Raman optical phonon peaks were identified as A_{1g} at ~ 62 cm^{-1}, E_{g2} at ~104 cm^{-1}, A_{1u} at ~120 cm^{-1} and A_{2g} at ~137 cm^{-1}. These peak positions are very close to the previously measured and assigned Raman peaks of bulk crystalline Bi_2Te_3 [27-29]. Richter *et al.* [27] in their detail study of

phonons in Bi_2Te_3 provided the following frequencies (in their notation): 134 cm^{-1} for A, 103 cm^{-1} for E_g and 120 cm^{-1} for A_{1u}. The A_{1u} peak is likely to become Raman active due to the symmetry breaking in atomically thin films. One can notice that the out-of-plane vibrations (at ~137 cm^{-1} and ~119 cm^{-1}) in the suspended Bi-Te atomic films have higher intensity. The latter may be an indication of the enhancement of these vibration modes in the atomically thin films, which are not supported by the substrate.

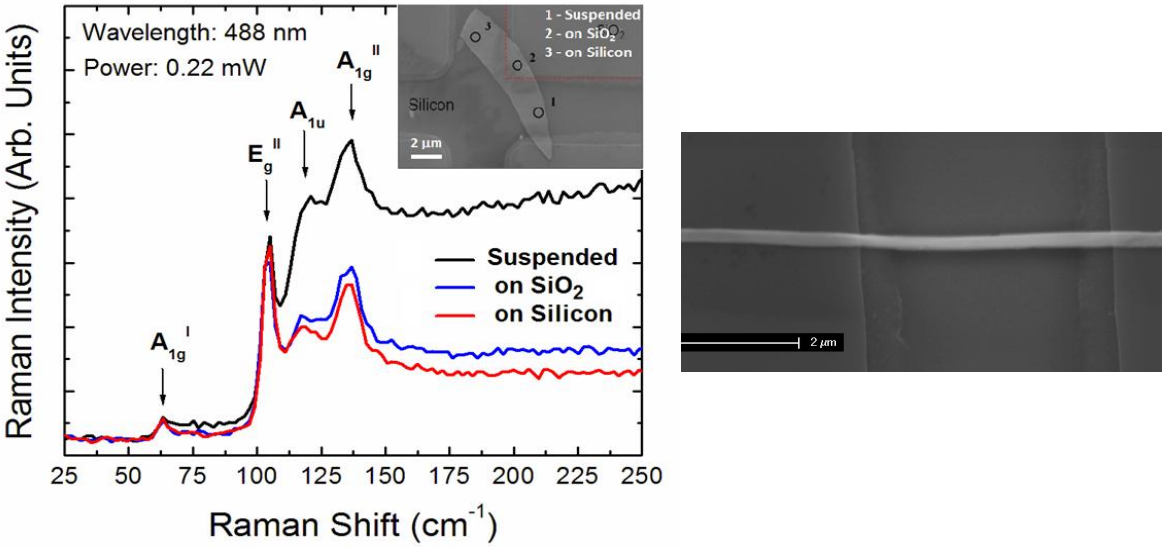

Figure 5.4: Raman spectra of quasi-2D bismuth telluride crystals. (a) SEM image showing suspended Bi-Te atomic film, which rests partially on SiO_2 and Si regions of the substrate. The spectra from the suspended and supported regions were recorded in the locations marked as 1, 2, and 3. (b) Informative Raman bands in the spectra of Bi-Te atomic films recorded at very low excitation power level. Note that the out-of-plane phonon modes in the suspended atomic crystals have higher intensity. Reprinted with Permission from D. Teweldebrhan, V. Goyal, and A.A. Balandin, *Nano Letters*, 10, 1209–1218 (2010).

Bi_2Te_3	A^{I}_{1g}	E^{II}_{g}	A_{1u}	A^{II}_{1g}
Suspended	63.51 cm^{-1}	104.38 cm^{-1}	120.44 cm^{-1}	135.24 cm^{-1}
On Oxide ($Si0_2$)	63.29 cm^{-1}	104.00 cm^{-1}	116.00 cm^{-1}	135.50 cm^{-1}
On Silicon	63.27 cm^{-1}	104.21 cm^{-1}	117.50 cm^{-1}	135.83 cm^{-1}

Table 5.1: The Raman frequencies are provided for the main peaks for Bi_2Te_3 exfoliated atomic crystalline films on Silicon, on Oxide (SiO_2), and that are suspended. Out of plane mode A^{II}_{1g} is shown to enhance in suspended films. Surface charges may be forming stronger effects in suspended films.

The Raman study confirms that the exfoliated films are crystalline and atomically thin. A systematic study of the changes in Raman spectrum due to modification of the vibration modes in the exfoliated ultra-thin films suspended or supported on the substrate was complicated due to pronounced local heating effects. Bulk single crystal Bi_2Te_3 is known to have very low thermal conductivity of ~ 1.5 – 2.0 W/mK along the cleavage plane and 0.6 W/mK along the van der Waals bonding direction [30]. It also has a low melting point of 573 ^{o}C. The local laser heating was a major problem when we tried to increase the excitation power to the levels typical for use with other materials. The maximum excitation power of the Ar+ laser (with the wavelength of 488 nm) used in this study was 10 mW. Approximately half of the excitation power reaches the sample surface after transmission through the optical system. The use of the power levels above 0.5 mW (corresponded ~0.22 mW on the sample) resulted in appearance of the holes due to local melting of the atomically-thin flakes as it is seen in the inset to Figure 5.5. In this image

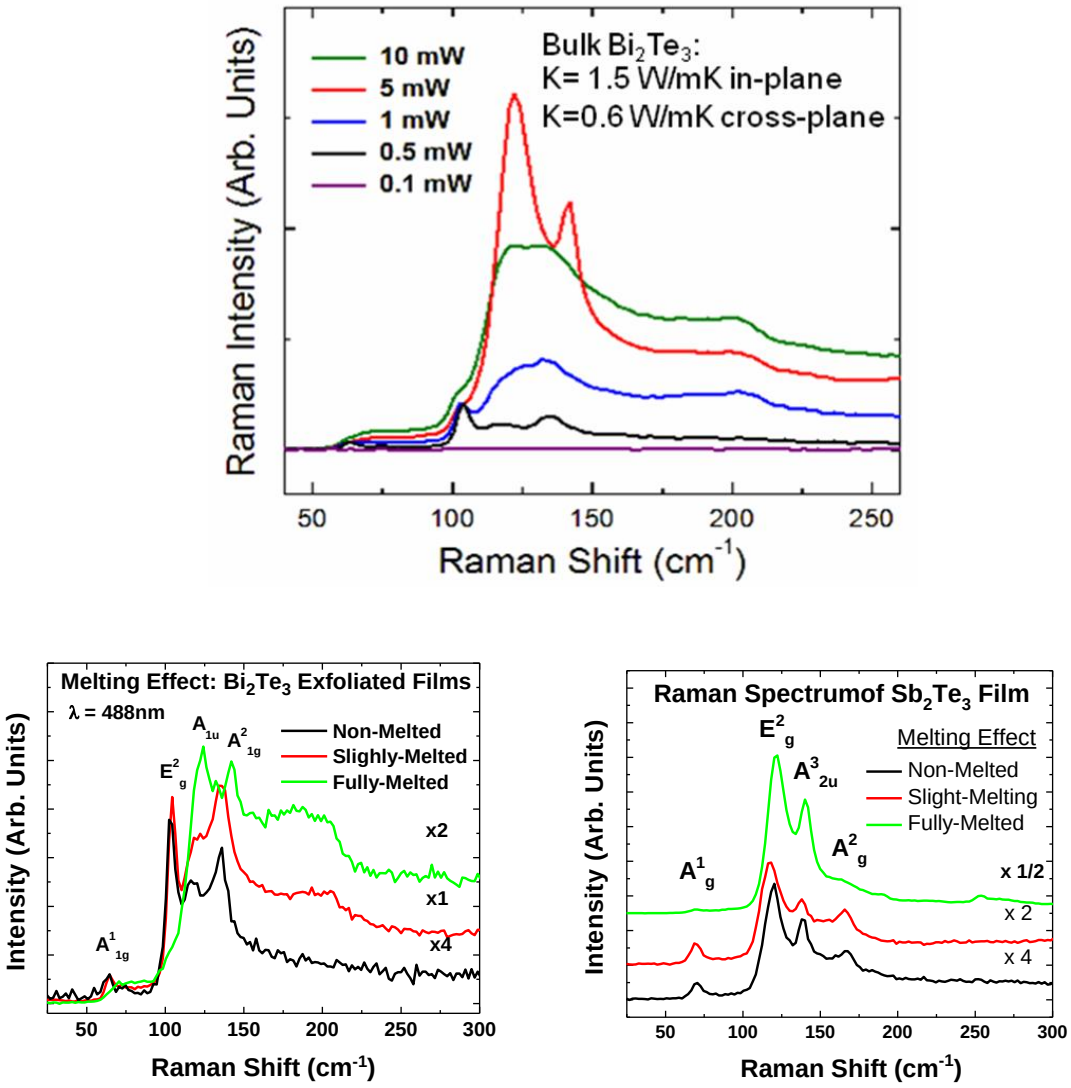

Figure 5.5: Evolution of Raman spectra from the Bi-Te atomic film with changing intensity of the excitation laser power illustrating a very narrow range of power levels suitable for exciting informative phonon bands. The power levels above 0.5 mW (corresponding to ~ 0.22 mW on the sample surface) lead to local melting of the atomic Bi-Te crystals in sharp contrast to graphene.

100% corresponds to the power of 10 mW set at the laser. We observed reproducibly that the diameter of the laser burned holes was growing with increasing excitation power. Figure 5.5 shows an evolution in Raman spectra of Bi-Te atomic layers as the excitation

power changes. When the power is too low (0.1 mW) no spectrum is excited. The excitation power of 0.5 mW provides meaningful spectra, which are in line with those obtained for bulk Bi_2Te_3 (at this power level no hole-burning or other laser-induced structural disorder were observed in microscopy images). As the power grows higher than 0.5 mW the Raman spectrum begins to change as a result of the local melting of the material. No laser damage was observed for the bulk Bi_2Te_3 at these power levels. For this reason, the selection of the right excitation power for Raman spectroscopy of the atomically thin Bi-Te layers is crucial for obtaining informative phonon bands. The drastically different reaction of the films on laser heating confirms their few-atomic layer thickness. In principle, one can envision a method for verifying the thickness of the film by examining the power dependence of the diameter of the burned holes.

The observed easy local heating damage to Bi-Te atomic flakes was in sharp contrast to graphene, a material characterized by extremely high thermal conductivity [31-32]. We were able to use much higher laser power on suspended graphene without inflicting any damage to its lattice. The heat conduction in strictly 2D systems is a complicated subject deserving special consideration. The thermal conductivity of conventional thin films usually decreases with decreasing film thickness as a result of the acoustic phonon – boundary scattering [12-13]. At the same time, it is also known that the thermal conductivity limited by crystal anharmonisity (also referred to as intrinsic) has a logarithmic divergence in strictly 2D system [33]. This anomalous behavior of the 2D thermal conductivity, which leads to its infinite values, has been studied extensively for many different crystal lattices and atomic potentials [34-35]. One needs disorder (e.g.

extrinsic scattering mechanisms) in order to obtain a finite value of the thermal conductivity in 2-D systems or limit the lateral size of the system [33-35]. In our case of Bi-Te flakes, the samples had the thickness of several atomic layers (not exactly 2D system but rather a quasi-2D) and the extrinsic effects were dominant. Due to the very low thermal diffusivity and thermal conductivity of Bi_2Te_3 crystals at first place, the induced heat had not escaped fast enough from the local spots leading to the lattice melting and observed lattice damages. As a consequence, for thermoelectric applications, it would be better to use stacks of bismuth telluride quintuple layers, put one on top of the other, rather than atomic bi-layers. Indeed, quintuples are more mechanically robust and expected have even lower thermal conductivity than Bi_2Te_3 bulk values. For Bi_2Se_3, we have been able to characterize change in crystallinity using Raman spectroscopy (Figure 5.6). Due to excess Se concentration in random exfoliated films, using Raman one may be able to detect the quality of the atomically thin layered films they are working with. This is analogous to the disorder D-peak in Graphene. This band is located at between ~230 cm^{-1} to 250 cm^{-1}, and its preliminary analysis is shown below in Figure 5.6. More analysis will be published on the topic.

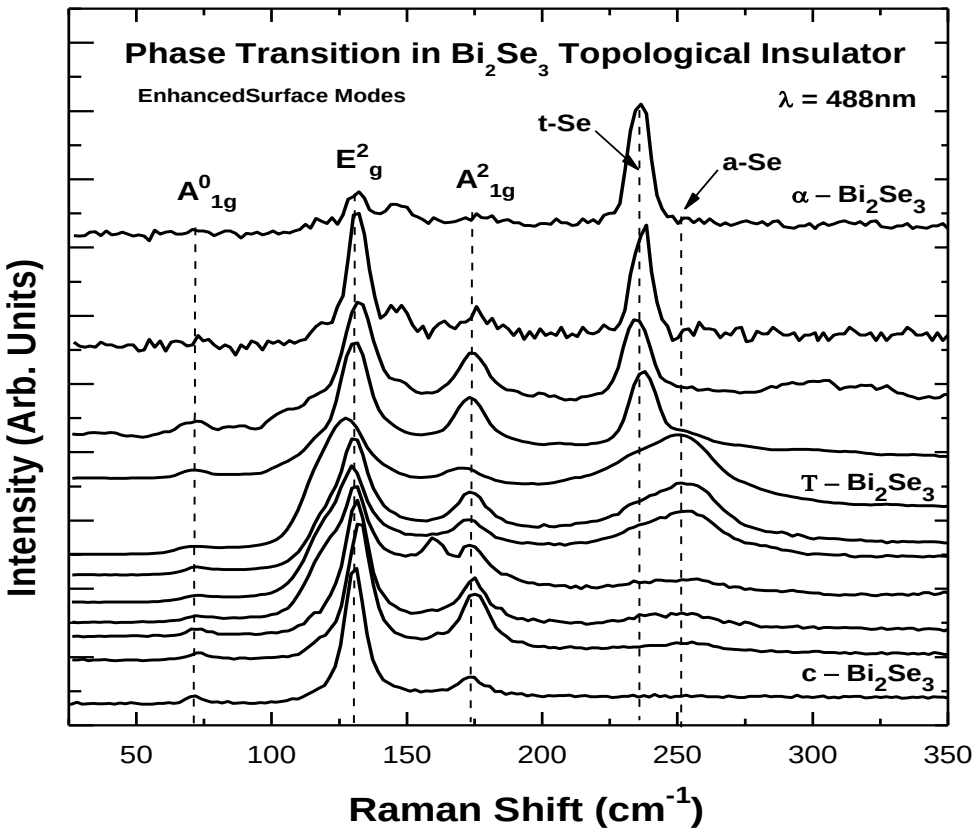

Figure 5.6: Raman analysis of Bi_2Se_3 surface topography.

5.3.4 Electrical Properties of Exfoliated 2D Films

By altering the thickness and sequence of atomic planes we were able to create "designer" non-stoichiometric quasi-2D crystalline films, change their composition and doping, the type of charge carriers as well as other properties. The possibility of changing the "effective" atomic composition in the crystalline ultra-thin films is very important for practical applications. It is known from the extensive studies of the thermoelectric properties of bismuth telluride, that a small small variation of ~0.1% in the Bi to Te atomic ratio can change the properties of the material from p-type to n-type [25]. Intentional deviation from stoichiometry during synthesis of bismuth telluride compounds and alloys has been conventionally used for "doping" this type of materials [26]. The close-to-stoichiometric Bi_2Te_3 is of p-type with a free carrier concentration of approximately 10^{-19} cm^{-3}. A shift to excess Te leads to an n-type material. Since our atomically thin films are crystalline, the "stoichiometric doping" may work in different ways than in the polycrystalline or disordered alloy bismuth telluride materials. In the atomically-thin crystals the charge can accumulate on the film surfaces or film – substrate interfaces. In this sense, the obtained quasi-2D crystals may open up a new way for doping and tuning the properties of bismuth telluride materials.

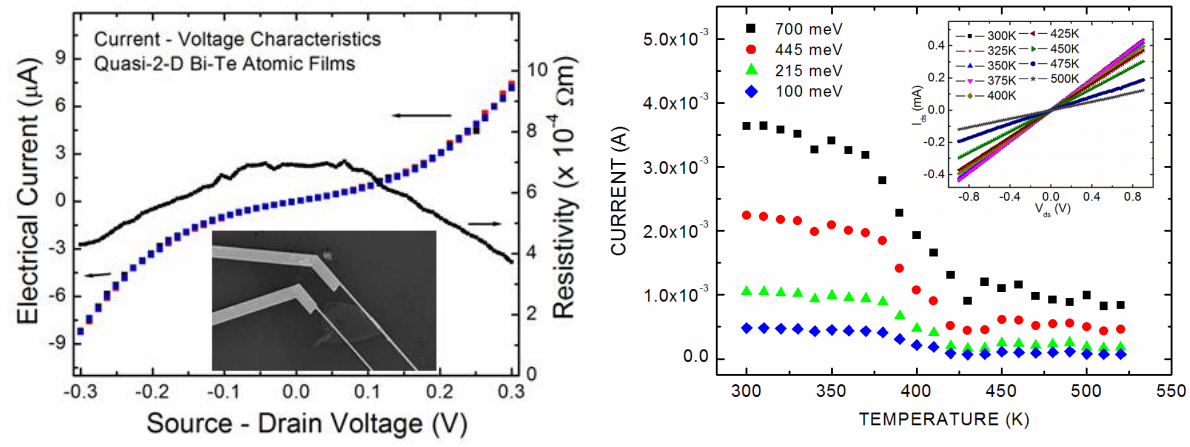

Figure 5.7: (a) Electrical current and resistivity of the quasi-2D bismuth telluride crystal as functions of the applied source – drain bias. The inset shows an optical microscopy image of the test structure. (b) Current as a function of temperature in Bi-Te atomic crystals shown for different source – drain voltages. Inset shows current – voltage characteristics in the low-bias region for different temperature. Reprinted with Permission from D. Teweldebrhan, V. Goyal, M. Rahman and A. A. Balandin, Appl. Phys. Lett. 95, 106952 (2010).

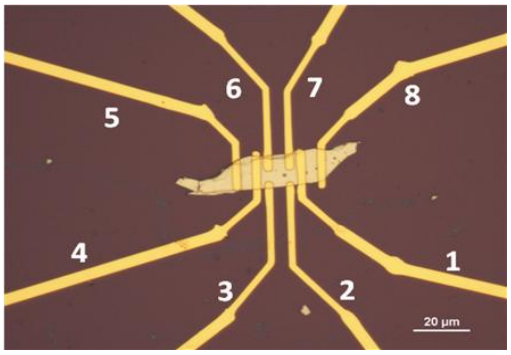

Figure 5.8: Optical Image if few-layer bismuth telluride hall bar structure device.

For transport measurements were prepared Bi-Te devices with a bottom gate and two top metal contacts (Figure 5.8). The RT current – voltage characteristics shown in Figure 5.7a reveal a weak non-linearity and rather low electrical resistivity of on the

order of 10^{-4} Ωm. This value (which includes contact resistance) is comparable to the resistivity values frequently measured for thick evaporated Bi_2Te_3 films used in thermoelectric devices [36-37]. The latter suggests that the charge carriers are not depleted in the samples and that the atomically thin bismuth telluride films retain their electrical properties. We did not observe a strong gating effect for Bi-Te devices while sweeping the back gate bias fro -50V to 50V. That was in a sharp contract to our experiments with the back-gated graphene and few-layer graphene devices [38-39]. In fabrication of graphene and Bi-Te devices we followed similar procedures and used the same heavily-doped Si/SiO_2 wafers. One possible explanation of the weak gating in Bi-Te atomic films can be a strong doping of the flakes due to the "stoichiometric doping" discussed above. The charge accumulation at the interfaces terminated with either Bi or Te atoms can screen the electric field produced by the back gate.

The described electrically conducting bismuth telluride quasi-2D crystals can be used as quantum wells with nearly infinite potential barriers for thermoelectric applications. The charge carriers and acoustic phonons in the crystalline quintuple layers with the thickness of ~1 nm will be strongly confined spatially. At the same time, any practical application of thermoelectric nanostructures requires a sufficient "bulk" volume of the material for development of the temperature gradient, in case of cooling, or voltage, in case of power generation. An individual quantum well would not be suitable. For this reason, we envisioned a practical method for utilization of Bi-Te quasi-2D crystals by stacking exfoliated films one on top of the other [40].

The room-temperature (RT) SD current – voltage characteristics of the devices made from the bismuth telluride flakes with the uniform thickness (number of atomic planes) revealed linear dependence (see inset to Figure 5.7b) and a rather low electrical resistivity on the order of ~10^{-4} Ωm. The measured RT resistivity is comparable to the values reported for thick Bi_2Te_3 films used in thermoelectric devices [5, 36, 41-43]. The resistivity of ~10^{-5} Ωm is considered to be optimal in conventional Bi_2Te_3 films because its further reduction leads to decreasing Seebeck coefficient. A weak non-linearity was observed for higher SD voltage and higher temperature *T*. Figure 5.7b shows I_{SD} current in the atomically-thin crystalline bismuth telluride films as the function of temperature for several different voltages. One can see that the current is nearly constant for *T* below ~375 – 400 K but then starts to decrease rapidly before it saturates at T ~ 450 K. Such temperature dependence was reproducible for several tested devices and observed before and after annealing. The data shown in the inset for a different device revealed a similar trend. In general, the increase of the resistance with increasing temperature is more typical of metals rather than semiconductors. But it is rather common for Bi_2Te_3 films and was observed for materials produced by a range of different techniques [5, 36, 41-43]. It is explained by the specifics of the electron scattering on acoustic phonons and defects in Bi_2Te_3 [44] although few exceptions from this dependence were also reported [45]. In our case, the dependence is not monotonic with the bending point ~400 K. In the thin films with the thickness of just few atomic layers the electron transport may strongly depend on the coupling to the substrate and remote impurity scattering.

5.3.5 2D Topological Insulators

Most recently, the interest to the stacked quasi-2D layers of bismuth telluride received an additional impetus from an unexpected direction. It has been shown that stacks of quasi-2D layers of Te-Bi-Te-Bi-Te are members of a new type of recently discovered materials referred to as *topological insulators* (TIs) [15-17]. The surface state of a quasi-2D crystal of Bi_2Te_3 is predicted to consist of a single Dirac cone. Moreover, it has been shown that the layered structures of related materials such as Bi_2Se_3 and Sb_2Te_3 are also topological insulators. The particles in topological insulators coated with thin ferromagnetic layers have manifested exotic physics and were proposed for possible applications in the magnetic memory where write and read operations are achieved by purely electric means. All these stimulate the search for methods to produce quasi-2D crystals of bismuth telluride even further. Other proposed applications of TIs include quantum computing, spintronics, and low-energy dissipation electronics. As a method of better characterization and enhance technique of observing topological effects, this work is the first reported method of isolation of individual quintuples and few-quintuple layer of Bi_2Te_3. The mechanically exfoliated atomically-thin films of Bi_2Te_3 can be transferred to various substrates and coated with other materials for TI investigation.

5.3.6 Thermal Conductivity of Stacked Bi_2Te_3

The quasi two-dimensional crystals of bismuth telluride revealed high electrical conductivity. The proposed *atomic-layer engineering* of bismuth telluride opens up a principally new route for drastic enhancement of the thermoelectric figure of merit.

Enhancement in figure of merit, *ZT*, by the proposed exfoliated Bismuth Telluride "stacked superlattices". The Bismuth Telluride "stacked-superlattices" were prepared by stacking mechanically-exfoliated crystalline Bismuth telluride films one on top of other. The Seebeck coefficient *S*, the thermal *K*, and electrical conductivity σ are investigated on these "stacked superlattices". The data shows drastic drop in both the in-plane and cross-plane thermal conductivity of the Bi_2Te_3 "stacked-superlattices" compared to bulk Bi_2Te_3 crystals which were used for exfoliation of the films. The dependence of thermal conductivity on temperature is found to be weak, suggesting the phonon transport to be dominated by boundary scattering. This represents that disorder and boundary resistance in Bi_2Te_3 stacked-suprlattices can limit the thermal conductivity and in turn can enhance the *ZT*. The proposed *stacked-superlattices* may embark a new promising pathway for their practical use in thermoelectric cooling applications.

The obtained "*stacked superlattices*" are expected to retain the useful properties of individual atomic films such as quantum confinement of charge carriers and reduced phonon thermal conductivity. Indeed, the potential barriers for charge carries in such crystalline films remain very high unlike in the epitaxially grown Bi_2Te_3-based superlattices with the lattice matched barriers where the band off-sets are small. The thermal conductivity in the mechanically separated and stacked layers is reduced due to the acoustic phonon – rough boundary scattering or acoustic phonon spatial confinement in exactly the same way as in the individual films. We experimentally tested a possibility of *ZT* enhancement in prototype stacked films by measuring the thermal conductivity and

Seebeck coefficient, and comparing them with those of the reference Bi_2Te_3 bulk crystals, which was used for the exfoliation of the films.

The thermal conductivity *K* of the prototype stacked atomic-films was determined by two different methods: the laser-flash (Netszch LFA) and the transient planar source (TPS) technique (Hot Disk). Both techniques have been "calibrated" via comparison with the values obtained with the in-house built 3-ω method [46-48], which is considered to be a standard technique for thin films. We have previously successfully used 3-ω measurements for electrically insulating thin films with the thickness down to ~1 nm [49]. The Seebeck coefficient of stacked films was determined using MMR system (SB100) consisting of two pairs of thermocouples. Details of the measurements are provided in the Methods. We found significant drop in the cross-plane (in-plane) thermal conductivity from ~0.5 – 0.6 W/mK (~1.5 – 2.0 W/mK) in bulk reference to ~0.1-0.3 W/mK (~1.1 W/mK) in the stacked films at RT. The thermal conductivity of stacked superlattices revealed a very weak temperature dependence suggesting that the acoustic phonon transport was dominated by the boundary scattering. It is interesting to note that the measured cross-plane *K* value is close to the minimum thermal conductivity for Bi_2Te_3 predicted by the Cahill model [50], which gives the low bound of ~0.12 W/mK. We have not observed substantial changes in the thermal power beyond experimental uncertainty with the measured Seebeck coefficient (~234 μV/K) only slightly above its bulk reference value. The latter was attributed to the fact that the Fermi level was not optimized in these films. More research is needed to gain complete control of the carrier densities in the mechanically exfoliated films. At the same time, the measured decrease

of the thermal conductivity resulting in the *ZT* enhancement by about 30% - 40% of its bulk value is extremely promising for thermoelectric applications. Additional *ZT* increase in a wide temperature range can be achieved with the cross-plane electrical gating of the Bi-Te atomic films.

5.4 Summary

Following the procedures similar to those developed for graphene mechanical exfoliation, we were able to produce bismuth telluride crystals with a thickness of few atoms. The quais-2D atomic crystals were suspended across trenches in Si/SiO_2 substrates and subjected to detail characterization using SEM, TEM, EDS, AFM, SAED and micro-Raman spectroscopy. It was established that the presence of the van der Waals gaps in Bi_2Te_3 crystals allows one to disassemble them into atomic quintuples, i.e. five atomic planes Te-Bi-Te-Bi-Te, which build up 3D crystal. Moreover the microscopy analysis shows that the bonds inside quintuples can be broken further leading to Bi-Te bi-layers and Te-Bi-Te tri-layers. By altering the thickness and sequence of atomic planes one can create "designer" non-stoichiometric crystalline films and change their properties. The exfoliated quintuples have low thermal conductivity and good electrical conductivity. The "stacked superlattices" made of the mechanically exfoliated bismuth telluride films show substantially enhanced thermoelectric figure of merit. The obtained results may lead to completely new scalable methods for producing low-dimensional thermoelectrics and atomic-layer engineering of their properties. The described technology for producing

free-standing quasi-2D layers of Te-Bi-Te-Bi-Te can be used for investigation of the topological insulators and their possible practical applications.

The developed technology for producing free-standing quasi-2D layers of $Te^{(1)}$-Bi-$Te^{(2)}$-Bi-$Te^{(1)}$ creates an impetus for investigation of the topological insulators and their possible practical applications. The obtained results pave the way for producing stacks of crystalline bismuth telluride quantum wells with the strong spatial confinement of charge carriers and acoustic phonons, beneficial for thermoelectric and topological insulator devices. Most of the thermoelectric thin films or superlattices on the basis of Bi_2Te_3 investigated so far were either polycrystalline or alloyed, or had the thicknesses far greater and the potential barrier higher far less than those required for strong spatial confinement of electrons and phonons.

It is important to understand if the electrical conductivity of bismuth telluride is preserved after it was structured to films with the thickness of just few atomic layers. Transport measurements were prepared Bi-Te devices with indicate RT current – voltage characteristics showed resistivity of on the order of 10^{-4} Ωm which is comparable to the resistivity values frequently measured for thick evaporated Bi_2Te_3 films used in thermoelectric devices . Recently it was shown theoretically by Bejernari *et al.* [51] that a combination of quantum confinement of carriers and perpendicularly applied electric field in bismuth telluride nanostructures can be effective for ZT improvement. The developed exfoliation technique can also be extended to other thermoelectric material

systems [52]. This approach is particularly promising for the thermoelectric cooling applications at low temperature.

References

[1] Ioffe, A.F., *Semiconductor Thermoelements* (Nauka, Moscow, 1956) (in Russian); or Ioffe, A.F., *Semiconductor Thermoelectric and Thermoelectric Cooling* (Infosearch, London, 1957.)

[2] H.J. Goldsmid and R.W. Douglas, Thermoelectric *Br. J. Appl. Phys.*, **5**, 458 (1994).

[3] D.A. Wright, *Nature*, **181**, 834 (1958).

[4] R. Venkatasubramanian, E. Siivola, T. Colpitts and B. O'Quinn, *Nature*, **413**, 597 (2001).

[5] W. Xie, X. Tang, Y. Yan, Q. Zhang and T.M. Tritt, *J. Applied Phys*., **105**, 113713 (2009).

[6] F.J. DiSalvo, *Science*, **285**, 703 (1999).

[7] M.S. Dresselhaus, G. Dresselhaus, X. Sun, Z. Zhang, S. B. Cronin and T. Koga, *Physics of the Solid State*, **41**, 679 (1999).

[8] L.D. Hicks and M.S. Dresselhaus, *Phys. Rev. B.*, **47**, 12727 (1993).

[9] D.A. Broido and T.L. Reinecke, *Appl. Phys. Lett.*, **67**, 100 (1995).

[10] A. Balandin, K.L. Wang, *Physical Review B*, **58**, 1544 (1998).; A. Balandin and K.L. Wang, *J. Applied Physics*, **84**, 6149 (1998).

[11] J. Zou and A. Balandin, *J. Appl. Phys.*, **89**, 2932 (2001**).**

[12] G. Chen, T. Borca-Tasciuc, B. Yang, D. Song, W.L. Liu, T. Zeng and D.A. Achimov, *Thermal Science and Engineering* , **7**, 43 (1999).

[13] T. Borca-Tasciuc, D. Achimov, W.L. Liu, G. Chen, H.-W. Ren, C.-H. Lin and S.S. Pei, *Microscale Thermophysical Engineering*, **5**, 225, (2001).

[14] Y. Feutelais, B. Legendre, N. Rodier and V. Agafonov, *Mater. Res. Bull.*, **28**, 591(1993).

[15] For a review see Qi, X.-L.; Zhang, S.-C. *Physics Today*, January **2010**, 33-38.

[16] B.A. Bernevig, T.L. Hughes and S.C. Zhang, *Science*, **314**, 1757 (2006).

[17] M. Konig, S. Wiedmann, C. Brune, A. Roth, H. Buhmann, L. W. Molenkamp, X-L Qi, and S.C Zhang, *Science,* **318**, 766, (2007).

[18] K.S. Novoselov, A.K. Geim, S.V. Morozov, D. Jiang, Y. Zhang, S.V. Dubonos, I.V. Grigorieva, and A.A. Firsov, *Science*, **306**, 666 (2004).

[19] K.S. Novoselov, D. Jiang, F. Schedin, T.J. Booth, V.V. Khotkevich, S.V. Morozov, A.K. Geim, *PNAS*, **102**, 10453 (2005).

[20] K.S. Novoselov, A.K. Geim, S.V. Morozov, D. Jiang, M.I. Katsnelson, I.V. Grigorieva, S.V. Dubonos and A.A. Firsov, *Nature*, **438**, 197 (2005)**.**

[21] Y. Zhang, J.W. Tan, H.L. Stormer, and P. Kim, *Nature*, **438**, 201(2005).

[22] I. Calizo, A.A.Balandin, W. Bao, F. Miao, and C.N. Lau, *Nano Lett.*, **7**, 2645 (2007).

[23] I. Calizo, W. Bao, F. Miao, C.N. Lau, and A.A. Balandin, *Appl. Phys. Lett*., **07**, 201904 (2007).

[24] I. Calizo, I. Bejenari, M. Rahman, G. Liu, and A.A. Balandin, *J. Appl. Phys.*, **106**, 043509 (2009).

[25] P. Jones, T.E. Hubera, J. Melngailisb, J. Barryb, M.H. Ervin, T.S. Zhelevac, A. Nikolaevad, G.M. Leonid Konopkod, *IEEE Inter. Conf. Of Thermoelectrics*, **693** (2006).

[26] S. Golia, M. Arora, R.K. Sharma and A.C. Rastogi, *Current Appl. Phys.*, **3**, 195 (2003).

[27] W. Richter, H. Kohler, C.R. Becker, *Phys. Stat. Sol. B,* **84**, 619 (1977).

[28] V. Russo, A. Bailini, M. Zamboni, M. Passoni, C. Conti, C.S. Casari, A. Li Bassi and C.E. Bottani, *J. Raman Spectroscopy*, **39**, 205 (2008).

[29] W. Lu, Y. Ding, Y. Chen, Z.L. Wang, J. Fang, *J. Am. Chem. Soc.*, **127**, 10112 (2005).

[30] D.G. Cahill et. al; *J. Appl. Phys*., **93**, 2 (2003).; C. Chiritescu, C. Mortensen, D.G. Cahill, D. Johnson, P. Zschack, *J. Appl. Phys*., **106**, 073503 (2009).

[31] A.A. Balandin, S. Ghosh, W. Bao, I. Calizo, D. Teweldebrhan, F. Miao and C.N. Lau, *Nano Letters* **8**, 902 (2008).; S. Ghosh, I. Calizo, D. Teweldebrhan, E.P. Pokatilov, D.L. Nika, A.A. Balandin, W. Bao, F. Miao, and C.N. Lau, *Appl. Phys. Lett.* **92**, 151911 (2009).

[32] D.L. Nika, S. Ghosh, E.P. Pokatilov, A.A. Balandin, *Appl. Phys. Lett*., **94**, 203103 (2009); D. L. Nika, E.P. Pokatilov, A.S. Askerov and A.A.Balandin, *Phys. Rev. B*, **79**, 155413 (2009).

[33] S. Lepri, R. Livi and A. Politi, *Phys. Rep.* **377**, 1-80 (2003).

[34] G. Basile, C. Bernardin and S. Olla, *Phys. Rev. Lett.* **96**, 204303 (2006).

[35] A. Dhar, *Phys. Rev. Lett.*, **86**, 5882 (2001).

[36] X.H. Ji, X.B. Zhao, Y.H. Zhang, B.H. Lu, H.L. Ni, *Materials Letters*, **59**, 682 (2005).

[37] J.Y. Yang, T. Aizawa, A. Yamamoto, and T. Ohta, *J. Alloys and Compounds*, **312**, 326 (2000).

[38] Q. Shao, G. Liu, D. Teweldebrhan, A.A. Balandin, S. Rumyantsev, M. Shur and D. Yan, *IEEE Electron Device Lett*,.**30**, 288 (2009).

[39] G. Liu, W. Stillman, S. Rumyantsev, Q. Shao, M. Shur and A.A. Balandin, *Appl. Phys. Lett.* **95**, 033103 (2009).

[40] D. Teweldebrhan and A.A. Balandin, Methods for Producing Atomically-Thin Bismuth Telluride Films and Stacked Superlattices for Thermoelectric and Topological Insulator Applications, Invention Disclosure. University of California – Riverside, December (2009).

[41] O. Yamashita and S. Tomiyoshi, *Jpn. J. Appl. Phys*. **42**, 492 (2003).

[42] J.P. Fleurial, L. Gailliard and R. Triboulet, *J. Phys. Chem. Solids*. **49**,1237 (1988).

[43] V.A. Kulbachinskii, M. Inoue, M. Sasaki, H. Negishi, W. X. Gao, K. Takase, Y. Giman, P. Lostak and J. Horak, *Phys. Rev. B.*, **50**, 16921 (1994).

[44] T.A. Christakudi, S.K. Plachkova and G.C. Christakudis, *Phys. Stat. Sol. (b).* **195**, 217 (1996).

[45] V. Damodara Das and N. Soundararajan, *Phys. Rev. B*, **37**, 4552 (1988).

[46] M. Shamsa, W.L. Liu, A.A. Balandin, C. Casiraghi, W.I. Milne, A.C. Ferrari, *Appl. Phys. Lett.*, **89**, 161921 (2006).

[47] S. Ghosh, D. Teweldebrhan, J.R. Morales, J.E. Garay, A.A. Balandin, *J. Appl. Phys*., **106**, 113507 (2009).; R. Ikkawi, N. Amos, A. Lavrenov, A. Krichevsky, D. Teweldebrhan, S. Ghosh, A.A. Balandin, D. Litvinov and S. Khizroev, *J. Nanoelectron. Optoelectron*., **3**, 44 (2008).

[48] M. Shamsa, S. Ghosh, I. Calizo, V. Ralchenko, A. Popovich and A.A. Balandin, *J. Appl. Phys.* **103**, 083538 (2008).

[49] A.A. Balandin, M. Shamsa, W.L. Liu, C. Casiraghi and A.C. Ferrari, *Appl. Phys. Lett.*, **93**, *93*, 043115 (2008).

[50] D. Cahill, S. Watson and R. Pohl, *Phys. Rev. B*, **46**, 6131 (1992).

[51] I. Bejenari, V. Kantser, A.A. Balandin, Phys. Rev. B., **81**, 075316 (2010).; I. Bejenari, V. Kantser, *Phys. Rev. B*, **78**, 115322 (2008).

[52] A. Casian, I. Sur, H. Scherrer, Z. Dashevsky, *Phys. Rev. B*, **61**, 15965 (2000).

[53] M.R. Dirmyer, J. Martin, G.S. Nolas, A. Sen, J.V. Badding, *Small*, **5**, 933 (2009).

[54] S. E. Gustafsson, *Rev. Sci. Instrum*. **62**, 797 (1991).

Chapter 6

Concluding Remarks

It's presented here a look at an alternative class of 2D Dirac materials as possible alternative materials to meet the challenges of industry as it moves towards smaller device feature sizes, increased integration densities and faster operation speeds. Dirac materials are characterized by the liner electron dispersion, and can be complementary materials in a wide variety of electronic applications. In this dissertation I investigated two representatives of Dirac materials – graphene and topological insulators, and focused on (i) effects of electron beam irradiation on graphene properties and (ii) electronic and thermal characteristics of exfoliated films of Bi_2Te_3-family of topological insulators. It was found that the radiation exposures result in appearance of the disorder D band around 1345 cm^{-1}. The dependence of the ratio of the intensities of D and G peaks, I(D)/I(G), on the irradiation dose is non-monotonic suggesting graphene's transformation to

polycrystalline and then to disordered state. It was shown that by controlling the irradiation dose one can change the carrier mobility and increase the resistance at the minimum conduction point in graphene.

For bismuth telluride and related compounds it was shown that they can be successfully in exfoliationed in a "graphene-like" fashion to produce large-area crystalline films and ribbons with the thickness going down to a single quintuple. The presence of the van der Waals gap allowed us to disassemble Bi_2Te_3 crystal into the five mono-atomic sheets consisting of $Te^{(1)}$-Bi-$Te^{(2)}$-Bi-$Te^{(1)}$. The exfoliated films had extremely low thermal conductivity and electrical resistance in the range required for thermoelectric applications. The obtained results may pave the way for producing crystalline Bi_2Te_3 films and stacked superlattices with the strong quantum confinement of the charge carriers and predominantly surface transport and allow one to obtain theoretically predicted order-of-magnitude higher thermoelectric figure-of-merit.